TÉCNICO LISBOA

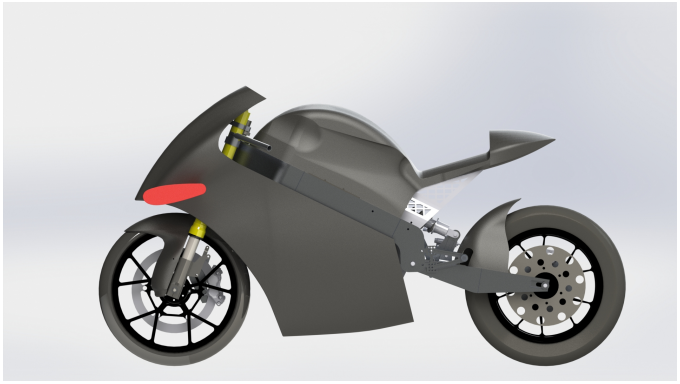

On the Aerodynamics Performance of MotoGP Wings

João Gaspar Cardoso Coelho da Silva

Thesis to obtain the Master of Science Degree in

Mechanical Engineering

Supervisor(s): Prof. Luís Rego da Cunha de Eça
Prof. José Manuel Chaves Pereira

Examination Committee

Chairperson: Prof. Carlos Frederico Neves Bettencourt da Silva
Supervisor: Prof. Luís Rego da Cunha de Eça
Member of the Committee: Prof. Duarte Manuel Salvador Freire Silva de Albuquerque

November 2019

To all important people in my life this dissertation is also yours!!!!

Acknowledgments

I would like to express the deepest gratitude and appreciation to my supervisors, Professor Luís Eça and Professor José Chaves Pereira for their constant guidance throughout the dissertation.

To my all family, for all the support they have been given.

To Eva Gonçalves for always believing in me, for all the support during this dissertation and during the last 8 years. You were my hope and inspiration for moving forward with this dissertation.

To António Januário for all support throughout the entire thesis. You were my inspiration to take a step further on the motorcycle dynamics subject.

To Diogo Neves for the positive energy and support.

To Francisco Jesus that was a big support during this dissertation and for the last four years in TLMoto Team.

To João Silva, André Alves and Eduardo Lima who have been my support over the last five years in university.

To the people working at LASEF for their hospitality and helpfulness.

Resumo

A presente dissertação analisou o desempenho aerodinâmico das asas utilizadas nos protótipos do MotoGP.

De forma a permitir a correta determinação das características aerodinâmicas das asas e do campo de escoamento, procedeu-se à resolução das equações de Navier-Stokes em média de Reynolds com a versão SST do modelo $\kappa - \omega$ e com o modelo de transição $\gamma - Re_\theta$ no software comercial Starccm+.

Numa primeira fase foram analisadas as características aerodinâmicas de um perfil simétrico, NACA0012, tendo-se verificado uma elevada dependência dos resultados numéricos com o modelo de transição escolhido.

Numa segunda fase, procedeu-se a uma análise dinâmica por forma a estudar a possível influência de acelerações e desacelerações dos protótipos do MotoGP nas características aerodinâmicas do perfil escolhido. Os resultados das análises efectuadas foram similares aos resultados obtidos por via de soluções estacionárias, podendo então concluir-se que o problema pode ser analisado como uma combinação de casos estacionários.

Por fim, foram analisadas várias configurações de asas dos protótipos de MotoGP, com o perfil NACA23015. Foi possível concluir que, devido ao reduzido alongamento das asas, os efeitos tridimensionais são determinantes nas suas características aerodinâmicas.

Palavras-chave: CFD, MotoGP Wings, RANS, modelo de trânsição $\gamma - Re_\theta$, Asas Fechadas

Abstract

This dissertation aims to investigate the aerodynamic performance of the MotoGP wings.

In order to determine the flow field and aerodynamic characteristics of these wings, the Reynolds Averaged Navier-Stokes equations were solved with SST version of the $\kappa - \omega$ turbulence model and the transition model $\gamma - Re_\theta$, supported by the commercial software Starccm+.

Firstly, through the analysis of a symmetric airfoil, NACA0012, it was possible to observe a high dependence of the transition models on the numerical solutions.

Secondly, the dynamic analysis was performed to estimate the possible influence of the MotoGP prototypes accelerations and decelerations in the airfoil aerodynamic characteristics. The deviation of the numerical results from the dynamic analysis was considered negligible, the reason why a quasi-steady approach is sufficient.

Finally, three-dimensional analyses of different MotoGP wings configurations were performed with the NACA23015. From the numerical results, it was concluded that the three-dimensional effects highly influence the finite wings aerodynamic characteristics.

Keywords: CFD, MotoGP Wings, RANS, $\gamma - Re_\theta$ transition model, Closed Wings

Contents

List of Tables

List of Figures

Acronyms

2D	2 Dimensional Space.
3D	3 Dimensional Space.
AoA	Angle of Attack.
BC	Boundary Condition.
BL	Boundary Layer.
CFD	Computational Fluid Dynamics.
DNS	Direct Numerical Simulation.
LES	Large-Eddy Simulation.
MotoGP	Moto Grand Prix.
SST	Shear Stress Transport.
WSBK	Superbike World Championship.

Nomenclature

Greek symbols

ν	Kinematic viscosity.
ω	Angular frequency.
ρ	Density.
τ	Viscous stress.

Roman symbols

c	Airfoil chord.
C_L	3D Coefficient of lift.
F_b	Braking force
F_D	Drag force
F_g	Force of gravity
F_g	Gravity force
F_L	Lift force
F_p	Driving force
St	Strouhal number
t	Airfoil maximum thickness.
U	Velocity.
V_{fluid}	Displaced volume.
WB	Wheelbase
X_{CG}	Center of gravity in x direction
Y_{CG}	Center of gravity in y direction

Subscripts

ref	Reference condition.

Chapter 1

Introduction

Ever since the first motorcycle was sold back in 1894, racing was one of the mechanisms that have driven forward these machines' development. In the early years, different manufacturers took the lead on the development of these racing machines having power delivery as the primary focus. Later on, technological development allowed the manufacturers to take a step further. The desire to accomplish better results in racing forced the engineers to integrate more competitive technologies on these machines. Starting from the chassis development up to the electronics, motorcycles started to embrace different engineering fields.

Figure 1.1: Example of a side-wings configuration integrated on the MotoGP fairings for the 2019 season.

The Grand Prix Motorcycle Racing, also known as MotoGP, is the premier class of motorcycle road racing events held on road circuits. For this reason, this competition has always been the main stage of motorcycle development. Race after race, manufacturers test new technologies looking forward to increasing the performances of the prototypes. Consequently, over the last few years in MotoGP, riders struggle to handle these prototypes due to an excessive increase in engine power. This excessive power causes the front wheel contact loss with the ground during acceleration, a phenomenon known as front-end-lift. For safety reasons, sensors and actuators systems, i.e. ECU, reduces the power delivered to the rider.

Throughout the years, the MotoGP prototypes have been integrating different solutions to avoid front-end-lift. This dissertation will cover one of these solutions, the side-wings illustrated in figure 1.1. The

idea behind these wings is to produce enough downforce to oppose the inertia forces during acceleration. This way, the engine power cut will be delayed increasing the power delivered to the rider.

The objective of this dissertation is to determine the performance of those wings aspiring to open a door in the study of different aerodynamic solutions to improve motorcycle performance.

1.1 Preliminary Work

A preliminary work about the motorcycle dynamics on track was developed in Appendix A. The objective was to determine the motorcycle behaviour along the track with the aid of a lap-simulator in Matlab. The lap-simulator was developed by the motorcycle prototype racing team of Instituto Superior Técnico, i.e. TLMoto team, providing data to the side-wings simulations.

In addition, a case study was performed to determine which power to weight ratio the front-end-lift starts to be a concern in four different motorcycle categories in Appendix B.

1.2 State of the Art

The flow around the MotoGP wings occurs at moderate Reynolds numbers. Therefore, the effect of laminar to turbulent flow transition region can be responsible for essential features at these Reynolds numbers flows. There are different studies around airfoils at this regime showing accurate results using the Reynolds-averaged Navier–Stokes (RANS) solver with the SST $\kappa - \omega$ turbulence model and the $\gamma - Re_\theta$ transition model, from [1], [2] and [3]. One of the airfoils widely studied in these regimes is the NACA0012, with different numerical results, from [1] and experimental data available in [4] and [5]. Regarding the available information, at the first stage, the CFD analysis will be performed around moderate Reynolds numbers with the NACA0012 airfoil.

When it comes to subsonic velocities, the wing characteristics can be highly sensitive to velocity variations, observed in [6], [7], [8] and [9]. For the present dissertation, the wings experience either accelerations, decelerations and pitching motion during a full lap on a circuit. Concerning these transient mechanisms, one of the main goals of this dissertation is to determine whether the quasi-steady approach is sufficient to predict the wing properties or otherwise, an unsteady approach is mandatory.

Lastly, this dissertation will analyse the three-dimensional effects on the wings aerodynamic performance. The MotoGP side wings due to geometric regulation constraints are within the low aspect ratio wings. As a consequence, the three-dimensional effects end up being highly intense, decreasing the wing aerodynamic performance substantially, from [10] and [11].

1.3 Objectives

The two main concerns of this dissertation are the transient and three-dimensional effects on the MotoGP wings aerodynamic performance. To obtain an answer to these problems this thesis includes the following studies:

- Include a transition model to simulate the flow with RANS.
- Obtain the lift and drag coefficients for the selected airfoil sections.
- Determine whether unsteady simulations are required or a quasi-steady approach is sufficient to determine the airfoil aerodynamic characteristics.
- Investigate the aerodynamics forces for the finite wings applied in MotoGP.

1.4 Thesis Outline

The dissertation is organized in four chapters with the following structure:

- Chapter 2 is confined to the problem definition. In an early stage, it will be discussed all physics aspects behind the front-end-lift problem and the physical conditions that bound the numerical analysis such as the wing size, the wing location, and the target downforce to avoid the front lift. Afterward, in this same chapter, it will be introduced the flow governing equations and flow regime. Finally, it will be introduced two case studies regarding the wing acceleration, deceleration, and pitching motion.
- In chapter 3, are described the mathematical models and numerical methods behind the computational fluid dynamics analysis.
- Chapter 4 will focus on the results of the two-dimensional analysis. It will consist of a parametric analysis over the NACA0012 for different Reynolds numbers and angles of attack. The results from unsteady simulations regarding wing acceleration, deceleration, and pitching motion will be discussed.
- In Chapter 5, the three-dimensional analyses will be performed around three different wing configurations over a cambered airfoil, the NACA23015. Firstly, a finite wing will be analysed with and without end-plate and lastly, the closed wings applied in MotoGP prototypes.

Chapter 2

Problem Definition

Single-track vehicles are characterized by their unique attributes. The lack of lateral stability introduces significant complexity to dynamic motorcycle behavior. In this dissertation, we look forward to studying the MotoGP wings aerodynamic performance along the straights of a road circuit. The performance of these wings during cornering will be off-topic with extensive analysis in [12].

In this chapter, it will be provided the required tools to perform the computational fluid dynamics analysis to the motorcycle wings. The section 2.1 will briefly pass through the dynamics associated with the front-end-lift effect, with extensive analysis in Appendix A. Determined the dynamic equations governing the problem, in section 2.2 it will be outlined the target downforce that the side-wings should produce to avoid the front-end-lift. Afterward, in section 2.3 the flow governing equations are introduced, and finally, in sections 2.4 and 2.5 are presented the two case studies about the wings acceleration, deceleration and pitching motion.

2.1 Motorcycle Dynamics

The motorcycle dynamics behold different subjects such as cornering, acceleration, deceleration, vibrations modes, stability and even more in [13]. The study of rectilinear motion highlights particular dynamics aspects concerning the MotoGP wing analysis.

Motorcycle modeling in straight running can be characterized by several degrees of freedom. Motorcycle dynamics analyses can become highly complex when different dynamic mechanisms are considered such as the material deformations, the suspension work or even the rider behavior during a race. However, to qualitatively evaluate the motorcycle behavior in straight running, at the first stage, the motorcycle will be approximated to a rigid body. Under this hypothesis, figure 2.1 shows a free-body diagram of the motorcycle during acceleration and deceleration. Then, the equation of equilibrium for a motorcycle in horizontal motion takes on specific characteristics whether the motorcycle is accelerating or braking, as described in equations 2.1 and 2.2 respectively. However, motorcycle dynamics requires the analysis of further aspects that are important for rider safety.

$$acc_{available} = \frac{F_p - F_D - F_{gx}}{m} \tag{2.1}$$

$$decc_{available} = \frac{F_b + F_D + F_{gx}}{m} \tag{2.2}$$

where m is the motorcycle and rider mass, F_D the drag force, F_p the driving force, F_b braking force and F_{gx} is the gravity force in x-direction due to positive track elevation. All these variables are illustrated in figure 2.1.

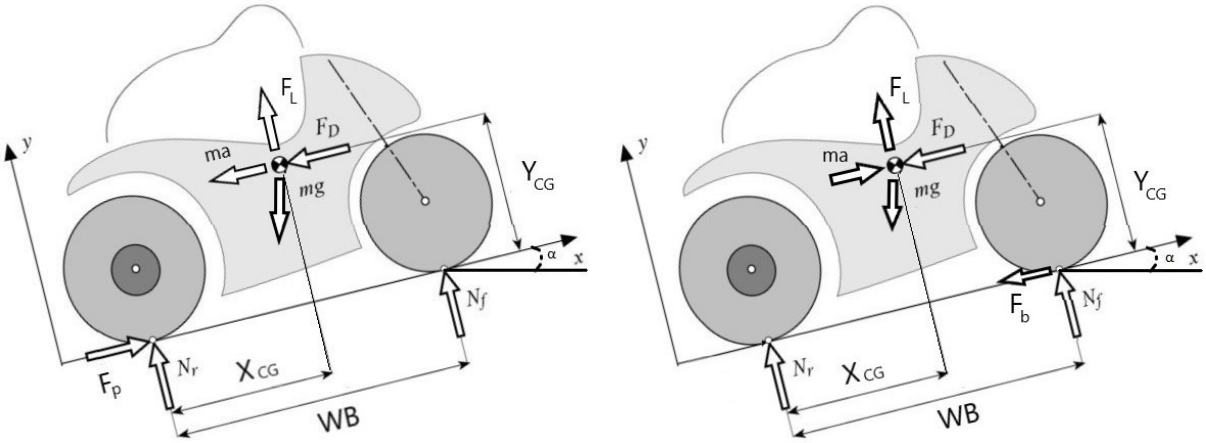

(a) Vector representation of acceleration motion

(b) Vector representation of deceleration motion

Figure 2.1: Vector representation of rectilinear motion forces

Over the last few years in MotoGP, riders struggle to handle these prototypes due to an excessive increase in the engine and braking power. As a result, the maximum power that a motorcycle can deliver is no longer limited by the engine or brakes. During acceleration or braking, two different limits constrain the brake or engine power delivery. The first one is the tire limit that occurs when the driving force or braking force exceeds the tire friction force limit ($F_a = \mu_{tire} N$). The second one is the limit when the wheel starts losing contact with the ground ($N = 0$). In particular, front-end-lift or wheelie is the definition for the front tire contact loss during acceleration ($N_f = 0$), which is the dissertation case study. Therefore, the maximum acceleration or deceleration that a motorcycle can perform to avoid the contact loss of the wheels with the ground is given by equations 2.3 and 2.4, respectively, with a more detailed explanation in [13] and Appendix A.

$$acc_{max} = \frac{(F_{gy} - F_L)X_{CG} - (F_D + F_{gx})Y_{CG}}{mY_{CG}} \tag{2.3}$$

$$dec_{max} = \frac{(F_D + F_{gx})Y_{CG} + (F_{gy} - F_L)(WB - X_{CG})}{mY_{CG}} \tag{2.4}$$

where X_{CG} and Y_{CG} are the distances to the gravity center, the WB is the motorcycle wheelbase and F_{gy} is the gravity force in y-direction due to positive track elevation. All the referred variables are illustrated in the free-body diagram in figure 2.1.

From Appendix B, not every Grand Prix categories are power limited under the front-end-lift effect, equation 2.3. For lower categories such as Moto3, the ratio between the driving force and total weight, which includes the motorcycle and rider weight, is not sufficient to overcome the wheelie limit. From the four motorcycles reviewed in Appendix B, for engine torque to total weight ratios larger than $0.48\ Nm/kg$ is worth examining whether the wings implementation is useful. Concerning the MotoGP prototypes, that ratio is sufficient to induce the loss of front tire contact with the ground. Consequently, the implementation of wings is suitable to increase the prototype's performance.

2.2 MotoGP Wings

In this section, the required downforce that the wings should produce to avoid front-end-lift will be estimated . To obtain an answer to this, in section 2.2.1, the optimum location to attach those wings will be discussed, and afterwards in section 2.2.2, the typical geometry of these wings will be analysed.

2.2.1 Optimum position

To determine the optimum wing location, the same equilibrium of momentum described in equations 2.3 and 2.4 is performed considering the wings effect.

$$acc_{maxwings} = acc_{max} + \frac{F_{lwings}X_{wings} - F_{dwings}Y_{wings}}{mY_{CG}} \tag{2.5}$$

$$dec_{maxwings} = dec_{max} + \frac{F_{dwings}Y_{wings} + F_{lwings}(WB - X_{wings})}{mY_{CG}} \tag{2.6}$$

where acc_{max} and dec_{max} are the maximum acceleration and deceleration that the motorcycle can perform to avoid losing the contact loss of the wheel with the ground, written in equations 2.3 and 2.4 respectively, X_{wings} and Y_{wings} are the wings position in the motorcycle about the rear axis and F_{lwings} and F_{dwings} are the forces produced by the same wings, as illustrated in figure 2.2.

From equations 2.5 and 2.6 the maximum acceleration and deceleration can not be satisfied simultaneously. The maximum acceleration is achieved for the maximum X_{wings} and minimum Y_{wings} and on the other hand, the maximum deceleration for the maximum Y_{wings} and the minimum X_{wings}. As a matter of principle, besides maximizing the motorcycle acceleration, the location was set not adversely to affect the deceleration. From equation 2.6, as long as the wings are located behind the front axis ($X_{wings} < WB$) the downforce produced by them would not compromise the deceleration process. Considering the MotoGP Technical Regulation 2019 [14] constraints and the physics in straight running, the optimum position to attach the wings would be aligned with the front tire axis at the minimum height possible, as illustrated in figure 2.2.

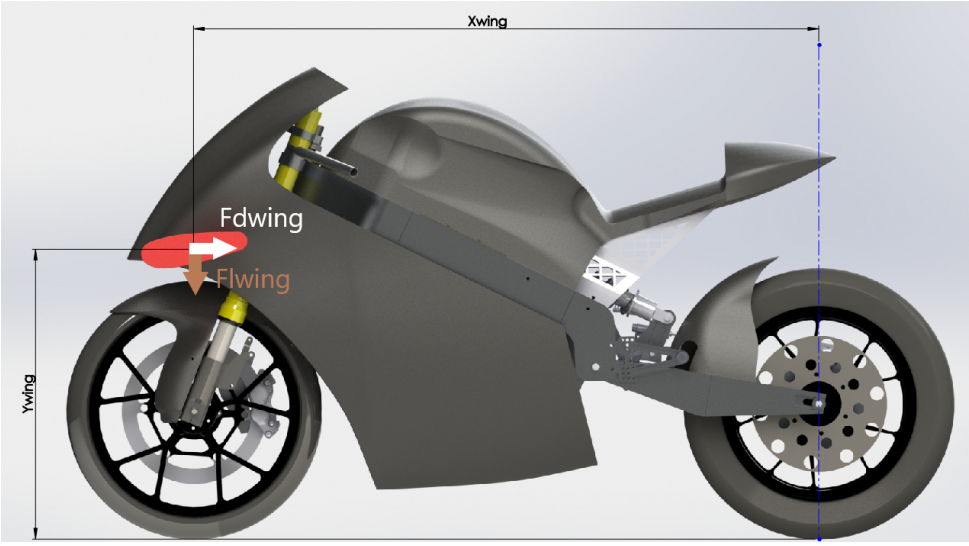

Figure 2.2: Lateral View over the university electric prototype TLMoto02e with the side-wings implemented.

2.2.2 Geometry

Depending on the MotoGP prototype manufacture, the side-wings can have different shapes and sizes. From the regulation in [14] the maximum wing-span is limited to $600\ mm$ for all prototypes, as illustrated in figure 2.3(a). As a result, from equation 2.7, the only way to manage the wing downforce production is either increasing the lift coefficient or the wing reference area.

$$F_{Lwings} = C_L \frac{1}{2} \rho U^2 A_{ref}; \tag{2.7}$$

Where C_L is the lift coefficient, U the velocity and A_{ref} the wing reference area.

To define the wing reference area, a chord length of $200\ mm$ will be assumed as a first approximation of a typical MotoGP wing. Additionally, the wing-span length must be determined to determine the wing reference area.

The motorcycle fairing is crucial to decrease the motorcycle drag. However, as illustrated in figure 2.3(a), the fairing forces the wings to be attached over the sides. As a result, not only the wing-span reduces significantly, but also from figure 2.3(b), the fairing shape decreases the total wing-span length through the wing-chord. Nonetheless, as a first approach, on the further CFD analysis will be assumed a rectangular wing with a span-length of $400\ mm$, $200\ mm$ at each side, as illustrated in figure 2.3(a).

2.2.3 Target Downforce

In this section, the downforce that a wing should produce to avoid the front-end-lift effect will be determined. Knowing the available acceleration from equation 2.1, the downforce is directly determined from equation 2.5, neglecting the wing drag force. For instance, the downforce was measured by the aid of the lap-simulator developed in the University team, TLMoto Team, for a motorcycle under these front-end-lift problems, racing at the Oulton Park circuit, whose results are plotted in figure 2.4.

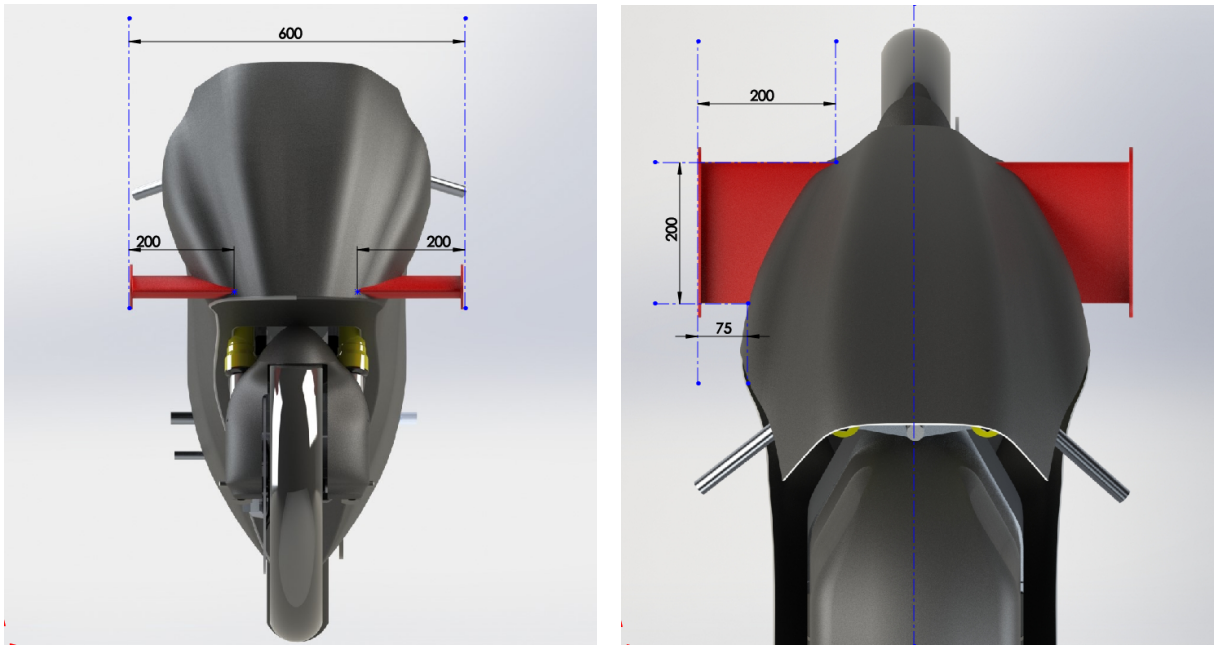

(a) Front view over the university electric prototype TLMoto02e (b) Top view over university electric prototype TLMoto02e

Figure 2.3: Front and top view over the university electric prototype TLMoto02e with the side-wings implemented

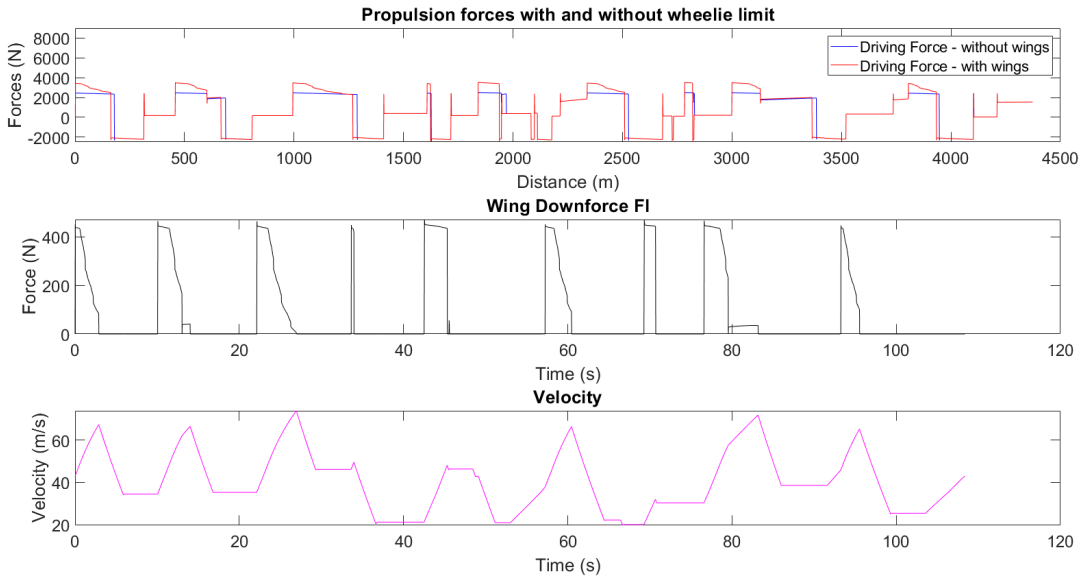

Figure 2.4: Matlab Driving force variation, wing down-force and velocity results for the most powerful motorcycle described in appendix B through a lap at Oulton Park circuit

Based on the acceleration time, the downforce is determined with the weighted averaged described in equation 2.8.

$$\overline{F_{Lwing}} = \frac{F_{Lwing}(meter_i) \times \Delta t(meter_i)}{\Delta t_{acc}} \tag{2.8}$$

where Δt_{acc} is the total acceleration time, and the numerator product represents the lift force integral over the time at each meter.

The average downforce that the wing should produce on a full lap at this circuit is approximately $200\ N$. For the geometry stated in the previous section and an average velocity of $40\ m/s$, the target lift coefficient of these wings would be approximately 2.8. For such short wings, this lift coefficient would be challenging to achieve. One of the solutions to produce such an amount of downforce would be attaching more wings to the motorcycle fairing. The number of wings to implement is a trade-off between increasing the motorcycle acceleration by implementing more wings and increasing the motorcycle top speed by implementing fewer wings reducing the motorcycle drag.

2.3 Flow Governing Equations

From a production line, passing through economic models to fluid dynamics, the conservation of a property is a standard concept. In a general form, the conservation law evaluates the flux of a quantity ϕ on a given volume, as written in equation 2.9.

$$\frac{\partial \phi}{\partial t} + \vec{\nabla}.\vec{F}(\phi) = Q_v + \vec{\nabla}.Q_s \tag{2.9}$$

where ϕ is the quantity to evaluate, Q_v and Q_s are source terms changing the property within the volume or within the bounds and F corresponds to the flux term.

The Navier-Stokes equations (NSE) are the conservation law of three properties: the mass (ρ), the momentum ($\rho\vec{v}$), and the energy (ρE). For an external isothermal incompressible flow, the NSE are reduced to the system of equations 2.10 in tensor notation.

$$\begin{cases} \dfrac{\partial u_i}{\partial x_i} = 0 \\ \dfrac{\partial u_i}{\partial t} + u_j \dfrac{\partial u_i}{\partial x_j} = \dfrac{\partial \tau_{ji}}{\partial x_j} - \dfrac{1}{\rho}\dfrac{\partial p}{\partial x_i} \end{cases} \tag{2.10}$$

Where u_i is the velocity in direction x_i, t the time, τ_{ij} the viscous stress tensor, p the pressure and ρ the fluid density. The viscous shear stresses represent the internal friction force of fluid layers against each other and is given below:

$$\vec{\tau_{ij}} = \nu \left(\frac{\partial u_i}{\partial x_j} + \frac{\partial u_j}{\partial x_i} \right) \tag{2.11}$$

where ν is the fluid kinematic viscosity.

2.3.1 Boundary Layer

For the problem at hand, the existence of a solid body within the viscous fluid domain leads to the emergence of a boundary layer (BL) near the wall region illustrated in figure 2.5. The BL regime is highly dependent on the balance between the convective term $\left(u_j \frac{\partial u_i}{\partial x_j}\right)$ and the diffusion term $\left(\frac{\partial \tau_{ji}}{\partial x_j}\right)$ in equation 2.10. The dimensionless number that controls this interaction is the Reynolds number represented

in equation 2.12, that balances the inertial over the viscous forces.

$$\frac{F_{inerc}}{F_{visc}} = \frac{\rho U \frac{dU}{dx}}{\mu \frac{d^2U}{dy^2}} \Rightarrow Re = \frac{\rho U_e \frac{U_e}{L}}{\mu \frac{U_e}{L^2}} = \frac{U_e L}{\nu} \tag{2.12}$$

Where U_e is the income flow velocity, L a length scale and ν the fluid kinematic viscosity.

Before getting into flows over complex shapes as airfoils, as an approximation, it will be established the Reynolds range that bounds the laminar and turbulent boundary layer based on the flat plate solution. The flat plate, in contrast to the airfoils, does not force any pressure gradient to the BL, simplifying the flow regime analysis. From [15] for Reynolds numbers of 10^5 order of magnitude, the flow is in a critical region where laminar to turbulent transition may occur anywhere.

From the graph plotted in figure 2.4, during a lap, the motorcycle ranges velocities between $20\ m/s$ and $80\ m/s$ corresponding to Reynolds numbers between $2.4 \cdot 10^5$ and $1 \cdot 10^6$, for a wing chord of $0.2\ m$. From the flat plate solution, this range corresponds to the critical region where transition mechanisms are responsible for important flow features.

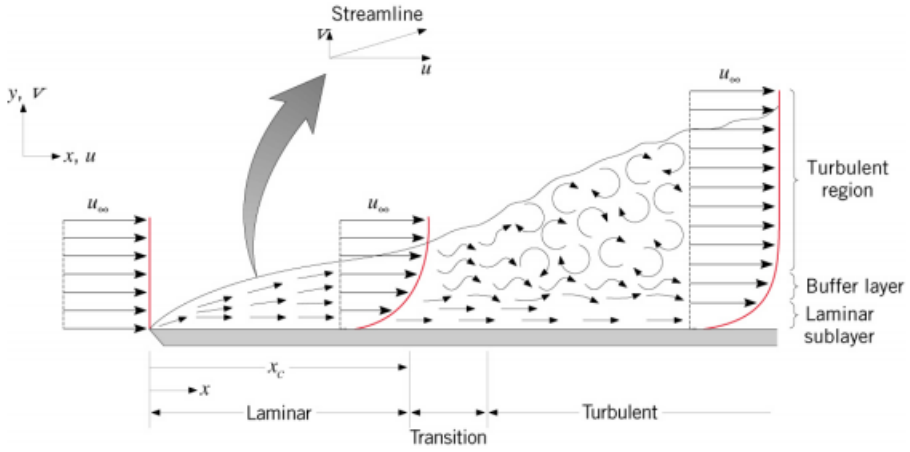

Figure 2.5: Boundary layer evolution over a flat plate, [16]

2.4 Case Study 1

In the present section, the order of magnitude of the fluid inertial forces due to the motorcycle accelerations and decelerations will be estimated.

Objects and fluids can not occupy the same physical space simultaneously. As a consequence, when an object changes the velocity, it deflects the surrounding fluid volume. This displaced mass is known as added mass or virtual mass and can be responsible for adding a significant amount of inertia to the system. This inertia is written in equation 2.13.

$$F_{am} = \rho V_{fluid} \frac{\partial U}{\partial t} \tag{2.13}$$

Where V_{fluid} is the displaced volume.

The displaced fluid will depend on the direction in which the wings are being accelerated. From [17], assuming that an ellipse is a good representation of an airfoil, in equation 2.14 is depicted the tensor diagonal of the added mass. From this system, the added mass of an airfoil accelerating at 0ºAoA on the streamwise direction is given by m_{11}.

$$\begin{cases} m_{11} = \rho\pi(t/2)^2 \\ m_{22} = \rho\pi(c/2)^2 \\ m_{12} = \rho((c/2)^2 - (t/2)^2)^2 \end{cases} \tag{2.14}$$

where c is the wing-chord and t is the wing maximum thickness.

From equation 2.13, the established added mass and the motorcycle velocity variations illustrated in figure 2.4, the inertial forces were determined and are depicted in table 2.1. Considering the reduced inertial forces order of magnitude is not expected a higher sensibility of the airfoil aerodynamic characteristics to the fluid inertial forces.

	$\rho\ [kg/m^3]$	$m_{11}\ [kg]$	$a\ [m/s^2]$	$F_{acc}\ [N]$
Acceleration	1.164	$5.3 \cdot 10^{-4}$	7	$3.7 \cdot 10^{-3}$
Deceleration			10	$5.3 \cdot 10^{-3}$

Table 2.1: Added mass and inertial forces under acceleration and deceleration

2.5 Case Study 2

From a dynamic point of view, a motorcycle can be considered as a rigid body connected to the wheels through an elastic system, [13]. As a result, the motorcycle is made up of three rigid bodies: the sprung mass, the rear unsprung mass and the front unsprung mass. In acceleration or braking because of the load transfer, the unsprung mass motion, where the MotoGP wings are attached, can be considered as the combination of vertical motion (bounce) and rotating motion (pitch), described in Appendix A.1.2 and illustrated in figure 2.6. As a first approach to this problem, the wings will be considered only prone to pitching motion.

In the pitching motion, there exists three mechanisms contributing to the global forces acting on the airfoil: the formation of a leading-edge vortex during the downstroke, the added mass reaction during the acceleration and deceleration phases, and the wake interaction, [18]. The present section aims to determine whether the respective contributions and interactions of the described mechanism participate in the lift force of a pitching airfoil as described in equation 2.15, from [18].

$$F_{lift} = F_{airfoillift} + F_{vortex} + F_{am} + F_{wc} \tag{2.15}$$

where $F_{airfoillift}$ is the airfoil lift force, F_{vortex} is the leading-edge vortex force, F_{am} is the added mass reaction and F_{wc} is the wake capture force.

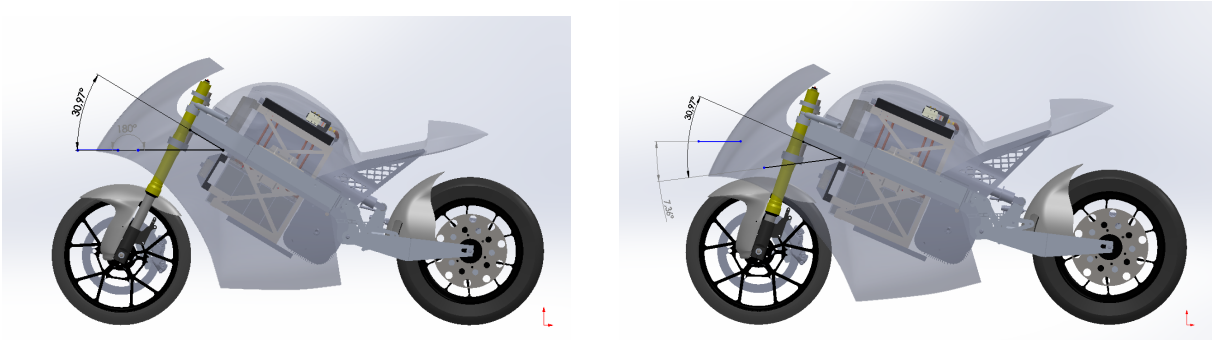

(a) TLMoto02e geometry change over acceleration

(b) TLMoto02e geometry change over deceleration

Figure 2.6: TLMoto02e geometry change over acceleration and deceleration

2.5.1 Vortex Shedding and Dynamic Stall

The first mechanisms occur when the airfoil exceeds stall incidence. The leading-edge vortex mechanism is highly prevalent in flapping flight whose angles of attack can achieve variations of 40º, and Strouhal numbers are in the range of 0.2–0.3, from [8] and [9]. For these oscillations, the Kutta-condition, [10], is not satisfied on the trailing edge and a vortex is shed forward to the leading-edge, as illustrated in figure 2.7. This mechanism increases the airfoil lift due to the high vortex velocities on the wing suction side. However, at a later stage, when this vortex is convected downstream, the wake interaction can cause a sudden lift decrease.

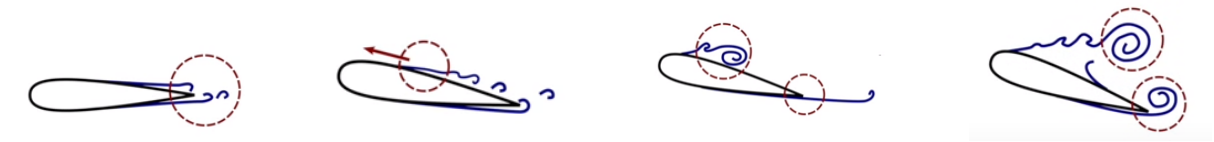

(a) Formation of trailing edge vortices

(b) The vortices are shed to the leading edge

(c) The vortices approach the leading edge

(d) At a later stage this vortex is convected downstream

Figure 2.7: Dynamic stall of an aerofoil in ramp-up motion [8]

For the problem at hand, the wings pitching motion frequencies are unpredictable since they are a consequence of the motorcycle accelerations and decelerations. Consequently, the wings will be studied out of the stall incidence and are not expected to experience those pitching mechanisms. However, since the boundary layer is sensible to transition mechanisms, the airfoil pitching could be responsible for important flow features.

To determine how far are the motorcycle pitching frequencies from the ones where the vortices formation occurs, the suspension frequencies and amplitudes were collected from a data acquisition system from a Yamaha R6 2009 on the best lap at Oulton Park Circuit.

According to the plot of figure 2.8, the front suspension can experience two different scenarios during a complete lap: a sudden variation after braking or accelerating, corresponding to the highest amplitudes, or an intermittent suspension oscillation of low amplitude, corresponding to the energy dissipation of shock absorber.

To determine the wing angle of attack, it is assumed a direct correlation to the front suspension from

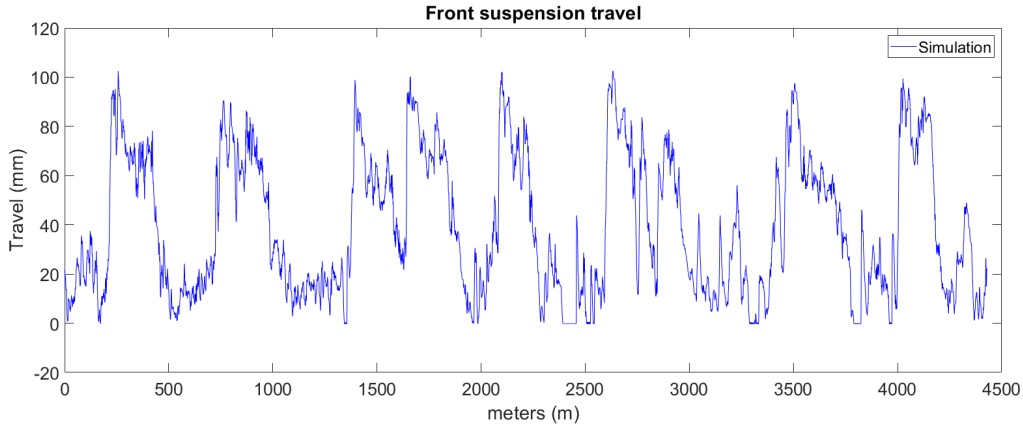

Figure 2.8: Matlab results and real data of suspension work for a Yamaha R6 2009 through a lap at Oulton Park circuit

the equation 2.16.

$$\alpha(t) = \frac{\alpha_{max}}{x_{travelmax}}(x_{travel}) + \alpha_0 \tag{2.16}$$

where α corresponds to the wing AoA and x to the suspension travel value.

Based on the university electric prototype, for the wing location illustrated in figure 2.6, the angle of attack variation between full extended suspension and completely compressed is approximately 4º. From the plot in figure 2.8 were selected two different track sections representatives of different working suspension frequencies, as illustrated in figures D.1(a) and D.1(b) in the appendix.

The Strouhal number for a pitching foil is defined in equation 2.17 below:

$$St = \frac{2fh_0}{U_e} \tag{2.17}$$

where f is the frequency of pitching, the h_0 is the maximum displacement traversed by the trailing edge and U_e the income velocity. By knowing the maximum pitching angle of attack and assuming that airfoil pitches around 25% of the chord, the h_0 can be written as:

$$h_0 = sin(AoA_{max})0.75c \tag{2.18}$$

Concerning the higher and lower pitching frequencies plotted in figures D.1(a) and D.1(b) in the appendix, the Stouhal number range is depicted in table 2.2. Similarly to the previous section, the pitching motion is not expected to interfere with the airfoil aerodynamic characteristics since the Strouhal ranges numbers are four orders of magnitude lower than the required to enhance the vortex shedding mechanisms.

	$f[Hz]$	$U_e\ [m/s]$	$Chord\ [m]$	AoA_{max} [º]	$h_0\ [m]$	St
High Amplitude	0.6	30	0.2	2	$5.2 \cdot 10^{-3}$	$2.2 \cdot 10^{-4}$
Low Amplitude	3.1			0.5	$1.3 \cdot 10^{-3}$	$2.7 \cdot 10^{-4}$

Table 2.2: Pitching characteristics for the motorcycle wings

2.5.2 Added Mass

This section aims to estimate the fluid inertia forces during the wing pitching motion. From [19], to determine this inertia forces from equation 2.13, the maximum angular acceleration can be approximated by the trailing-edge linear acceleration as:

$$a_{TE,p} = -h_0 \alpha_0 \omega^2 sin(\omega t) \tag{2.19}$$

where α_0 is the airfoil AoA, ω the angular frequency, t the time and h_0 is the amplitude vertical distance measured on the trailing edge.

From the values presented in table 2.2 and the added mass m_{12} of the system of equations 2.14, the inertia forces are determined in table 2.3. Similarly to the acceleration inertial forces, the pitching motion should not be a concern to determine the airfoil aerodynamic characteristics.

	$m_{33}\ [kg]$	$a\ [m/s^2]$	$F_{acc}[N]$
High Amplitude	$1.1 \cdot 10^{-3}$	$8.2 \cdot 10^{-2}$	$9.2 \cdot 10^{-5}$
Low Amplitude		0.5	$5.8 \cdot 10^{-4}$

Table 2.3: Added mass under pitching motion

In conclusion, either the vortex shedding mechanism or the added mass should not play a role in the airfoil aerodynamic characteristics. Nevertheless, the Reynolds numbers range is within the critical regime and it has to be determined whether the pitching motion affects the boundary layer transition mechanisms or not.

Chapter 3

Mathematical Models and Numerical Methods

3.1 Models

A model is a physical, mathematical, or otherwise logical representation of a system, entity, phenomenon, or process (DoD 1998). Both motorcycle and fluid dynamics are non-linear systems, the reason why it is mandatory to establish some approximations to reduce the system complexity and predict their behaviour. According to fluid dynamics principles, the modelling is highly dependent on flow characteristics. It was already established that in the present problem, turbulence is expected. Turbulence can be solved in different ways, computed directly using the Direct Numerical Simulation (DNS), by approximating the turbulent field above a specific length scale when using the Large Eddy Simulation (LES) or by averaging the turbulence in time using the Reynolds Averaged Navier-Stokes (RANS). RANS is the most used approach to compute turbulent flow in engineering applications. It requires lower computational power than DNS and LES and provides a satisfactory accuracy for most turbulent problems. Consequently, the focus of this dissertation will be the RANS modelling approach.

3.1.1 Reynolds Averaged Navier-Stokes Equations (RANS)

Reynolds proposed a statistical approach to solve the NSE. Considering that the fluctuation of a property ϕ_i characterizes a turbulent flow, the statistical value of this property is expressed by the sum of a mean component ($\overline{\phi_i}$) and fluctuations components (ϕ_i'), equation 3.1.

$$\phi_i = \overline{\phi_i} + \phi_i' \tag{3.1}$$

Applying this composition to the NSE, the RANS can be written as:

$$\begin{cases} \dfrac{\partial \bar{u}_i}{\partial x_i} = 0 \\ \dfrac{\partial \overline{u_i}}{\partial t} + \overline{u_j}\dfrac{\partial \bar{u}_i}{\partial x_j} + \dfrac{\partial}{\partial x_j}\left(\overline{u_i' u_j'}\right) = \nu \dfrac{\partial^2 \bar{u}_i}{\partial x_j^2} - \dfrac{1}{\rho}\dfrac{\partial \overline{p}}{\partial x_i} \end{cases} \tag{3.2}$$

By comparing equations 3.2 and the NSE 2.10, the average process results in the emergence of a new term, the Reynolds stresses $\overline{u_i' u_j'}$. The Reynolds stress tensor introduces new variables to the system of equations that have no additional equations to be determined. As a result, the RANS becomes an undetermined system and depends on additional equations. In the further sections, the models coupled with the RANS to determine the Reynolds stress term will be presented.

3.1.2 Turbulence Models

Reynolds stress is the main concern of turbulence in engineering problems. Boussinesq proposed an approximation to the Reynolds stress tensor by assuming a direct proportionality to the velocity gradients, as shown in equation 3.3.

$$-\overline{u_i' u_j'} = \nu_t \left(\frac{\partial \overline{u_i}}{\partial x_j} + \frac{\partial \overline{u_j}}{\partial x_i} \right) \tag{3.3}$$

where ν_t is the turbulent eddy-viscosity.

Different turbulence models use the Boussinesq assumption to calculate the eddy viscosity. The Menter shear stress transport $\kappa - \omega$ (SST $\kappa - \omega$), from [20] and [21], is the widely used turbulence model for this applications with two blended models, figure 3.1: The $\kappa - \epsilon$ model, developed by Jones and Launder [21], which is mainly implemented for fully turbulent flows, sensitive to the free-stream turbulence, and the $\kappa - \omega$, developed by Wilcox [21], that reveals a good behavior on the near-wall region able to predict flow separations. $\kappa - \omega$ and $\kappa - \epsilon$ are two equations models based on the transport

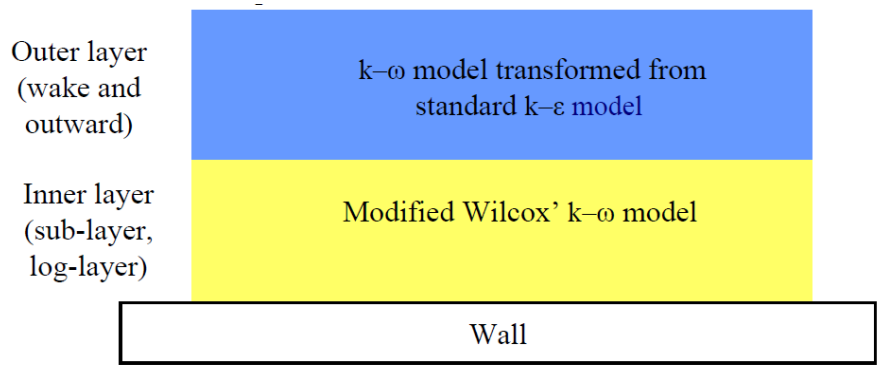

Figure 3.1: Menter SST $\kappa - \omega$ model typology

of the quantities κ, ω and ϵ. The SST $\kappa - \omega$ similarly is a two-equation model, governed by equations 3.4 and 3.5, which uses blending functions F_1 to change between $\kappa - \omega$ and $\kappa - \epsilon$ depending on the wall

distance.

$$\rho\frac{\partial\kappa}{\partial t} = \tau_{ij}\frac{\partial\overline{u_i}}{\partial x_j} - \beta^*\kappa\rho\omega + \frac{\partial}{\partial x_j}\left[(\mu + \mu_t\sigma_\kappa)\frac{\partial\kappa}{\partial x_j}\right] - \frac{\partial(\rho u_i\kappa)}{\partial x_j} \tag{3.4}$$

$$\rho\frac{\partial\omega}{\partial t} = \frac{\gamma}{\nu_t}\tau_{ij}\frac{\partial\overline{u_i}}{\partial x_j} - \beta\rho\omega^2 + \frac{\partial}{\partial x_j}\left[(\mu + \mu_t\sigma_\omega)\frac{\partial\omega}{\partial x_j}\right] - \frac{\partial(\rho u_i\omega)}{\partial x_j} + 2\rho(1-F_1)\frac{\sigma_{\omega 2}}{\omega}\frac{\partial\kappa}{\partial x_j}\frac{\partial\omega}{\partial x_j} \tag{3.5}$$

Where the first term on the right side is the production of turbulence kinetic energy (κ), the second is the transport property dissipation, the third stands for the property diffusion and the forth is convection. The equation 3.5 contains an additional term associated with the blend function responsible for changing between the $\kappa-\omega$ and the $\kappa-\epsilon$ model. The variables $\beta^*, \sigma_k, \gamma, \sigma_\omega$ and $\sigma_{\omega 2}$ are constants, and the ω is the turbulence specific rate of dissipation.

Then the eddy-viscosity, from equation 3.6, is used to calculate the Reynolds stress with equation 3.3, and so closing the RANS equations.

$$\nu_t = \frac{a_1 k}{\max(a_1\omega, \Omega F_2)} \tag{3.6}$$

Where a_1 is a constant, Ω the vorticity magnitude and F_2 is another blending function.

3.1.3 Transition Models

The turbulence models, as SST $\kappa-\omega$, were not developed to predict transition between flow regimes, [22] and [23]. This model estimates the transition location based on the model turbulence production. The coupling of a transition model aims to control turbulence production locally. The transition model used in this dissertation is the $\gamma - Re_\theta$, a two equations model, with one transport equation for the intermittency γ, equation 3.7, which triggers the transition in BL and another one for the local momentum thickness Reynolds Re_θ, equation 3.8, which controls the transition location.

$$\frac{\partial\overline{Re_{\theta t}}}{\partial t} = P_{\theta t} + \frac{1}{\rho}\frac{\partial}{\partial x_i}\left[\sigma_{\theta t}(\mu + \mu_t)\frac{\partial\overline{Re_{\theta t}}}{\partial x_i}\right] - u_i\frac{\partial\overline{Re_{\theta t}}}{\partial x_i} \tag{3.7}$$

$$\frac{\partial\gamma}{\partial t} = P_\gamma - E_\gamma + \frac{1}{\rho}\frac{\partial}{\partial x_i}\left[(\mu + \frac{\mu_t}{\sigma_f})\frac{\partial\gamma}{\partial x_i}\right] - u_i\frac{\partial\gamma}{\partial x_i} \tag{3.8}$$

where P_γ and $P_{\theta t}$ are the properties production, the E_γ corresponds to the γ destruction term, and $\sigma_{\theta t}$ and σ_f are constants. The last term and the second-to-last are respectively, the convection and diffusion of the correspondent property.

From [24], the Re_θ has an essential role in the communication between the boundary layer and the freestream flow. That way, free-stream conditions, such as the viscosity ratio ($\frac{\mu_t}{\mu}$) or the turbulence intensity (Tu) are crucial to the transition prediction.

The transition model requires the calculation of the shear stress at the wall by definition $\left(\tau_w = \mu\frac{\partial U}{\partial y}_{y=0}\right)$ at the viscous sub-layer [24]. As a result, the first element near the wall region should be caught within this layer. Typically for proper modelling the dimensionless wall distance y^+ of the first element near the wall should be lower than one, [24].

3.2 Wall Treatment

At this stage, it is already known that flow is highly dependent on the transition process and consequently, the near-wall region must be treated with caution. From the previous section, the transition model requires the dimensionless distance to the wall, equation 3.9, to be lower than one.

$$y^+ = \frac{u_\tau y}{\nu}; \tag{3.9}$$

$$u_\tau = \sqrt{\frac{\tau_w}{\rho}} = U_e\sqrt{\frac{C_f}{2}} \tag{3.10}$$

From the relations 3.9 and friction velocity 3.10 the effective dimension of the first element near the wall is given below:

$$\frac{y_2}{c} < \frac{1}{Re_{chord}}\sqrt{\frac{2}{C_f}} \tag{3.11}$$

The minimum element size is given for the maximum friction coefficient (C_f) value over the airfoil. From the literature [10], the friction coefficient assumes different values for laminar and turbulent boundary layer, respectively equations 3.12 and 3.13.

$$C_{flaminar} = \frac{0.664}{\sqrt{Re_x}} \tag{3.12}$$

$$C_{fturbulent} = \frac{0.0592}{\sqrt[5]{Re_x}} \tag{3.13}$$

The friction coefficient for the turbulent boundary layer is expected to be higher, equation 3.13, which requires to know the transition location. As a first approach, it was performed a simulation in the software *XFoil6.99* to a NACA0012, which is shown in figure 3.2, for an average Reynolds number $Re = 5 \cdot 10^5$ at a 0º AoA.

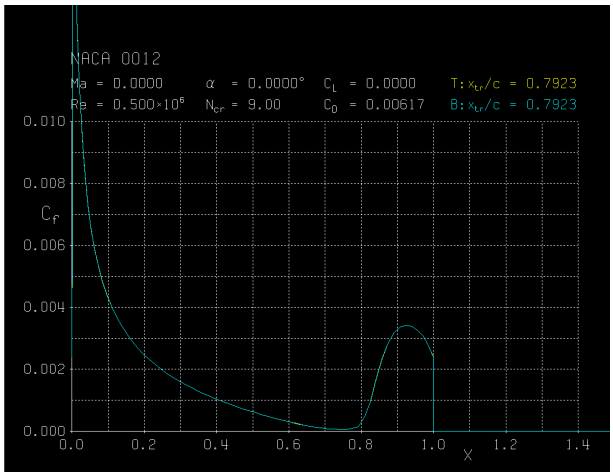

Figure 3.2: XFoil NACA0012 Friction coefficient through the chord length for $Re = 5 \cdot 10^5$

Assuming that transition occurs at 79% of the chord from the XFoil plot in figure 3.2, the maximum friction coefficient is approximately $3.5 \cdot 10^{-3}$. As a result, from equation 3.11, the first element near the

wall region should be smaller than $8.43 \cdot 10^{-6} m$, ensuring that the transition model calculates the shear stress at the wall properly. This condition will be verified in section 4.1.2.

3.3 Discretization Schemes and Solution Algorithms

To determine the flow properties around the wing, the fluid domain must be discretized with finite volumes that form a grid structure. As a consequence, the transport equations 3.2, 3.4, 3.5, 3.7 and 3.8 must be discretized in space and for unsteady simulation also in time. The selected discretization schemes are detailed in table 3.1 with second-order schemes in space discretization and first-order in time.

Besides the accuracy of a finite volume solution being related to how the flow equation is discretized, it is also essential to establish how they were solved. The solution of the numerical results was accomplished using a segregated iterative method based on the SIMPLE algorithm [25].

	Scheme
Convection $\gamma - Re_\theta$	2nd-order upwind
Convection $SST\ \kappa - \omega$	2nd-order upwind
Convection Momentum equation	2nd-order upwind
Unsteady $\left(\frac{\partial}{\partial t} \neq 0\right)$	1nd-order Implicit

Table 3.1: Discretization schemes applied to the NSE to solve the convection flow problem

Chapter 4

2D-RANS NACA0012

Two-dimensional analyses are a useful tool as the first approach for real wing problems. In this chapter, it will be performed a parametric analysis to an airfoil NACA0012 using the commercial software Starccm+ version 13.06. Section 4.1 presents the grid developed with the main domain characteristics as well as an estimation of the discretization error associated with this grid. In section 4.2, the transition mechanism sensibility will be discussed for different airfoil angles of attack, different inlet turbulence conditions and different Reynolds numbers. Afterwards in section 4.3, the airfoil aerodynamic characteristics will be outlined using steady and unsteady solvers. At the end of this chapter, in sections 4.4 and 4.5, the numerical results regarding the two case studies about the wings acceleration, deceleration and pitching motion will be discussed.

4.1 2D-Grid

The domain and grid definition represent an important step to determine the final solution of the problem accurately. The present grid is a quadrilateral Multi-block grid, as illustrated in figure 4.1(a), with a body-fitted C-Mesh structured grid near the wall, as illustrated in figure 4.1(b). These quadrilateral structures are built to be aligned with the flow direction, leading to more accurate results and a better solution convergence. In addition, these meshes are highly controllable over the high gradient zones near the wall region. Regardless of its benefits, structured meshes tend to be heavy and time-consuming in contrast to other grid structures. Given the fact it is a two-dimensional analysis, the structured meshes can be handled with the available computational power.

4.1.1 Domain

The proper domain size will be determinant to an accurate measurement of the airfoil aerodynamic characteristics. Throughout the simulations, the wing AoA will be handled from the inlet velocity condition rather than adjusting the grid. As a result, for all AoA and velocity values, the grid will remain static. Consequently, not only the numerical error will increase due to the grid misalignment with the income flow but also requires an additional concern regarding the location where the airfoil wake is being convected.

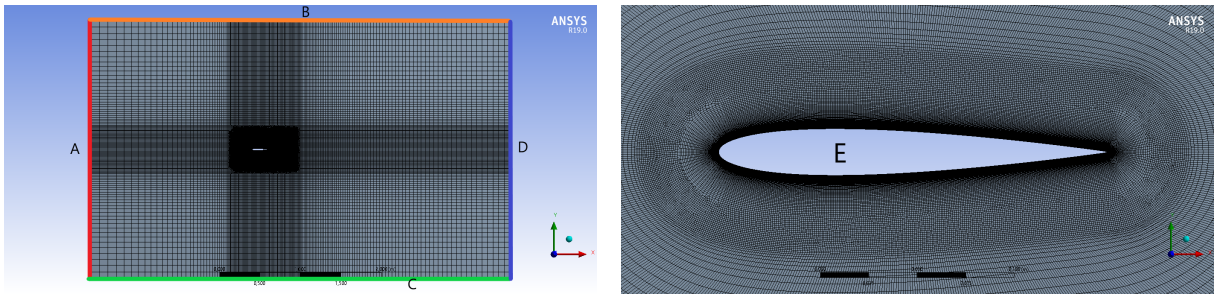

(a) Multi-grid block grid division around NACA0012

(b) Near wall body-fitted C-Mesh around NACA0012

Figure 4.1: Two-dimensional block grid around the NACA0012

After several attempts, the selected domain is illustrated in figure 4.1, with the respective boundary condition and sizing presented in table 4.1.

	A	B	C	D	E
Boundary Condition	Velocity Imposed			Pressure Imposed	No-slip
Distance from the LE	$10 \cdot c$	$8 \cdot c$	$8 \cdot c$	$15 \cdot c$	-

Table 4.1: Domain size and boundary conditions. where c stands for the chord length, LE stands for the airfoil leading-edge and the letters A, B, C, D and E are identified in figure 4.1

Concerning the near-wall region, the boundary layer is highly dependent on transition and separation phenomena. The models described in chapter 3 will require special near-wall treatment. In section 3.2 the required cell size of the first element near the wall region was computed. Apart from this restriction required from the transition model, the boundary layer must be caught within a considerable range of volumes and on its full size. Assuming that the boundary layer is turbulent from the leading edge, from equation 4.1 [10], for a $Re = 5 \cdot 10^5$ and the airfoil chord of $0.2\ m$, the prismatic layer near the wall region illustrated in figure 4.1(b) should be at least $5\ mm$ thick. As a result, the block offset was set to $20\ mm$ and the elements' growth rate followed a geometric progression with a stretching factor of 1.2. As the blocks stepped aside from this region, the grid remains growing at the same rate but with different cell sizes, ensuring that the transition between blocks is smooth.

$$\delta_{turb} = \frac{0.37x}{\sqrt[5]{Re_x}} \tag{4.1}$$

4.1.2 Wall distance verification

The present section aims to verify whether the predicted wall distance of the first element near the wall region in section 3.2 is within an acceptable range to ensure the correct operation of the transition model. In figure 4.2 are plotted the y^+ distances of the first element near the airfoil for three different Reynolds numbers at two different angles of attack. As observed from the plotted results, the size of the first element near the wall region complies with the required condition of $y^+ < 1$ for most of the airfoil. As a result, it can be stated that the grid is catching the viscous sub-layer in the near-wall region, ensuring that the transition model calculates the shear stress at the wall properly.

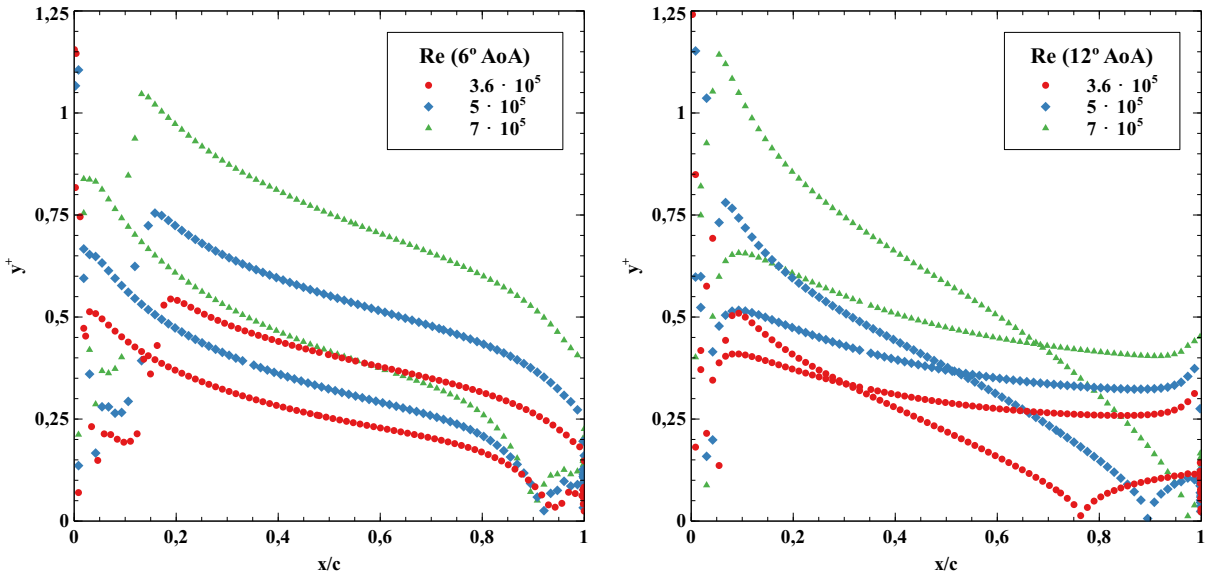

(a) (b)

Figure 4.2: NACA0012 y^+ distribution for $6\ ^\circ$ and $12\ ^\circ$ AoA along the dimensionless chord for $Re = 3.6 \cdot 10^5, 5 \cdot 10^5, 7 \cdot 10^5$

4.1.3 Discretization Error Assessment

Apart from the domain size, the grid has to be dense enough to ensure that all the essential features of the flow are adequately solved. Although, to accomplish enough resolution to accurately determine the airfoil aerodynamic characteristics, a successive analysis to similar geometric grids with different levels of refinement would be required. Since this procedure falls out of the dissertation scope, the grid illustrated in figure 4.1 was established based on other grids from [26] and [2].

Any computational solution coming from an iterative process on a discretized domain will have an inherent error. Therefore, a property ϕ took from a numerical solution must have an uncertainty U_ϕ concerning the exact solution ϕ_{exact}, equation 4.2. However, for the NSE in turbulent flows, there is no exact solution available and the goal is to define an interval that contains the exact solution with 95% confidence, [27].

$$\phi_i - U(\phi_i) \leq \phi_{exact} \leq \phi_i + U(\phi_i) \tag{4.2}$$

The uncertainty is divided into three main sources of error:

- The round-off error stems from the machine accuracy. For the present analysis, the double-precision calculation is being used, i.e. 14 digits, which is enough condition to neglect the round-off error.

- The discretization error is a consequence of the approximations made to transform the partial differential equations into a system of algebraic equations, relying on the grid refinement. For most CFD applications, the numerical error source relies on the discretization error, which will be the primary concern of the present assessment.

- The iteration error is a consequence of the non-linearity of the mathematical equations solved by CFD. For residuals levels of two orders of magnitude below the discretization error, the iterative error can be neglected, from [28].

By ensuring that neither the round-off error nor the iterative error affects the discretization error, the Richardson Extrapolation will be implemented to determine the discretization error, as written in equation 4.3.

$$\delta_{RE} = \phi_i - \phi_0 = \alpha h_i^p \tag{4.3}$$

where p is the order of convergence, h_i the relative grid spacing, α a constant and δ_{RE} the discretization error.

To close the equation 4.3, at least three solutions ϕ_i are required, i.e. three different grids. In the present work, the other two solutions were taken from more sparse and thinner grids with a refinement reason of 1.4. Then, the relative grid spacing h_i for unstructured grids is estimated from equation 4.4.

$$h_i = \frac{\Delta x_i}{\Delta x_1} \; ; \; \Delta x_i = \left(\frac{1}{N_{celli}} \right)^{\frac{1}{n_d}} \tag{4.4}$$

where n_d is the space dimension (for two-dimensional analysis $n_d = 2$), N_{celli} is the total number of cells of the grid i and the subscript one is the solution of the thinnest grid.

In table 4.2 are depicted the lift coefficient, pressure and friction drag coefficients for the three different grids, on NACA0012 at an angle of attack of two degrees and Reynolds number of $3.6 \cdot 10^5$.

Grid	cells nº	h_i	C_l	$C_{dp} \cdot 10^3$	$C_{df} \cdot 10^3$
1	53730	1.41	0.216	3.557	3.776
2	106859	1.41	0.217	3.417	3.781
3	213385	-	0.217	3.374	3.782

Table 4.2: Aerodynamic characteristics for different structured grids sizing with $Re = 3.6 \cdot 10^5$ at $2\ ^\circ$ AoA.(Solution Verification of NACA0012)

From the results depicted in table 4.2, the type of convergence and the order of convergence of the three properties will be evaluated. The type of convergence is measured with the convergence ratio R estimated by equation 4.5 from [29].

$$R = \frac{\phi_2 - \phi_1}{\phi_3 - \phi_2} \tag{4.5}$$

Where ϕ_1, ϕ_2, ϕ_3 correspond to solutions with the fine, medium and coarse grid spacing, respectively.

Assuming a uniform grid refinement ratio h_i, the order of convergence p is given by equation 4.6.

$$p = \frac{log(\frac{\phi_3 - \phi_2}{\phi_2 - \phi_1})}{log(r)} \tag{4.6}$$

Where r stands for the grid refinement ratio $\left(r = \frac{h_i}{h_1} \right)$ which is assumed constant for the present grid.

To reliably determine the type of convergence and the order of convergence, more grid solutions would be needed. Otherwise, a small amount of data could mislead the solution tendency. For in-

	C_l	C_{dp}	C_{df}
R	0.46	0.30	0.49
P	2.23	3.47	2.04
δ	$5.17 \cdot 10^{-4}$	$4.23 \cdot 10^{-5}$	$1.88 \cdot 10^{-6}$

Table 4.3: Errors and order of convergence associated with the different properties of the structured mesh for $Re = 3.6 \cdot 10^5$ and $2\,^\circ$ AoA (NACA0012).

stance, from the depicted results in table 4.3 and from [28], the properties in study exhibit a monotonic convergence with convergence ratios between zero and one.

For a second-order method, the convergence order should be lower than 2. From table 4.3, the observed order of convergence for lift and friction coefficients is closer to two, although the pressure drag fell out within the acceptable range.

Overall, since the goal is to determine the airfoil lift properties, an acceptable discretization error to proceed with the following simulations was accomplished.

4.2 Flow characteristics

At moderate Reynolds numbers, different transition mechanisms are responsible for determining the flow characteristics. For the problem at hand, the boundary layer transition occurs through a separation bubble. The separation of a boundary layer depends upon three mechanisms: the pressure gradient imposed on the flow, flow diffusion dependent on the boundary layer regime and momentum close to the wall. To occur flow separation an adverse pressure gradient is required, which is commanded by the airfoil shape. However, either the flow diffusion and the momentum close to the wall can have an important role in this mechanism.

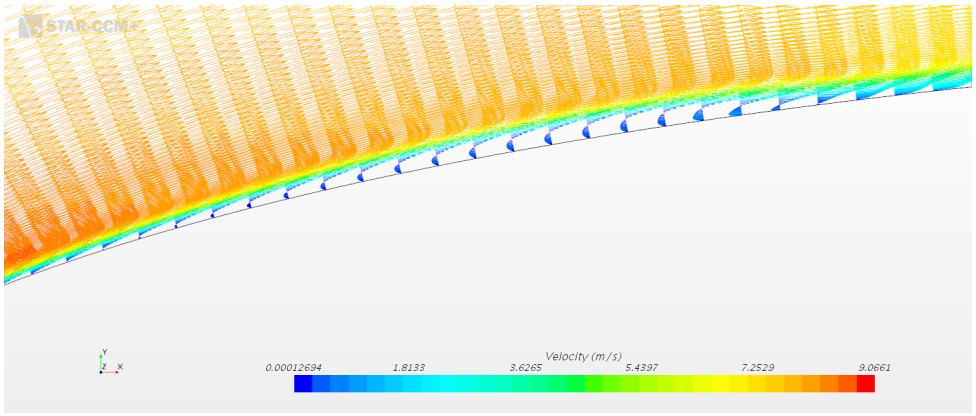

Figure 4.3: Vector scene on the near-wall region with a separation bubble close to the leading edge at the upper surface

The separation bubble phenomenon presented in this section is caused by an adverse pressure gradient, due to the airfoil shape, acting on a laminar boundary layer. Since the laminar boundary layer is less diffusive than turbulent boundary layers, it is more likely to separate. After separation, the

free-shear layer promotes the boundary-layer transition and afterwards, due to the higher diffusivity of turbulent boundary layers, the flow reattaches to the surface. From [10], this last phenomenon is known as the Coanda effect, relying on the entrainment velocity. To illustrate this effect the velocity vectors near the wall region were plotted in figure 4.3. Throughout this section, the influence of different angles of attack, Reynolds number and inlet condition on the separation bubble process will be discussed.

4.2.1 Angle of Attack Sensibility

In this section, the sensibility of the separation bubble mechanism will be studied for different angles of attack values and Reynolds number of $5 \cdot 10^5$. The convergence of these results was achieved by using unsteady solver, later on explained in section 4.3.2, with the settings described in table 4.4.

The separation bubble as a transition mechanism of the boundary layer can be observed on the airfoil skin friction coefficient plotted in figure 4.4. For a NACA0012 at $0\,^\circ$ the boundary layer develops laminar until 65% of the chord and by a separation bubble mechanism reattach turbulent at 90% of the chord for the upper and lower surfaces. As long as the airfoil angle of attack increases, the adverse pressure gradient increases on the suction side, as plotted on the pressure coefficient in figure 4.6, and the separation bubble moves towards the leading-edge, as observed in figure 4.5.

On the other hand, from the plotted results of the pressure coefficient in figure 4.6, as long as the airfoil angle of attack increases, on the airfoil pressure side is observed a favourable pressure gradient. As a result, the separation bubble moves forward to the trailing-edge until it vanishes at $10\,^\circ$, as illustrated figure 4.5.

In conclusion, the separation bubble mechanism shows high sensibility to the pressure gradients enforced either by the airfoil shape and the airfoil angle of attack.

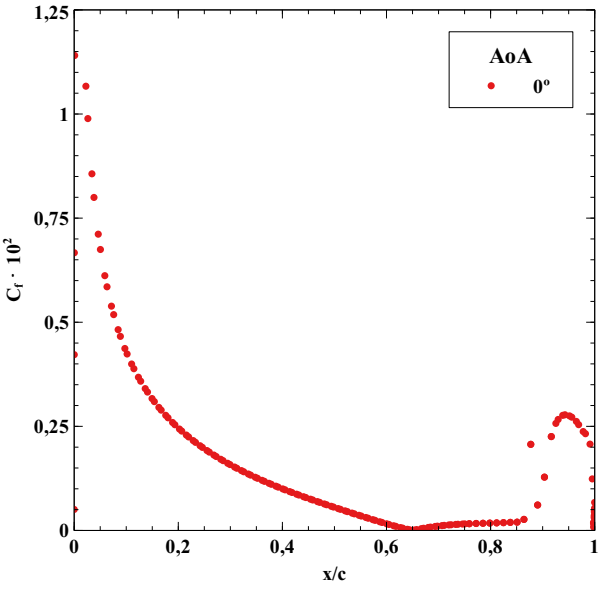

Figure 4.4: NACA0012 $|C_f|$ distribution at $0\,^\circ$ AoA for $Re = 5 \cdot 10^5$.

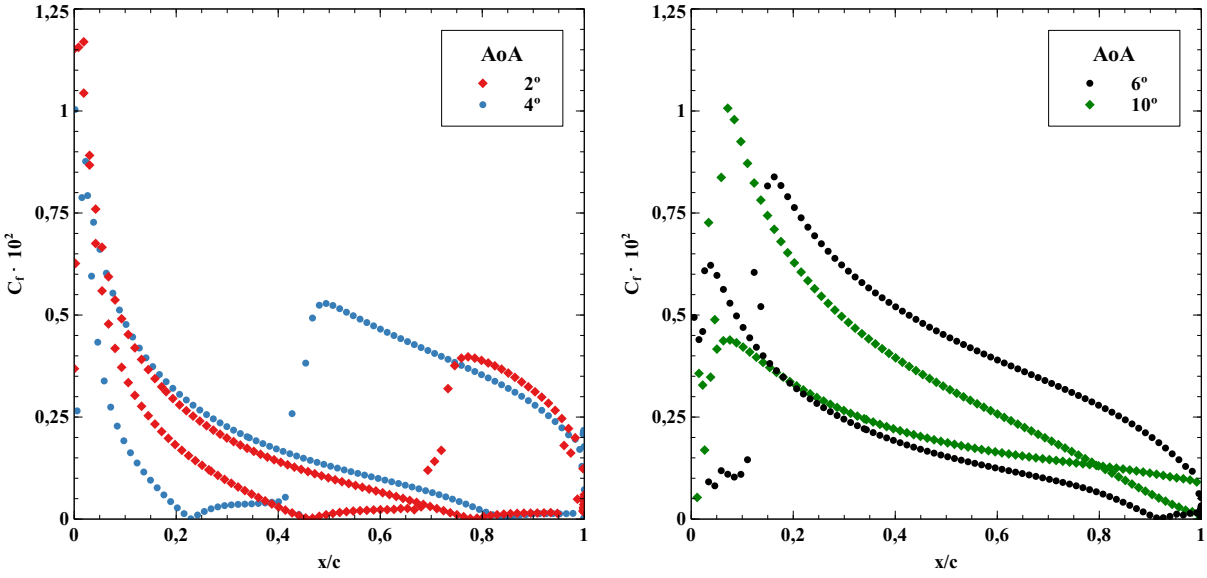

(a) (b)

Figure 4.5: NACA0012 $|C_f|$ distribution between $2\,^\circ$ and $10\,^\circ$ AoA for $Re = 5 \cdot 10^5$

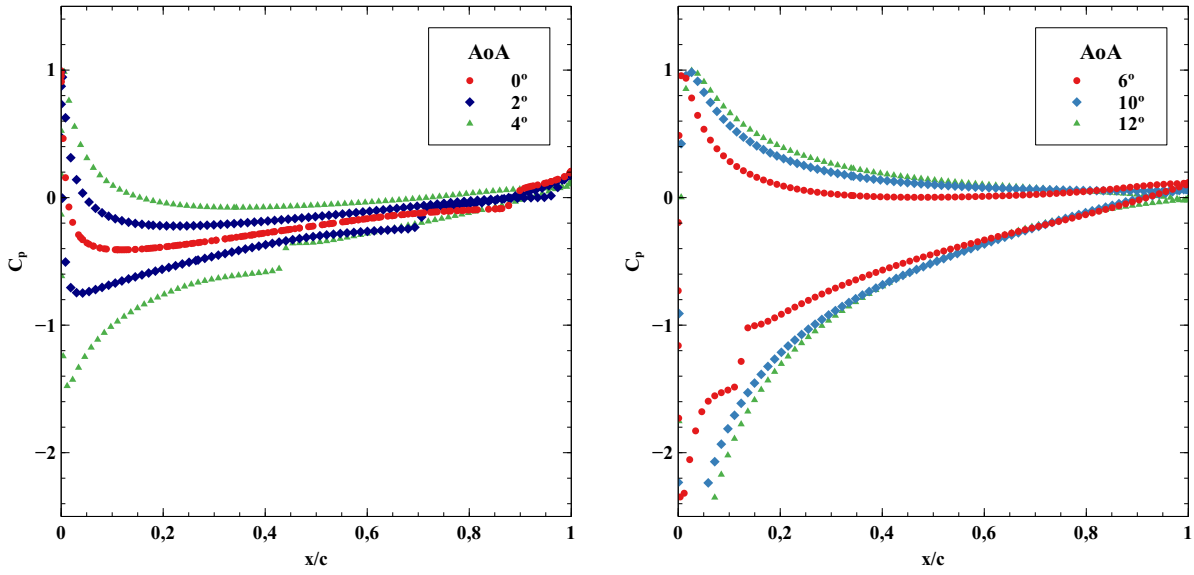

(a) (b)

Figure 4.6: NACA0012 C_p distribution between $0\,^\circ$ and $12\,^\circ$ AoA along the dimensionless chord for $Re = 5 \cdot 10^5$

4.2.2 Turbulence Level Sensibility

The stall is an aerodynamic condition in which a wing exceeds its given critical angle of attack. Depending on the airfoil thickness and flow conditions, this region can be ruled by a thin airfoil stall, a leading-edge stall or a trailing-edge stall, [10].

The airfoil thickness will determine the leading-edge curvature smoothness. For thick airfoils, as the NACA0012, the airfoil stall can occur due to the separation bubble burst (Leading-edge stall) or

a turbulent separation starting from the trailing-edge (Trailing-edge stall). For the trailing-edge stall, the flow separation begins near the airfoil trailing-edge moving towards the leading-edge. When this separated flow fills approximately 50% of the chord, the airfoil stall. On the other hand, for the leading-edge stall, the flow separates near the leading-edge due to the separation bubble burst. The main differences between both stall mechanisms are the lift decrease. While on the trailing-edge stall, the lift decreases progressively, on the leading-edge stall, the airfoil experience a sudden lift decrease. In this section, the sensibility of the boundary layer near the stall incidence will be studied for a thick airfoil to different turbulence levels from the income flow.

From the friction coefficient plot in figure 4.9, a conventional trailing-edge separation bubble is observed formed as the angle of attack increases till the point of complete separation when the separation takes more than 50% of the airfoil chord at $14\,^{\circ}$. However, by decreasing the viscosity ratio of the income flow, the lower diffusion of the free-shear layers do not allow the flow transition. As a result, the flow does not reattach to the airfoil and the separation bubble burst. This effect can be seen in figures 4.7 and 4.8 for different levels of viscosity ratios from the income flow.

As a conclusion, near the stall region, where the pressure gradients are highly intense, the turbulence levels of the free-stream flow can induce different stall mechanisms.

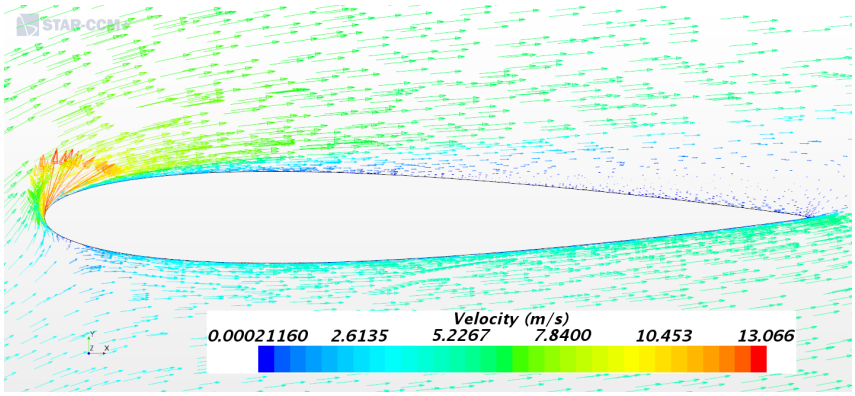

Figure 4.7: NACA0012 velocity vector scene at $14\,^{\circ}$ AoA for $Re = 5 \cdot 10^5$, with $\frac{\mu_t}{\mu} = 0.1$

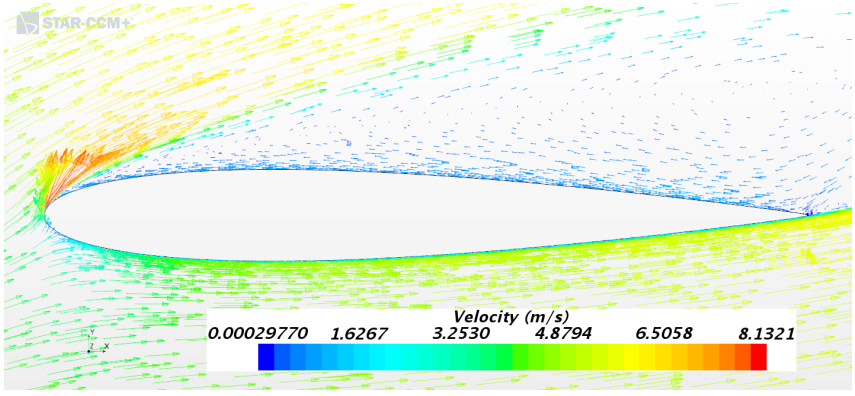

Figure 4.8: NACA0012 velocity vector scene at $14\,^{\circ}$ AoA for $Re = 5 \cdot 10^5$, with $\frac{\mu_t}{\mu} = 0.001$

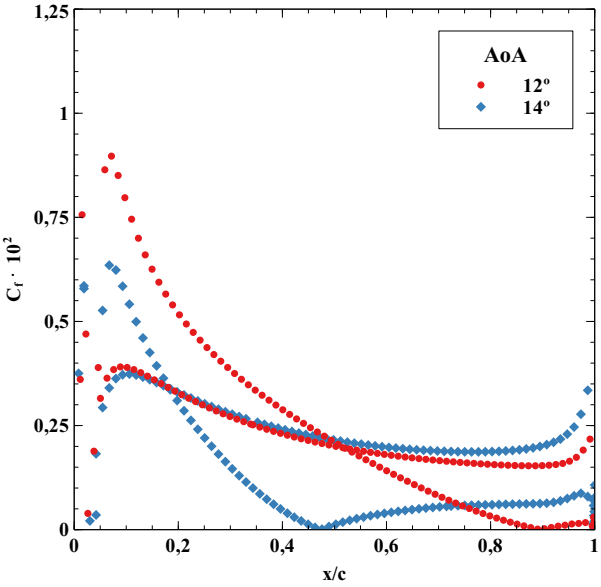

Figure 4.9: NACA0012 $|C_f|$ distribution between $12\ °$ and $14\ °$ AoA for $Re = 5 \cdot 10^5$ and $\frac{\mu_t}{\mu} = 0.1$ on the inlet

4.2.3 Reynolds Number Sensibility

In this section, to determine the boundary layer sensibility for different income velocities, a numerical analysis was performed to Reynolds numbers of $3.6 \cdot 10^5$, $5 \cdot 10^5$ and $7 \cdot 10^5$ for angles of attack of $6\ °$ and $12\ °$.

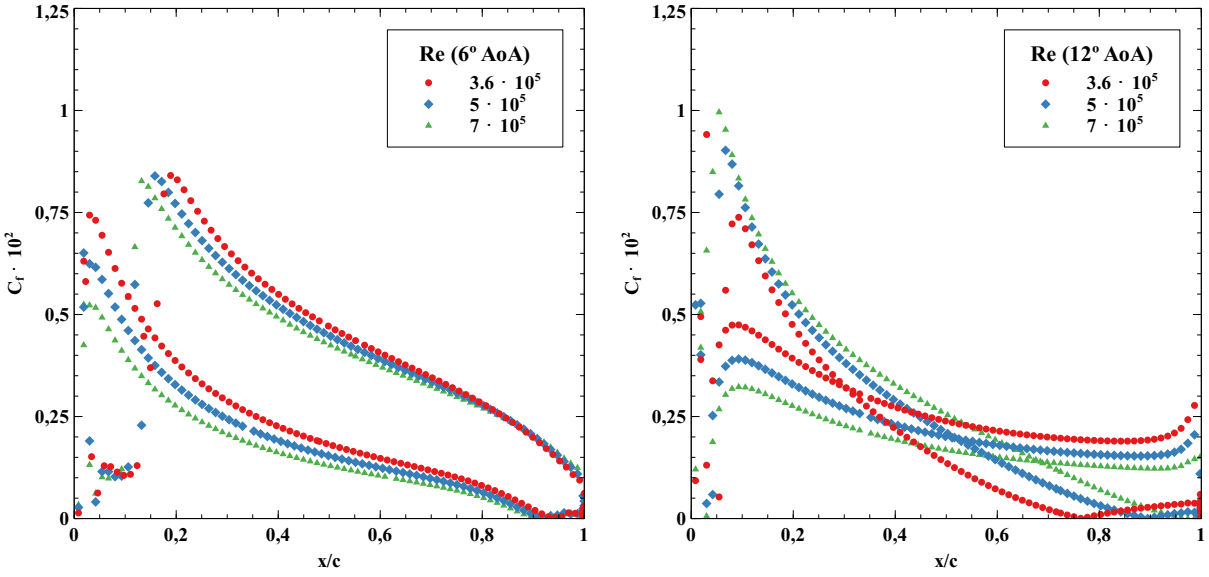

(a) Airfoil angle of attack of $6\ °$.

(b) Airfoil angle of attack of $12\ °$.

Figure 4.10: NACA0012 $|C_f|$ distribution for $6\ °$ and $12\ °$ AoA along the dimensionless chord for $Re = 3.6 \cdot 10^5, 5 \cdot 10^5, 7 \cdot 10^5$

In previous sections, the separation bubble was shown to be highly sensitive to the free-stream turbulence condition and pressure gradients. However, the momentum near the wall has an important

role in the flow transition after the laminar boundary layer separation. By increasing the income velocity, i.e. increase the Reynolds number, the momentum near the wall increases, forcing the transition of the separated flow. As a result, the separated flow reattaches sooner and the separation bubble shrinks, as illustrated on the skin friction coefficient plotted in figure 4.10.

Concerning the flow near the stall incidence, by increasing the momentum near the wall, the turbulent boundary layer will separate later, as shown in the skin friction coefficient plot in figure 4.10(b). Therefore, for higher Reynolds values, the airfoil is expected to reach higher angles of attack values until stall incidence.

4.3 Airfoil Aerodynamic Characteristics

The airfoil aerodynamic characteristics are mainly dependent on the Reynolds number, airfoil shape, angle of attack and free-stream turbulence. After some of the flow attributes have been presented, two different approaches will be outlined to approximate the numerical of the experimental results.

4.3.1 Steady Analysis

As already discussed in chapter 3, turbulence is characterized by the flow properties fluctuation, which forced us to average the calculation process of the NSE. Steady analysis, solve the RANS assuming that there is no time dependency on the problem $\left(\frac{\partial}{\partial t} = 0\right)$, therefore if the problem solution is steady, then convergence might be achieved.

For the physical conditions detailed in table 4.4, a steady analysis was performed until the moment when the convergence of the transport's residual partial differential equations becomes two orders of magnitude below the discretization error and the variables of interest stagnate or exhibit a negligible fluctuation.

	A, B, C	**D**	**E**
Boundary Condition	Velocity imposed	Pressure Imposed	No-slip
Physical Condition	$Re = 3.6 \cdot 10^5; 5 \cdot 10^5; 7 \cdot 10^5$ $\mu_t/\mu = 0.1$ $Tu = 1\%$ $\alpha = [0, 14]$	$P_{gauge} = 0$	$\tau_w \neq 0$

Table 4.4: Boundary and physical condition of the CFD analyses for the NACA0012, where Tu stands for turbulent intensity and the P_{gauge} is the pressure relative to atmospheric pressure. The letters A, B, C, D and E correspond to the boundary conditions in figure 4.1.

The problem at scope is expected to have a steady solution, even with the presence of a separation bubble. However, the separation bubble showed a highly unstable behaviour, not allowing the residuals and properties to stabilize. As a consequence, the solution convergence was only possible for a high under-relaxation of the solver. Additionally, for higher angles of attack values, the solution convergence was achieved by increasing the viscosity ratio at the inlet boundary to force the separated flow

reattachment, as depicted in table 4.5.

<table>
<tr><th>AoA (º)</th><th>$F_{Velocity}$</th><th>$F_{Pressure}$</th><th>$F_{\kappa-\omega}$</th><th>F_{μ_t}</th><th>$F_{\gamma-Re_\theta}$</th><th>$\frac{\mu_t}{\mu}$</th><th>Initial Guess</th></tr>
<tr><td>Default</td><td rowspan="3">0.7</td><td rowspan="2">0.3</td><td rowspan="3">0.8</td><td>1</td><td>0.8</td><td rowspan="3">0.1</td><td rowspan="3">None</td></tr>
<tr><td>0</td><td rowspan="2">0.6</td><td rowspan="2">0.2</td></tr>
<tr><td>2</td><td>0.1</td></tr>
<tr><td>5</td><td rowspan="4">0.2</td><td rowspan="4">0.01</td><td rowspan="4">0.1</td><td rowspan="4">0.1</td><td rowspan="4">0.1</td></tr>
<tr><td>6</td><td>10</td><td rowspan="3">Previous AoA</td></tr>
<tr><td>10</td><td>40</td></tr>
<tr><td>12,14,16</td><td>120</td></tr>
</table>

Table 4.5: Under-relaxation set-up and inlet changes for the NACA0012 steady simulation

Results

From the lift and drag coefficients plotted in figure 4.11 for lower angles of attack, $0\ ^\circ < \alpha < 5\ ^\circ$, the numerical results comply with the experimental results, which were taken from [4] and [5]. For these angles of attack values, from table 4.5, the convergence was achieved through an under-relaxation of the solver without managing the viscosity ratio values at the inlet. At some point, for angles of attack higher than $6\ ^\circ$, to reattach and stabilize the separation bubble to converge the numerical solution, the viscosity ratio value at the inlet was increased, as depicted in table 4.5. As a consequence, the free-stream flow induced a higher flow diffusion delaying the airfoil stall, thus contributing to an increase of the lift coefficient for higher angles of attack. From the drag coefficient plot for higher angles of attack values, as the flow remains attached to the airfoil for longer, the drag coefficient predicted by the RANS with the steady approach is lower than the experiment results.

Although the method used to converge a steady solution has shown to be reliable for lower angles of attack values, the procedure was highly time-consuming and non-reliable for higher angles of attack, thus simulations were performed just for $Re = 5 \cdot 10^5$. Nevertheless, the steady analysis proved that the inlet conditions have an important role in the solution convergence and on the airfoil properties and flow characteristics as well. As a conclusion, to determine the airfoil aerodynamic characteristics correctly at the studied Reynolds number values, the inlet turbulence conditions must be given.

4.3.2 Unsteady Analysis

By knowing that managing the inlet turbulence conditions is not a reliable technique to approximate the numerical solution with the experimental data, an unsteady analysis will be performed to obtain a steady time-averaged solution for Reynolds numbers of $3.6 \cdot 10^5$, $5 \cdot 10^5$ and $7 \cdot 10^5$. By solving the RANS equation 3.2 implicitly, the problem has now a physical solution over iterations, which the solution convergence depends upon a time-step establishment.

For the unsteady approach, the partial differential equations besides being discretized in space are also discretized in time. Just as the spatial discretization has a criterion to obtain a reliable solution, already covered in section 4.1.3, the time discretization also has a time-step stability criterion. Since

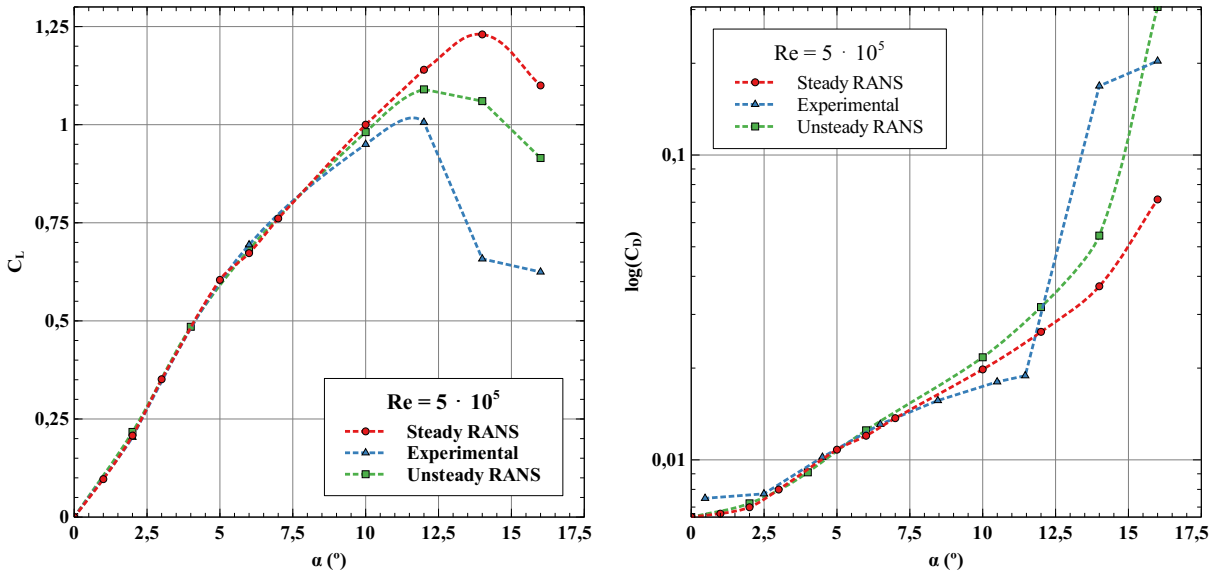

(a) (b)

Figure 4.11: NACA0012 lift and drag coefficient of experimental data and Simulation results at $Re = 5 \cdot 10^5$. (Experimental data were taken from [4] and [5]). The Steady RANS labelled on the plot stands for the steady approach to the RANS and Unsteady RANS stands for the unsteady approach to the RANS.

RANS equations were discretized implicitly, the solution convergence was achieved by managing the time-step and the number of iterations per each time-step until a residual decrease of two orders of magnitude below the discretization error. The physical conditions, for the unsteady approach, are the same presented in table 4.4, and the solution convergence was achieved using the program default relaxation factors of table 4.5. The results plotted in figures 4.11, 4.12 and 4.14 were determined for a time-step of $2.5 \cdot 10^{-}5$ and 20 to 30 iterations per time-step.

Results

The numerical solutions achieved a steady time-averaged solution without managing the inlet turbulence conditions. From the airfoil aerodynamic characteristics plotted in figure 4.11, although the numerical solutions continued to deviate from the experimental data for higher angles of attack, the airfoil stall predicted by the unsteady solver is closer to the experimental data. In addition, for lower angles of attack, the unsteady approach, similar to the steady one, comply with the experimental data.

For lower Reynolds numbers, the airfoil aerodynamic characteristics comply with the experimental data at lower angles of attack, although near stall incidence, the numerical results kept showing a slight deviation, as illustrated in figure 4.12.

For higher Reynolds numbers, the same properties behaviour was observed, although, for higher angles of attack, the implemented models had predicted a later stall, as illustrated in figure 4.13. To determine whether the turbulence levels could be influencing the delayed stall, the inlet viscosity ratio was decreased to values under 0.001. However, the stall angle of attack has never matched the experimental data.

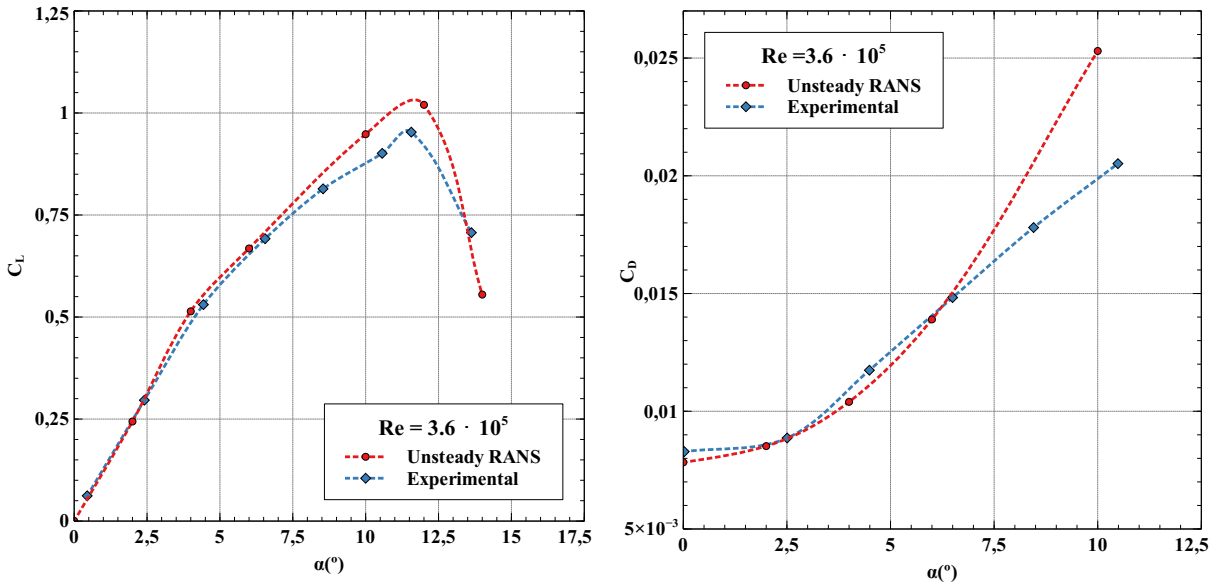

(a) (b)

Figure 4.12: NACA0012 lift and drag coefficient of experimental data and simulation results at $Re = 3.6 \cdot 10^5$. (Experimental data were taken from [4] and [5])

As a final remark, the absence of experimental and numerical uncertainties only allowed us to evaluate the numerical results qualitatively. Since near the stall incidence the aerodynamic characteristics deviated considerably from the experimental results, the following transient or three-dimensional analysis should avoid the study of angles of attack higher than $10\,^\circ$. Overall, for angles of attack under $10\,^\circ$ the numerical results will be considered close enough to experimental data and from now on will be assumed as appropriate to proceed for further simulations.

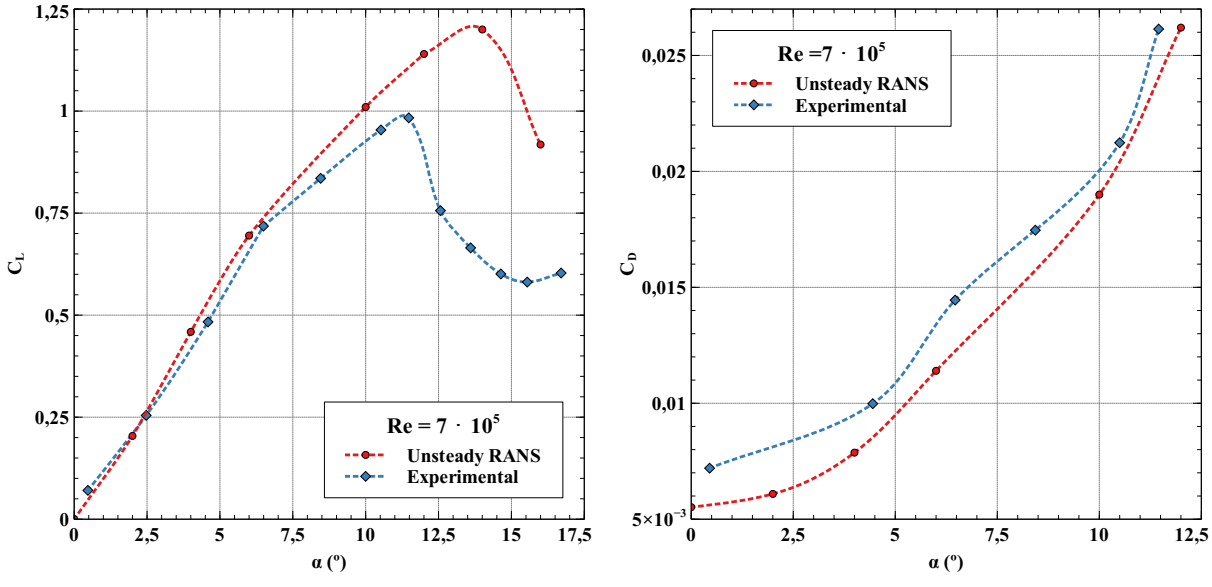

(a) (b)

Figure 4.13: NACA0012 lift and drag coefficient for experimental data and simulation results at $Re = 7 \cdot 10^5$. (Experimental data were taken from [4] and [5])

Stall Incidence Sensibility

Wind tunnels experiments are characterized by lower turbulence levels from the income flow in contrast to track conditions. From the lift coefficient plot in figure 4.14, for Reynolds numbers of $5 \cdot 10^5$, the experimental data showed a steeper lift decrease near the stall region in contrast to the numerical results.

To determine whether this phenomenon was a consequence of the inlet turbulence conditions, the same analyses were performed for two different viscosity ratios values. From the lift coefficients results plotted in figure 4.14, the compliance between numerical and experimental results improved with the decrease of the income flow viscosity ratio. The steeper lift decrease, due to the decrease of the income flow viscosity ratio, is an immediate consequence of the type of stall already discussed in section 4.2.2. In conclusion, the type of stall and the aerodynamic characteristics near the stall incidence are challenging to predict numerically. Not only due to the limitations of the mathematical models used, but also because the turbulence conditions during a lap on a circuit are difficult to predict.

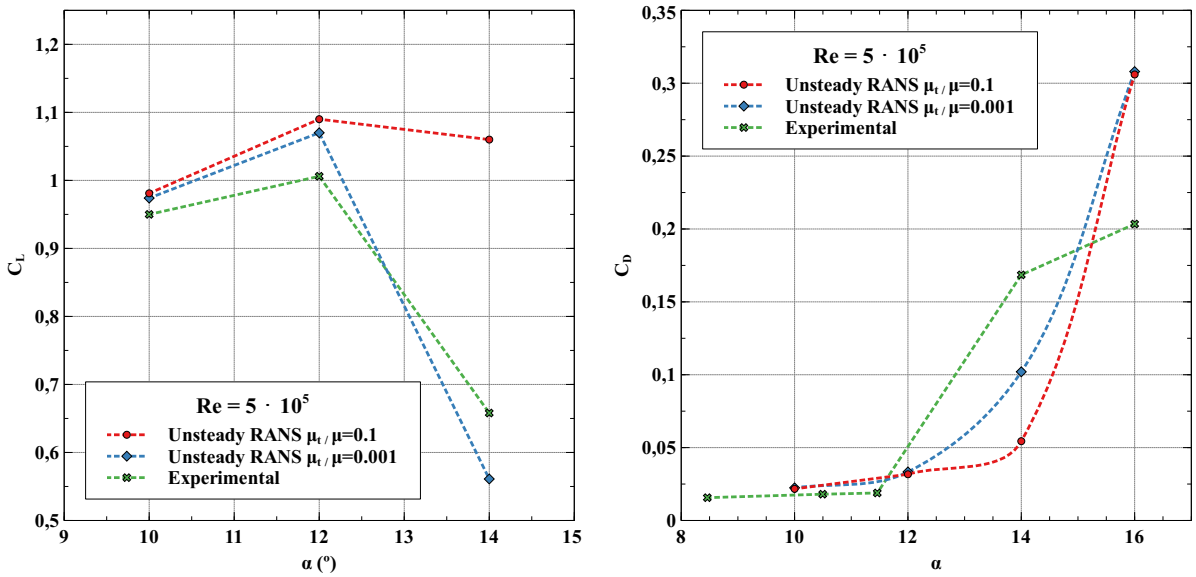

(a) (b)

Figure 4.14: NACA0012 lift and drag coefficient of experimental data and Simulation results at $Re = 5 \cdot 10^5$. (Experimental data were taken from [4] and [5])

4.4 Acceleration Analysis to NACA0012 (Case Study 1)

Chapter 2 enlightened the basic motorcycle dynamic principals and motorcycle behaviour during a race. From the velocity plot in figure 2.4, the rider was either accelerating or braking, which leads to a characteristic transient process along a circuit. It was already proven that the airfoil aerodynamic characteristics under constant velocities have a steady solution. In this section, the velocity magnitude will be forced to change at the inlet with the same acceleration and deceleration felt by the motorcycle. The objective was to analyse whether a dynamic analysis will lead to significant differences when compared to the

steady solution.

4.4.1 Physical Conditions

The analysis performed to the NACA0012 proved that the near stall region is highly sensitive to the inlet conditions. The airfoil stall is linked to flow instability, and from a practical point of view, for a motorcycle decelerating from $100m/s$ to $20m/s$, any instability is undesirable. To avoid being on the stall region when the motorcycle brakes, which corresponds to the maximum wing AoA, it will be stated that the wings AoA must be 20% away from the stall region, approximately $10\,^\circ$. Therefore, assuming that the AoA amplitude is $4\,^\circ$ from section 2.5, the simulation of acceleration and deceleration will be performed around $6\,^\circ$ and $10\,^\circ$ AoA, respectively.

The simulation set-up will be similar to that performed on unsteady analysis, section 4.3.2, except for the inlet velocity condition and the time-step. The time-step chosen for the unsteady analysis ensured the solution convergence at each time step during the transient process and the acceleration and deceleration are taken directly from the case study 1, section 2.4, respectively $acc = 6m/s^2$ and $acc = -10m/s^2$. Therefore the inlet velocity condition is given by a field function in Starccm+ defined by:

$$U(t) = V_i + \frac{dV}{dt} \times (t - t_i); (m/s) \tag{4.7}$$

where the V_i stands for the initial velocity, $\frac{dV}{dt}$ represents the acceleration or deceleration, t the simulation time and t_i the time of the already converged solution. The simulation proceed started with a constant speed V_i and at the time t_i has been introduced the function described in equation 4.7. After the airfoil has achieved its maximum velocity was introduced a constant velocity condition again.

4.4.2 Results

From the airfoil aerodynamic characteristics plotted in figure 4.15, during acceleration and deceleration the lift coefficient results lie within a quasi-steady approach with a maximum deviation no greater than 1%.

On the other hand, the drag coefficient slightly deviates from the steady solution, either for acceleration and deceleration. This deviation could be explained by the fluid inertia forces acting on the airfoil, from [6] and already discussed in section 2.4. During acceleration, the fluid inertia contributes negatively to the movement direction resulting in an overall increase in drag, compared to the steady-state condition. On the other hand, during deceleration, the fluid inertia contributes to the airfoil thrust, resulting in a drag reduction, which is supported by the numerical results in figure 4.15(b). Nonetheless, the differences between the steady and transient processes were at most 2%, thus concluding that the transient process does not affect the equilibrium of global forces. Furthermore, for these acceleration and deceleration magnitudes, the separation bubble did not show any sensibility neither in length nor positioning.

In conclusion, for the accelerations and decelerations magnitudes, the airfoil aerodynamic character-

istics can be predicted with a quasi-steady approach, thus concluding that the dynamic determination of the lift and drag coefficients are not important. From now on, in the present dissertation, the influence of acceleration on the wings will be discarded and the problem can be handled as consecutive steady problems.

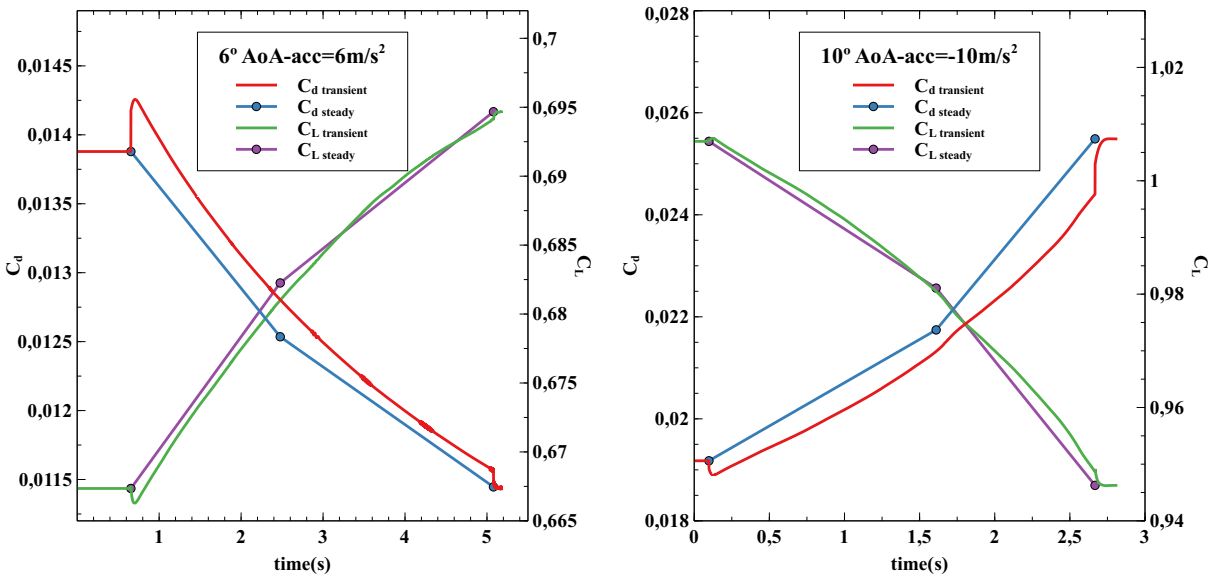

(a) Accelerating a NACA0012 at $6m/s^2$ at $6\,^\circ$ AoA

(b) Decelerating a NACA0012 at $10m/s^2$ at $10\,^\circ$ AoA

Figure 4.15: NACA0012 lift and drag coefficient for a dynamic velocity condition and a quasi-steady solution

4.5 Frequency Analysis to NACA0012 (Case Study 2)

The non-permanent inlet condition, according to the data results plotted in figure 2.8, is not only linked to the velocity magnitude. The velocity also changes under all three-dimensional vector properties. Neglecting the wing bounce motion and the roll motion during the motorcycle cornering, this section aims to verify whether the wing pitch introduces any instability on the airfoil aerodynamic characteristics, as already described in section 2.5. Again, the objective is to estimate whether the dynamic effects are relevant.

4.5.1 Physical Conditions

The simulation set-up will be similar to the one used in section 4.3.2, except for the inlet velocity condition and time-step establishment. Again, the time-step established in this unsteady analysis aims to ensure the solution convergence at each time step during the dynamic process.

In section 4.4, the angle of attack range during acceleration and deceleration motions was established. The simulation will be performed assuming a fixed income velocity magnitude with an average Reynolds of $Re = 5 \cdot 10^5$, and an angular variation of the inlet velocity with a frequency of $2\ Hz$ and an amplitude of $2\,^\circ$ about a mean angle of attack of $8\,^\circ$. The inlet velocity will be defined as a sinusoidal

function, as described below:

$$\alpha(t) = \alpha_{Mean} + \Delta\alpha \times sin(2\pi f(t - t_i - t_{phase})); (rad) \tag{4.8}$$

where α_{Mean} is the mean wing AoA, the $\Delta\alpha$ is the oscillation amplitude, f stands for the pitching frequency. The t_i stands for the time of the already converged solution and the t_{phase} is the phase correction of the sinusoidal function to start on the time t_i solution AoA. Similar to the simulation proceeds for the airfoil during acceleration, equation 4.8 is introduced as a field function in Starccm+ and after six complete cycles, a permanent condition with the initial angle of attack was forced.

4.5.2 Results

Firstly, neither the vortex shedding nor the dynamic stall were verified for the angular frequencies and AoA amplitudes determined in section 2.5. This result was already expected from [9] since both mechanisms take place at higher Strouhal numbers and angles of attack.

Similarly to the first case study, the lift coefficient lies within the steady solution for angles of attack of $6\ ^\circ$ and $10\ ^\circ$ with negligible deviations, as illustrated in figure 4.16. However, a deviation on the drag coefficient is observed. Once again, this deviation could be explained by the fluid inertia forces acting on the airfoil during the change of rotation direction. As an aside, the drag coefficient should be analysed carefully since the discretization errors, estimated in section 4.1.3, does not ensure the accuracy of the results. Nonetheless, for the dissertation goal, the deviation observed in the drag coefficient plot is not representative. Thereby, it will be assumed that the pitching motion does not influence the airfoil aerodynamic characteristics. After performing both dynamic analyses, a quasi-steady approach is sufficient to proceed with further analyses.

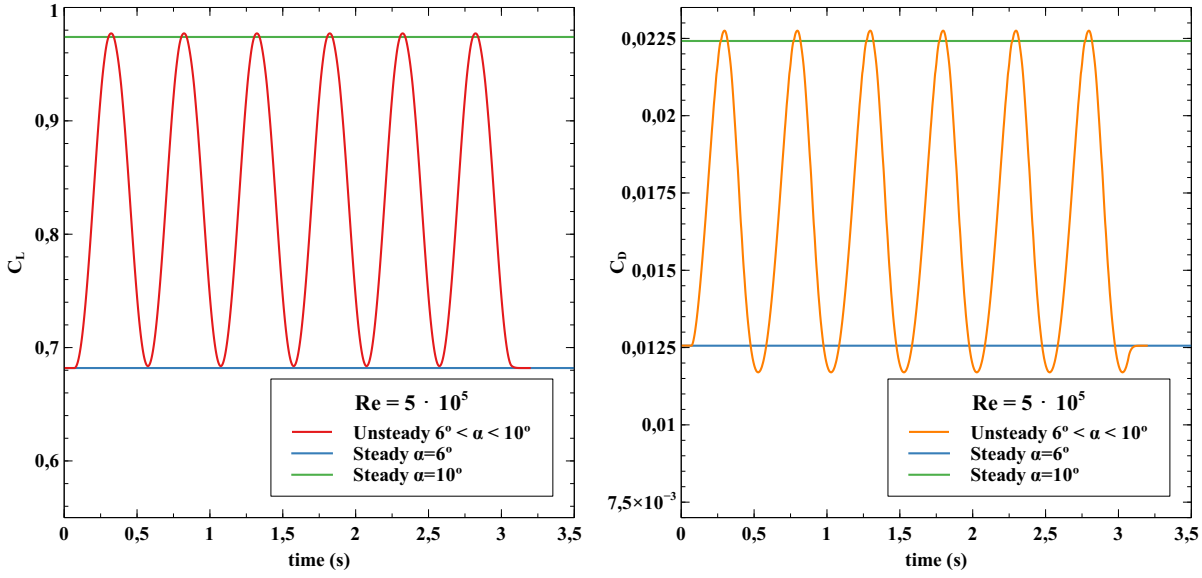

(a) (b)

Figure 4.16: NACA0012 lift and drag coefficient for a transient angular frequency condition and a steady-state solutions for $Re = 5 \cdot 10^5$

Chapter 5

3D-RANS NACA23015

From the two-dimensional results, the amount of lift that a wing produces is dependent on the shape, income velocity and income flow conditions. However, when it comes to the three-dimensional analysis, there is an additional effect concerning lift. Near the wing-tip, the air is free to move from the pressure side to the suction one. As a result, a tip-vortex is formed interfering with the streamwise flow.

This vortex effect over the wing is negligible as long as the ratio between the wing-span and the wing-chord lengths (aspect ratio $\mathcal{AR}$) is large enough. Since the MotoGP regulation constrains the maximum wing-span, these wings end-up with low $\mathcal{AR}$ and highly prone to the three-dimensional effects. In short, the main concern through this chapter is to measure the influence of the three-dimensional effects over low $\mathcal{AR}$ wings.

5.1 NACA23015 2D

Chapter 4 reflects upon the properties of a symmetric airfoil NACA0012. However, based on the lift force demands studied in section 2.2.3, a symmetric foil falls outside the scope of a high-performance lift surface. Similarly to [12], in this chapter, a three-dimensional study will be performed around a NACA23015 illustrated in figure 5.1. In the present section, a two-dimensional analysis will be performed to NACA23015, serving as a reference for the finite wing results.

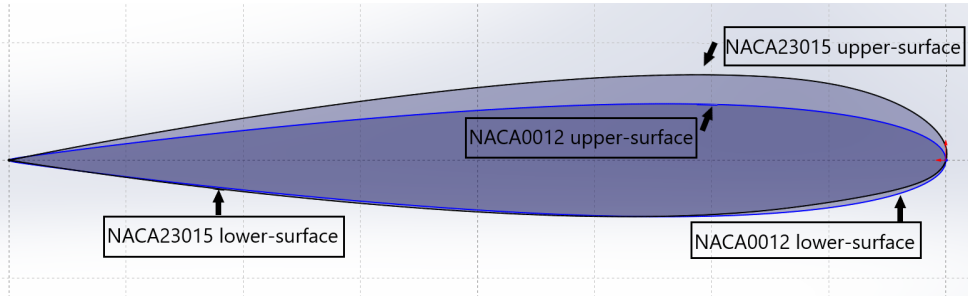

Figure 5.1: NACA23015 and NACA0012 sections sketch

5.1.1 Simulation General Settings

The two-dimensional analysis was performed around a Multi-block, quadrilateral C-mesh with the same characteristics described in section 4.1 and the same simulation settings of the unsteady analysis in section 4.3.2. For the sake of comparison, the NACA23015 will be analysed for the AoA already studied in section 4.5 and for the lowest Reynolds number. The chosen Reynolds, $Re = 3.6 \cdot 10^5$, shows a region with large separation bubbles, which requires greater concern, being also a case study for wings with smaller chords racing in MotoGP.

5.1.2 Numerical Results

The NACA23015 properties depicted in figure 5.2 comply with the expected results for a cambered and thicker airfoil, with more than 20% increase in the lift for the entire AoA range, as well as an increase in drag. However, for higher AoA, the NACA0012 suddenly increases the drag coefficient above the cambered airfoil.

Concerning transition, the separation bubble on the cambered airfoil suction side is occurring much sooner than on the symmetric foil, as illustrated in figure 5.3 for the NACA23015, and 4.4 and 4.5 for the NACA0012. The separation bubble misalignment is a consequence of the higher adverse pressure gradient induced by the NACA23015 steeper upper surface slope, as illustrated in figure 5.1. In addition, the stronger pressure gradient leads to an early turbulent separation flow for higher AoA.

On the pressure side, since the NACA23015 curvature is similar to the NACA0012, the laminar separations and separation bubbles are in identical locations.

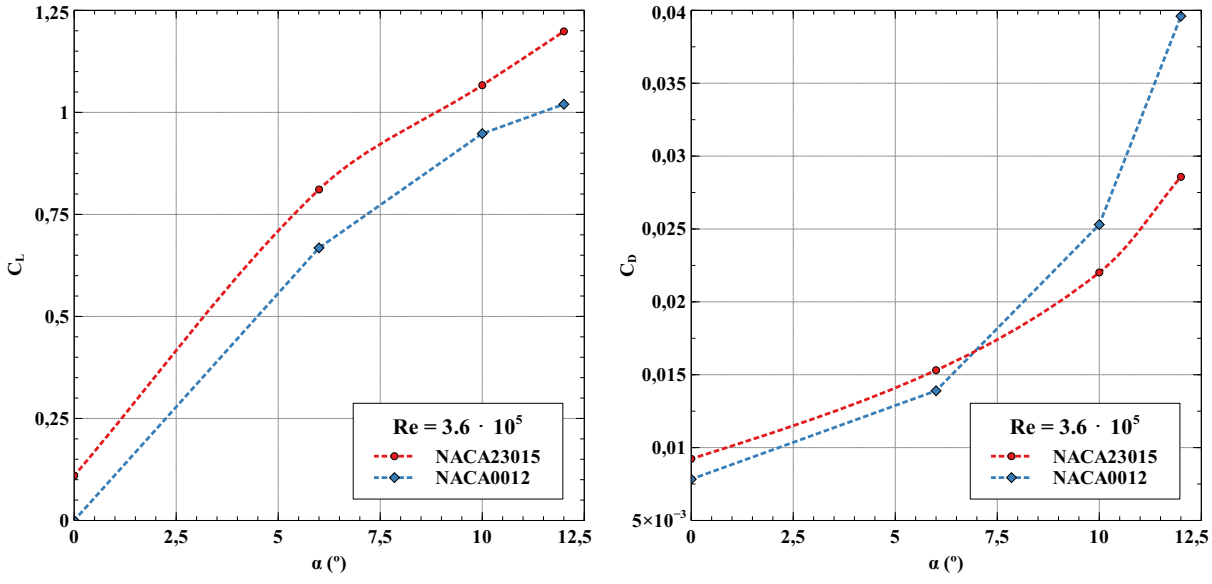

(a) (b)

Figure 5.2: NACA0012 and NACA23015 lift and drag coefficient for $Re = 3.6 \cdot 10^5$

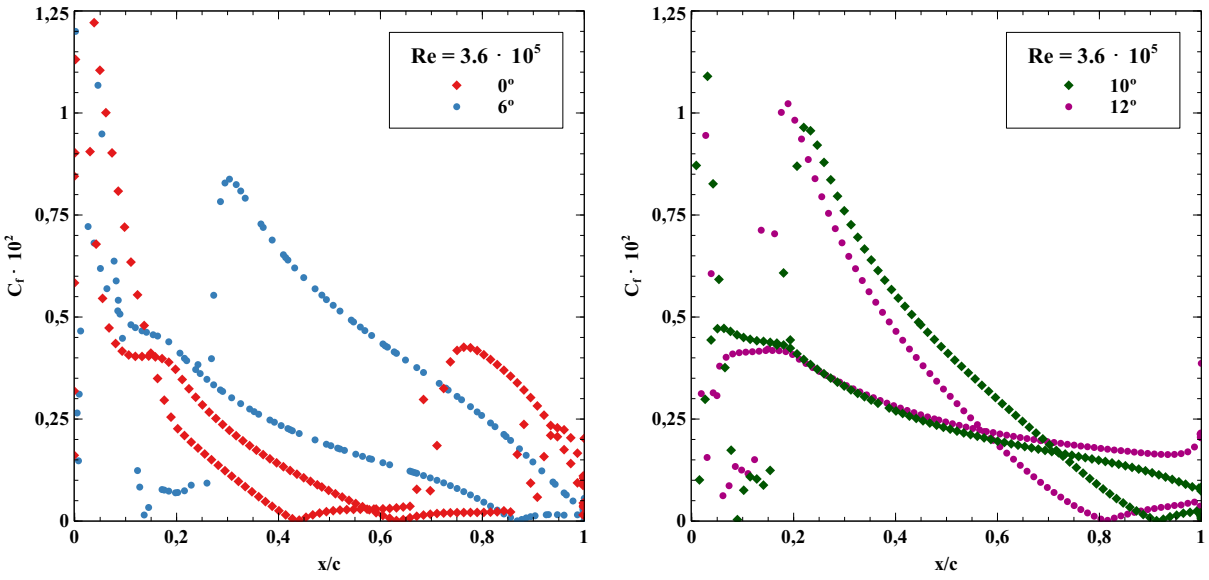

(a) (b)

Figure 5.3: NACA23015 $|C_f|$ distribution along the airfoil at $Re = 3.6 \cdot 10^5$ for different AoA

5.2 3D-Grid

The structured grids developed on the two-dimensional simulations provided a higher degree of quality elements and higher control over the mesh. In addition, the hexaedron elements are typically built to be aligned with the flow direction leading to more accurate results and better convergence. However, it requires powerful machines when it comes to three-dimensional analysis. As a consequence, the grid choice ends-up in a trade-off between accuracy, available computational power and time. The lack of powerful machines led us to choose the unstructured polyhedral grids. These grids, given their considerable good solution accuracy with a low computation power cost, are widely used nowadays for several applications.

In the present section, the fundamental characteristics of the three-dimensional grid will be outlined for the three wings configurations: a wing without an end-plate, another one with an end-plate and a box-wing.

5.2.1 2D- Polyhedral Grid

To avoid yielding with inaccurate results, the aerodynamic characteristics will be determined on a cross-wise plane of the three-dimensional grid, as illustrated in figure 5.4. In this section, the differences between the structured and unstructured grid will be enlightened.

The unstructured mesh is divided between polyhedral elements all over the fluid domain and a prismatic layer on the near-wall region, illustrated in figure 5.4(b). This prismatic layer follows the same characteristics as the structured grid discussed in sections 3.2 and 4.1. The lack of computational power to perform the three-dimensional analysis, force us to decrease the total number of elements with the cost of less accurate results. As a result, the two-dimensional unstructured grid ended up with ap-

proximately thirty thousand elements, 70% lower than the structured grid. To qualitatively measure the

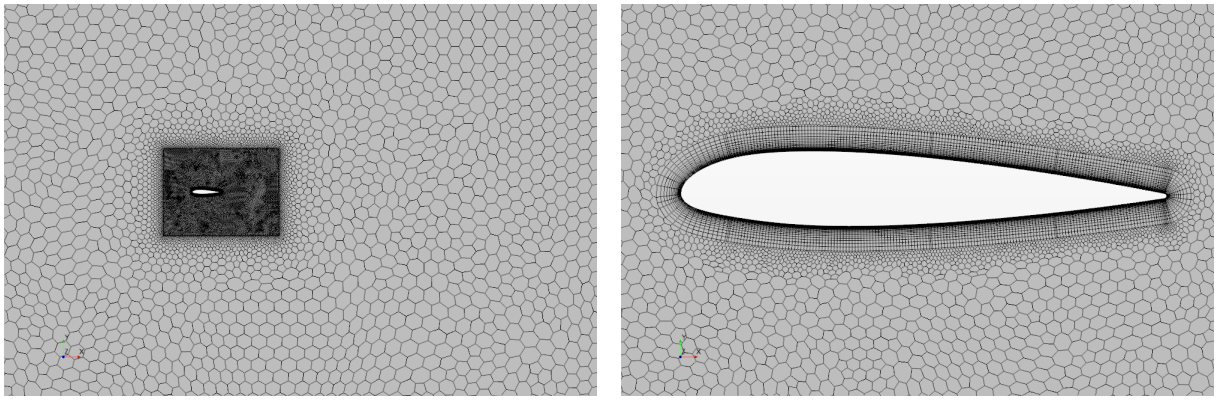

(a) Two-dimensional unstructured polyhedral grid

(b) Two-dimensional unstructured polyhedral grid near the airfoil

Figure 5.4: Two-dimensional unstructured polyhedral grid around NACA23015

consequences of changing the grid type and reducing the total number of elements, the NACA23015 properties, for both unstructured and structured grids, are plotted in figure 5.5.

The substantial decreasing number of elements leads to a high deviation of the drag coefficient results, although for the lift coefficient, the solution remained identical with negligible deviation. Besides the prismatic layer near the airfoil remained identical to the structured grid, the deviation observed on the drag coefficient is a consequence of a poor prediction of the friction drag forces. Since the three-dimensional analysis aimed to evaluate especially the lift properties of the finite wing, these deviations were considered good enough to proceed with the three-dimensional analysis.

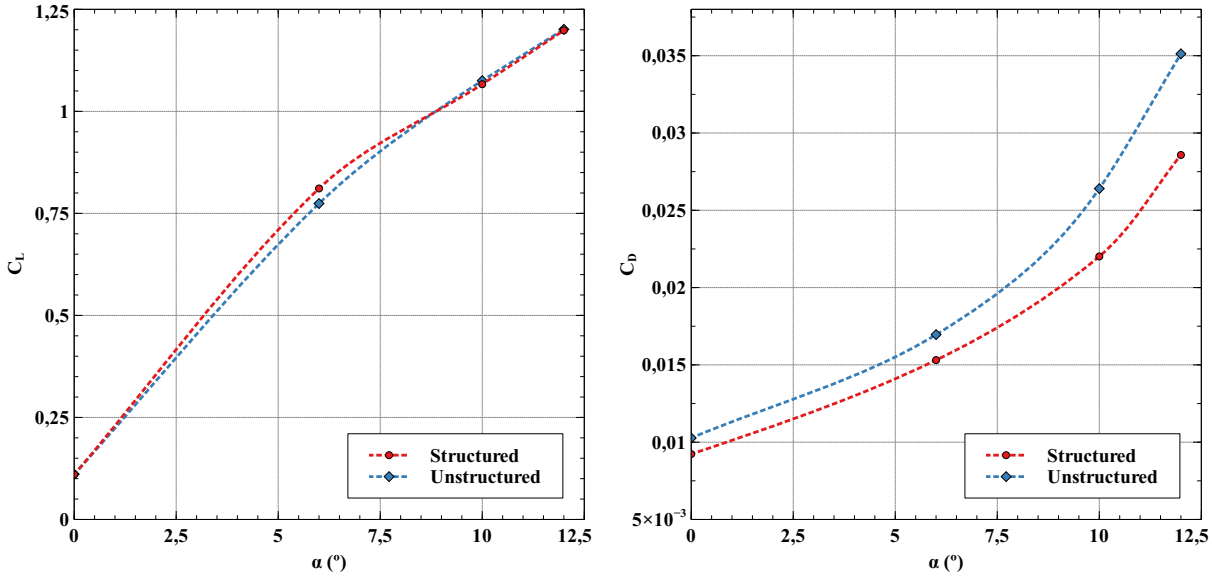

(a)

(b)

Figure 5.5: NACA23015 C_l and C_d for the structured and unstructured grids at $Re = 3.6 \cdot 10^5$

5.2.2 3D - Polyhedral Grid

In the previous studies, the control volumes were confined to the two-dimensional plane. For the three-dimensional analysis, the same grid has to be defined in space. For this reason, three-dimensional grids near the wall region should be handled with special attention. In figure 5.6(b), a cut plane of the 3D-grid is illustrated where the prismatic layer around the airfoil can be observed. The established settings for this layer are identical to the ones used in sections 3.2 and 4.1.

To approximate three-dimensional analysis to the reality, the wing was attached to a wall, simulating the motorcycle fairing, as illustrated by the letter (A) in figure 5.6(a). In table 5.1 are the general mesh settings for all the different finite wings set-ups. The sizing settings regarding the inlet and fluid domain correspond to the grid base size set to $0.1m$. Additionally, in table 5.2 is depicted the total number of elements for the three wing configurations analysed in this chapter that follow the same grid characteristics depicted in table 5.1.

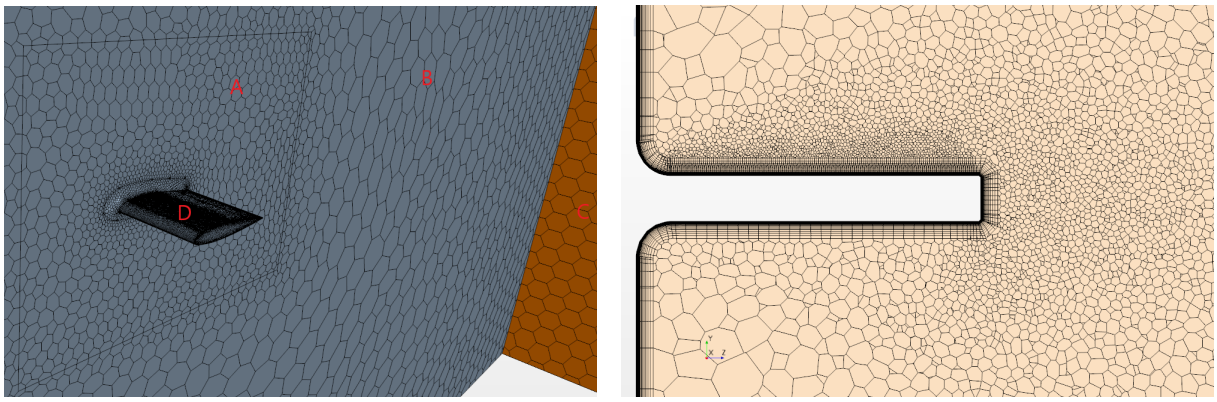

(a) Isometric view over the surface mesh of the three-dimensional grid

(b) Front view over a crosswise cut plane over the three-dimensional grid

Figure 5.6: Finite-wing three-dimensional grid

	A	B	C	D
Boundary Condition	No-slip	Free-slip	Pressure Imposed	No-slip
Physical Condition	$\tau_w \neq 0$	$\tau_w = 0$	$P_{Gauge} = 0$	$\tau_w \neq 0$
Cells Sizing*	25%	100%	100%	1%

Table 5.1: Settings of the three-dimensional unstructured grid for a finite-wing NACA23015. *The cells sizing for each boundary is relative to the base size of 0.1m.

	Finite-wing	Finite-wing with end-plate	Closed-wing
Number of cells	2,018,134	2,643,891	4,587,154

Table 5.2: Total number of elements of the three-dimensional grid for the three different wing configurations

5.3 Finite-Wing Analysis

As a first approach to the finite-wing analysis, the properties of a wing without end-plate and with symmetry condition on the wing-root will be outlined, illustrated in figure 5.7. This way, the influences of the tip-vortex over the wing properties can be isolated. In section 5.3.1, the properties of a finite wing will be estimated under a perfect fluid assumption, the lifting-line-theory, and afterwards under a numerical analysis considering real fluid flow conditions.

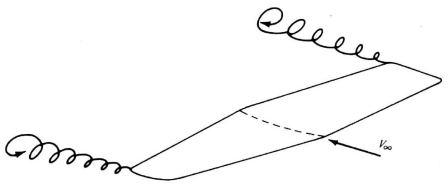

Figure 5.7: Schematic of a finite-wing prone to tip-vortex, [10]

5.3.1 Lifting Line Theory

The lifting line theory is a useful tool to predict the properties of high AR wings. However, since the present analysis regards a low aspect ratio wing, this theory is a qualitative assessment of the CFD results.

The lifting line theory states that a wing producing downforce is exposed to a vortex spreading mechanism that is responsible for the upwash effect, from [10]. This mechanism leads to a pressure loss acting on the wing surface, decreasing the downforce and inducing an additional drag force.

Assuming an elliptical circulation distribution over a wing without twist and sweep, the lift coefficient of a finite-wing is given by equation 5.1, [10].

$$C_L = \frac{C_l}{1 + \frac{a_{2d}}{\pi \mathit{AR}}} \tag{5.1}$$

Where C_l is the airfoil lift-coefficient, a_{2d} is the C_l growth rate and AR the aspect ratio. Assuming that the C_l grows linearly between 0º and 6º AoA, the a_{2d} is taken directly from the unstructured grid C_l solution plotted in figure 5.5.

Additionally, the tip vortex induces an upward velocity field to the income velocity. Due to this upwash velocity, the effective velocity is now assigned to an induced AoA. Assuming elliptic circulation distribution the induced AoA is described in equation 5.2.

$$\alpha_i = \frac{C_L}{\pi \mathit{AR}} \tag{5.2}$$

This induced AoA is responsible for the emergence of an induced drag force, thus the total drag assigned to the finite wing is described in equation 5.3.

$$C_D = C_{Dairfoil} + C_{Di} \; ; \; C_{Di} = \frac{C_L^2}{\pi \mathit{AR}} \tag{5.3}$$

Where C_{Di} is the induced drag.

Finally, the correspondent properties are described in the table of figure 5.8 for a finite wing at 6º AoA and $Re = 3.6 \cdot 10^5$ with an $\mathcal{AR}= 2$. These properties are valid as long as the wing remains at AoA smaller than 6º, i.e. on the C_l linear zone.

From the obtained results, the $\mathcal{AR}$ has a significant role over the global finite wing properties. From the table observed in figure 5.8, the pressure loss on the wing-tips represents a 49% lift coefficient decrease and a 153% drag coefficient increase about the airfoil aerodynamic characteristics. The global drag force increase is a direct result of the upwash velocity intensity that increased the induced angle of attack significantly.

From the lift and induced drag coefficient plots in figure 5.8, the $\mathcal{AR}$ of this finite-wings range a very low-efficient region according to the maximum induced drag and the reduced lift force. Since the MotoGP wings are limited by regulation to a maximum span, the only solution to avoid such higher interference of the tip vortex is to decrease the wing chord. As a result, lower chords will decrease the Reynolds numbers and the wing will produce less downforce. Overall, the final decision between a high and low aspect ratio wing is a trade-off between the $\mathcal{AR}$ and Reynolds weight over the wing properties.

It must not be forgotten that the lifting line theory is a simple approximation of the real fluid flow condition. It assumes a rigid wake aligned with the income flow and a direct relation between lift and the circulation, which is only valid for an ideal fluid. Nonetheless, the results depicted should not deviate from the real fluid flow solution as long as the crosswise velocities coming from the wing tip do not disturb the free-stream flow.

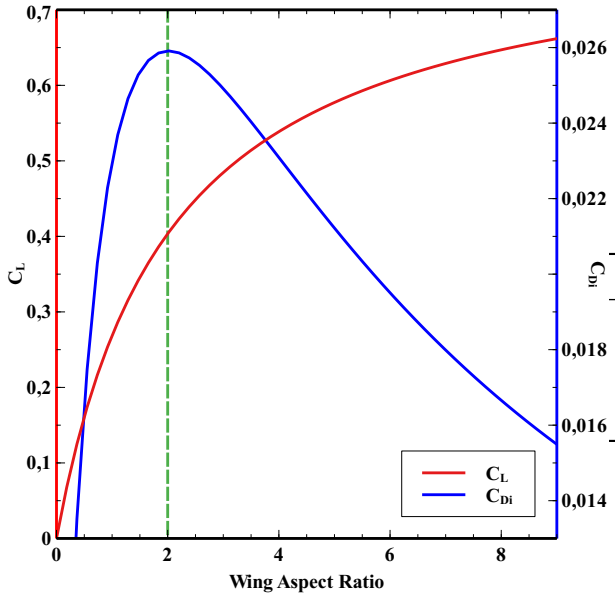

NACA23015 at 6º and $Re = 3.6 \cdot 10^5$					
	a_{2d} $[rad^{-1}]$	C_L	C_D	C_{Di}	α_i [º]
Airfoil	6.33	0.81	0.017	-	-
Wing ($\mathcal{AR}= 2$)	-	0.40	0.043	0.026	3.68

Figure 5.8: On the left side is plotted the C_L and C_{Di} function of the aspect ratio from the lifting line theory. The green line fits the MotoGP wings aspect ratio. On the right side are the results for the finite-wing at 6º and $Re = 3.6 \cdot 10^5$ predicted by the lifting line theory.

5.3.2 Wing Without End-Plate in Symmetry Conditions

The lifting line theory has predicted the aerodynamic characteristics of a finite-wing, under the assumption of a perfect fluid. Throughout this dissertation has been discussed the importance of the viscous effects on the flow characteristics. As a result, the three-dimensional effects in viscous flow may change the finite-wing aerodynamic characteristics.

Over the three-dimensional grid discussed in section 5.2, the NACA23015 will be studied with the same simulation settings performed on the unsteady analysis in section 4.3.2. The finite-wing studied, in the present section, is a wing without end-plate, with symmetry condition on the wing-root, as illustrated in figure 5.7. Therefore, for the boundary condition A from table 5.1, the wall condition will be switched to a symmetric flow condition.

This section aims to discuss and visualize how the tip-vortex influences the flow over the wing surface and evaluate the results against the theoretical approximation of perfect fluid.

Either the separation bubble and the crosswise flow coming from the wing pressure side, are phenomena that change the streamwise velocity and consequently change the shear stress at the wall. One of the techniques proposed in [10] to illustrate these effects is the skin friction lines plot over the wing surfaces. These limiting flow lines illustrate the streamlines directions and the boundary layer separation and reattachment zones as well. From [10], near a separation or reattachment region, the skin friction lines are deflected 90°, as illustrated in figure 5.9. In addition, in three-dimensional flows, the boundary layer is not restricted to separate in the streamwise direction. Due to secondary flows, other different complex separations can emerge, such as saddle points, node points and spiral points, as illustrated in figure 5.10.

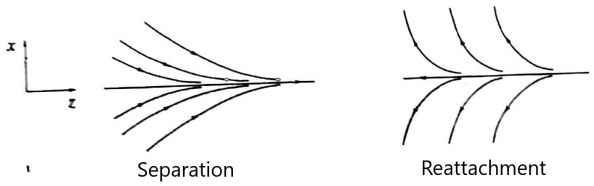

Figure 5.9: Limiting streamline configuration near a separation or reattachment line from [10]

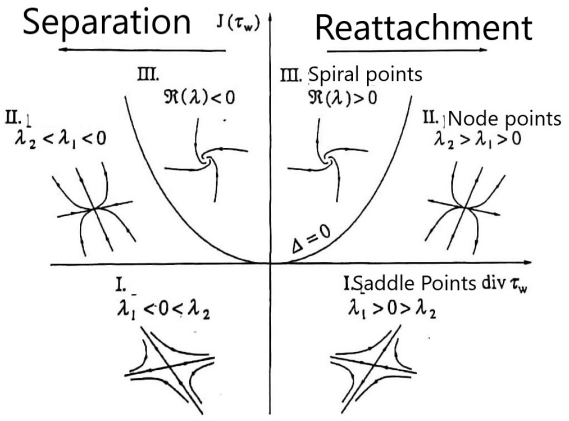

Figure 5.10: Limiting streamline configuration in critical points from [10]

From the skin friction lines plotted in figure 5.11 are illustrated different patterns representative of the already discussed separation and reattachment regions. Firstly, either on the wing pressure and suction side, a region similar to the 2D results is observed with a negligible deflection of the limiting flow lines. On the wing pressure side, this 2D region takes approximately 60% of the wing, as illustrated in figure 5.11(a). However, near the wing-tip, since the flow is free to move from the pressure to the suction side, the limiting flow lines exhibit a slight deviation to the crosswise direction in almost 40% of the wing.

On the wing suction side in figure 5.11(b), the same region similar to the 2D solution is observed, although the crosswise velocity interferes with approximately 40% of the wing-span. In this region, different three-dimensional separations phenomena can be observed due to secondary flows with spiral points reattachment and separation regions. These secondary flows are a consequence of the tip vortex effect illustrated in figure 5.13.

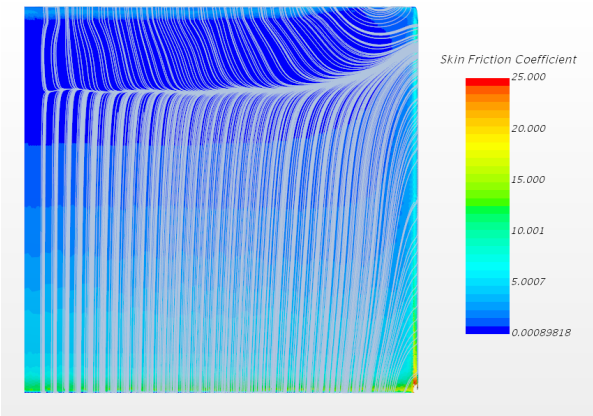

(a) Skin friction lines of the pressure side of the finite-wing with symmetry condition on the wing root for $Re = 3.6 \cdot 10^5$ and 6ºAoA

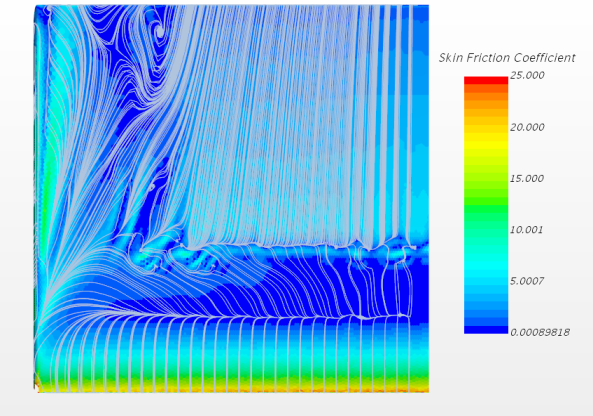

(b) Skin friction lines of the suction side of the finite-wing with symmetry condition on the wing root for $Re = 3.6 \cdot 10^5$ and 6ºAoA

Figure 5.11: Skin friction lines of the finite-wing with symmetry condition on the wing root for $Re = 3.6 \cdot 10^5$ and 6ºAoA

To determine the influence of the tip-vortex on the wing aerodynamic characteristics, the pressure coefficients for different wing sections are plotted in figure 5.12. By looking to the sections near the wing-tip at $0.16\ m$ and $0.18\ m$ from the wing-root, a sudden decrease of the pressure distribution is observed due to the high incidence of the crosswise velocities caused by the tip-vortex. As long as the wing sections get closer to the wing-root, the effect fades and the pressure distribution increases. From the velocity vectors of the secondary flow plotted in figure 5.13, the high incidence of the crosswise velocity can be observed over the wing-span as well as the upwash velocity responsible for the induced angle of attack.

In order to measure this induced angle of attack, the wing pressure and skin friction coefficient were plotted for a region not affected by crosswise velocity, on a section about $0.08\ m$ from the wing-root, and for the 2D results at the same angle of attack. From the friction coefficient plot in figure 5.14, the 2D and 3D separation bubbles are observed in different locations. This misalignment arises from the upwash effect, decreasing the finite-wing effective angle of attack. This phenomenon is also observed in the pressure coefficient plot, where the finite-wing shows a lower pressure distribution.

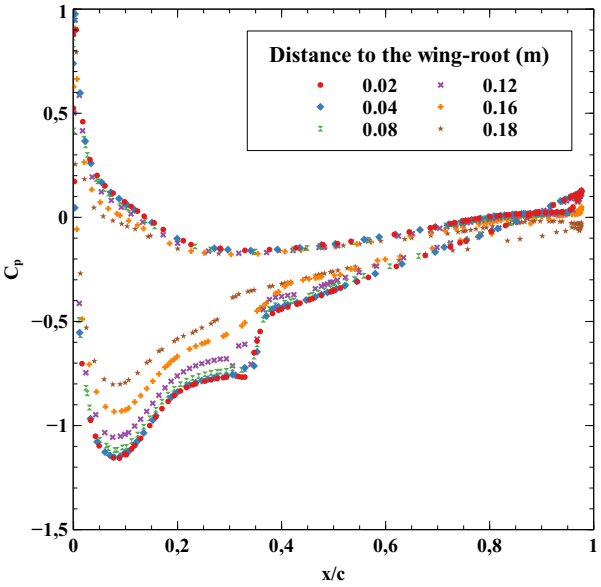

Figure 5.12: C_P distribution in different sections along the span in the crosswise direction for the finite-wing with symmetry condition on the wing root for $Re = 3.6 \cdot 10^5$ and 6ºAoA

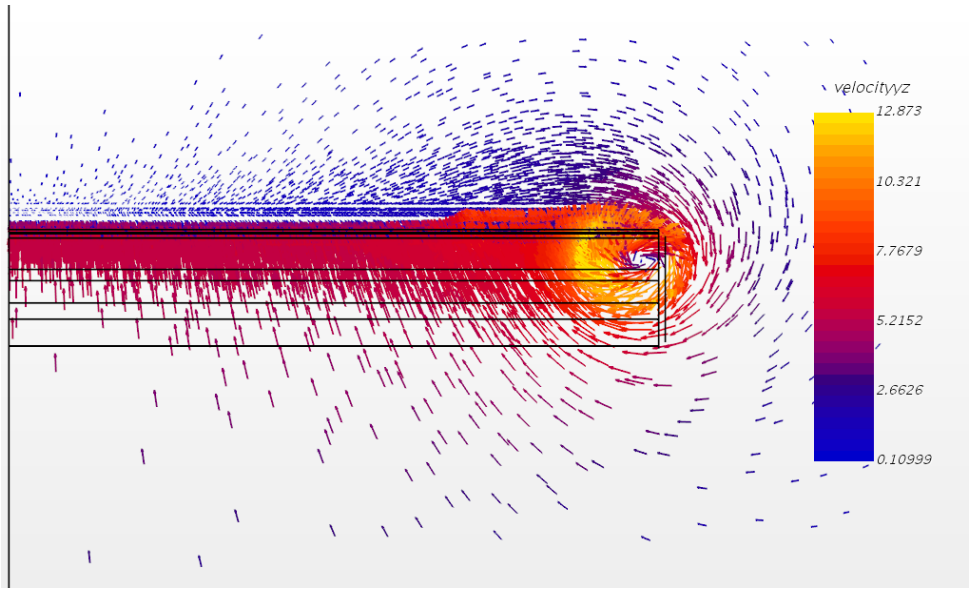

Figure 5.13: Velocity vectors at the trailing-edge for the finite-wing with symmetry condition on the wing root for $Re = 3.6 \cdot 10^5$ and 6ºAoA.

At the same graph is plotted the numerical solution of the airfoil at 3^o angle of attack that approximately fits the 3D pressure and skin friction coefficients. As a result, the induced angle of attack is approximately 3^o, resulting from the subtraction of the 3D angle of attack, or the geometric AoA, and the 2D angle of attack for the same pressure and skin friction distribution, or the effective AoA.

Finally, the lifting line theory predicted the wing aerodynamic characteristics close to the numerical results. The induced angle of attack predicted by the numerical results is similar to the one predicted by the lifting line theory. However, from the histogram plotted in figure 5.27, the lifting line theory overestimates the wing lift and drag coefficients. The difference is considerable but knowing that this theory is a

linear approximation of a non-linear problem, an acceptable approximation of the aerodynamic characteristics of a low $\mathcal{R}$ wing was achieved.

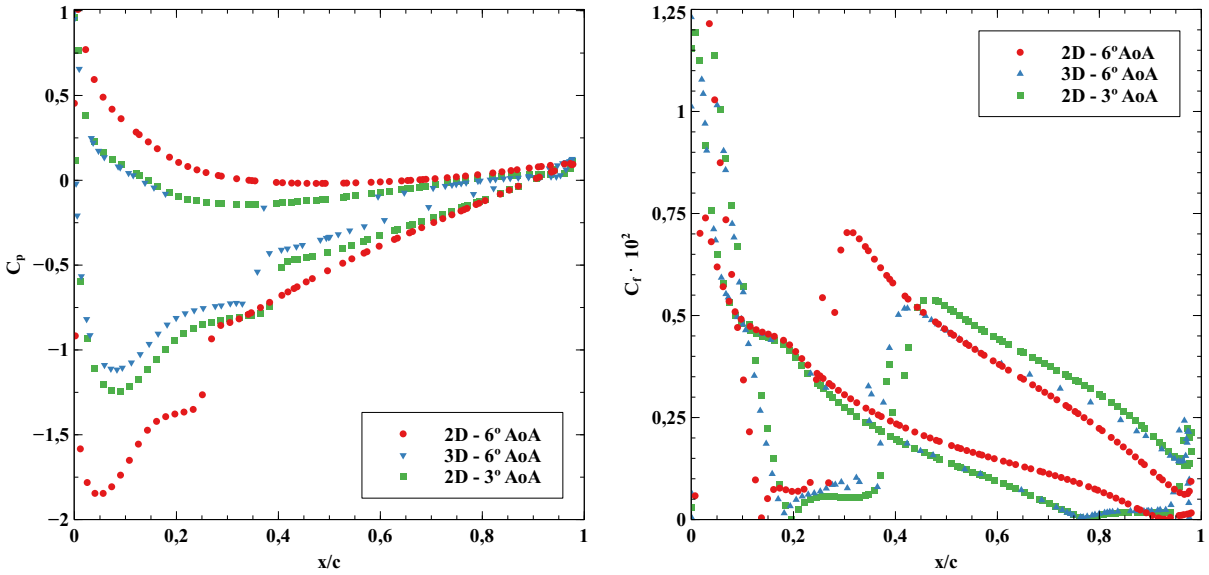

(a) C_P distribution for the NACA23015 airfoil and a section of the wing not affected by crosswise velocities at $Re = 3.6 \cdot 10^5$.

(b) $|C_f|$ distribution for the NACA23015 airfoil and a section of the wing not affected by crosswise velocities at $Re = 3.6 \cdot 10^5$.

Figure 5.14: C_p and C_f distribution for the NACA23015 airfoil and a section of the wing not affected by crosswise velocities at $Re = 3.6 \cdot 10^5$.

5.4 Wing-Body Junction

In the previous sections, a finite wing with symmetry conditions on the wing root was studied. In MotoGP prototypes, these wings are attached to the motorcycle fairing, bringing a new flow dynamics over the wings surface.

The wing-body junction is a relevant subject in aviation since it is responsible for secondary flows, such as horseshoe vortex and corner separations, that can affect the aircraft's performance, [30]. These secondary flows arise from the interaction between boundary layers developing through different planes in space, resulting in a three-dimensional boundary layer. In this section, the goal is to determine the influence of the wing-body junction on the main flow features discussed in the previous section. For this purpose, two different wing set-ups will be analysed: in section 5.4.1, a wing attached to a flat wall without end-plate at the wing-tip and afterwards in section 5.4.2, the same wing with end-plate at the wing-tip.

5.4.1 Wing Without End-Plate

From the skin friction lines plotted over the wing without end-plate on the pressure side, in figure 5.15, near the wing-root is visible not only a slight deviation of the limiting flow lines to the crosswise direction but also the emergence of small spiral points. This perturbation on the wing-wall junction takes approximately 5% of the wing-span. These effects are a consequence of the horseshoe vortex also illustrated

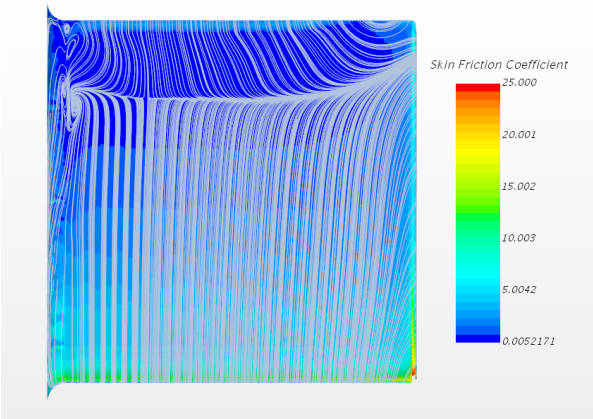

(a) Skin friction lines of the pressure side of the finite-wing with a no-slip condition on the wing root for $Re = 3.6 \cdot 10^5$ and 6ºAoA

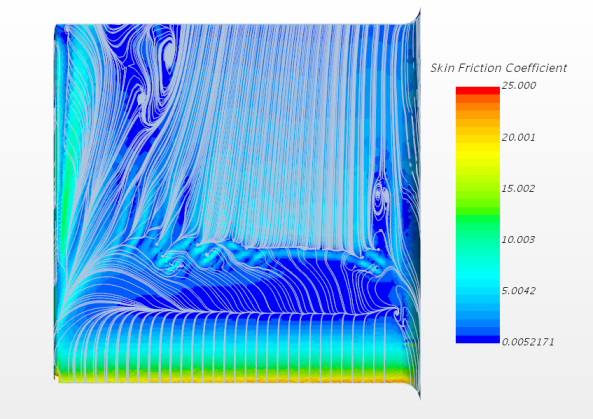

(b) Skin friction lines of the suction side of the finite-wing with a no-slip condition on the wing root for $Re = 3.6 \cdot 10^5$ and 6ºAoA

Figure 5.15: Skin friction lines of the finite-wing with a no-slip condition on the wing root for $Re = 3.6 \cdot 10^5$ and 6ºAoA

over the velocity isolines of the secondary flow in figure 5.16. In addition, the tip-vortex effects over the streamwise flow are identical to those observed in the wing with symmetry conditions, as illustrated in figure 5.13.

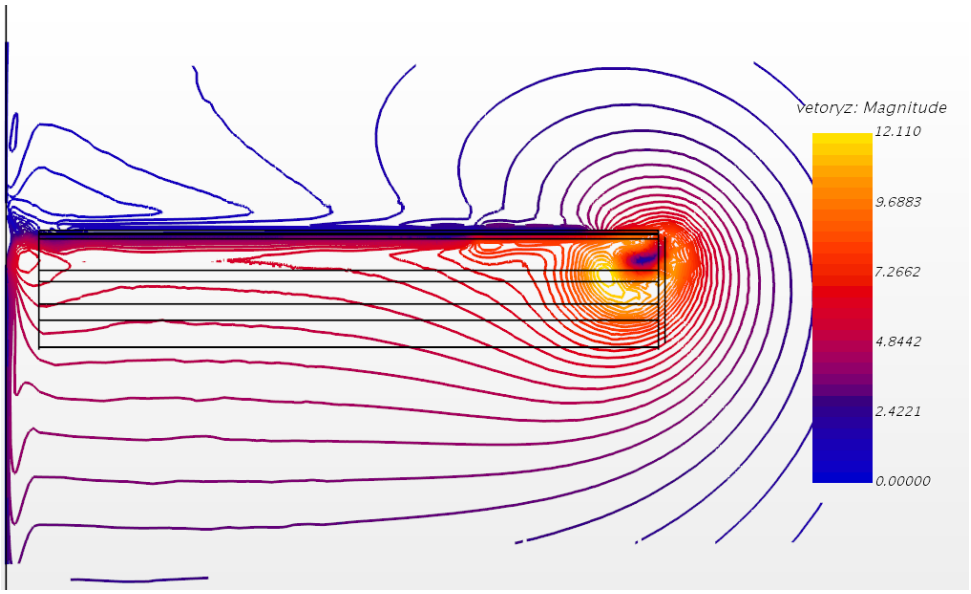

Figure 5.16: Velocity isolines at the trailing-edge for the finite-wing with a no-slip condition on the wing root for $Re = 3.6 \cdot 10^5$ and 6ºAoA

5.4.2 Wing With End-Plate

At the wing illustrated in figure 5.6, an end-plate was attached on the wing-tip with an offset of $20\ mm$ and $2.5\ mm$ in thickness.

As expected, the same behaviour of the limiting flow lines is observed near the wing-root, as illustrated in figure 5.17. One the other hand, the end-plate considerably changed the flow near the wing-tip, in contrast to the wing without end-plate. The main goal of attaching an end-plate at the tip is to decrease

the influence of crosswise velocities over the streamwise flow. As a result, the pressure loss near the tip is reduced. This effect is illustrated in figure 5.19, where the crosswise velocities on the pressure are less intense than for the wing without end-plate already presented in figure 5.13.

On the other hand, at the suction side near the end-plate, the interaction between the tip-vortex and the secondary flows has a massive impact over the streamwise flow, as illustrated in figure 5.18. This secondary flows are responsible for disturbing more than 30% of the streamwise flow over the wing-span.

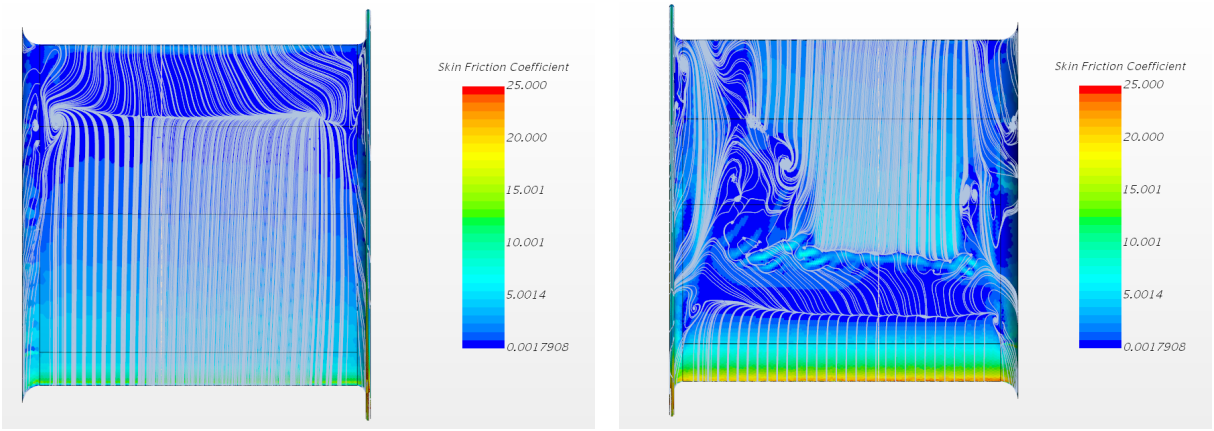

(a) Skin friction lines of the pressure side of the finite wing with an end-plate at the tip for $Re = 3.6 \cdot 10^5$ and 6°AoA

(b) Skin friction lines of the suction side of the finite wing with an end-plate at the tip for $Re = 3.6 \cdot 10^5$ and 6°AoA

Figure 5.17: Skin friction lines of the finite wing with an end-plate at the tip for $Re = 3.6 \cdot 10^5$ and 6°AoA

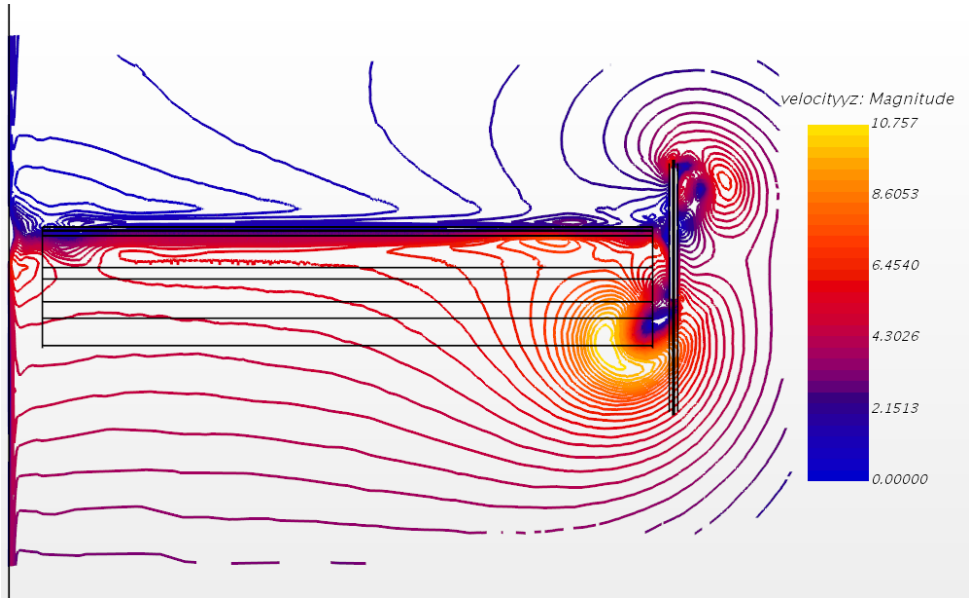

Figure 5.18: Velocity isolines at the trailing-edge for the finite-wing with a no-slip condition on the wing root and an end-plate attached at the wing tip for $Re = 3.6 \cdot 10^5$ and 6°AoA

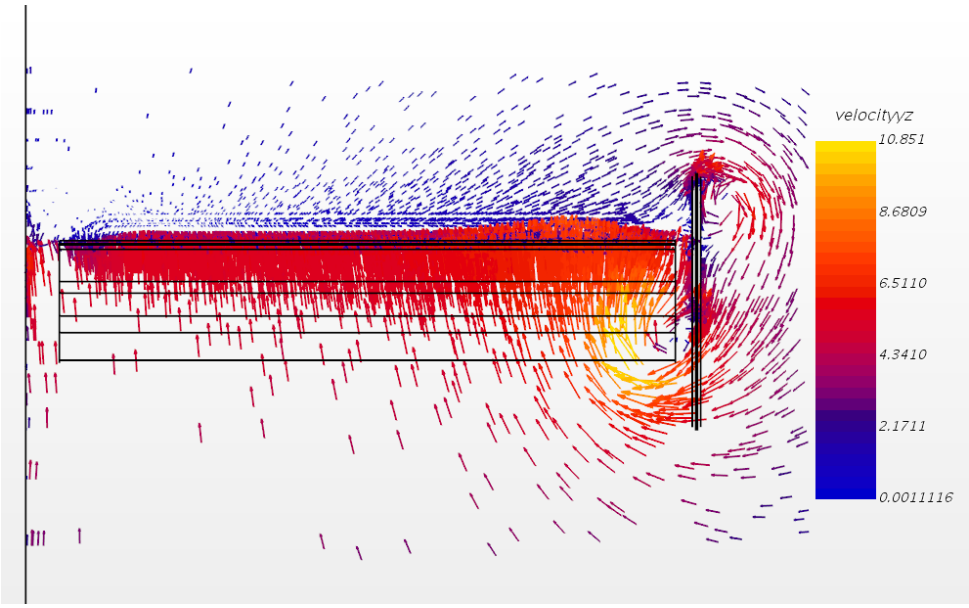

Figure 5.19: Velocity vectors at the trailing-edge for the finite-wing with a no-slip condition on the wing root and an end-plate attached at the wing tip for $Re = 3.6 \cdot 10^5$ and 6°AoA

5.4.3 Results Discussion

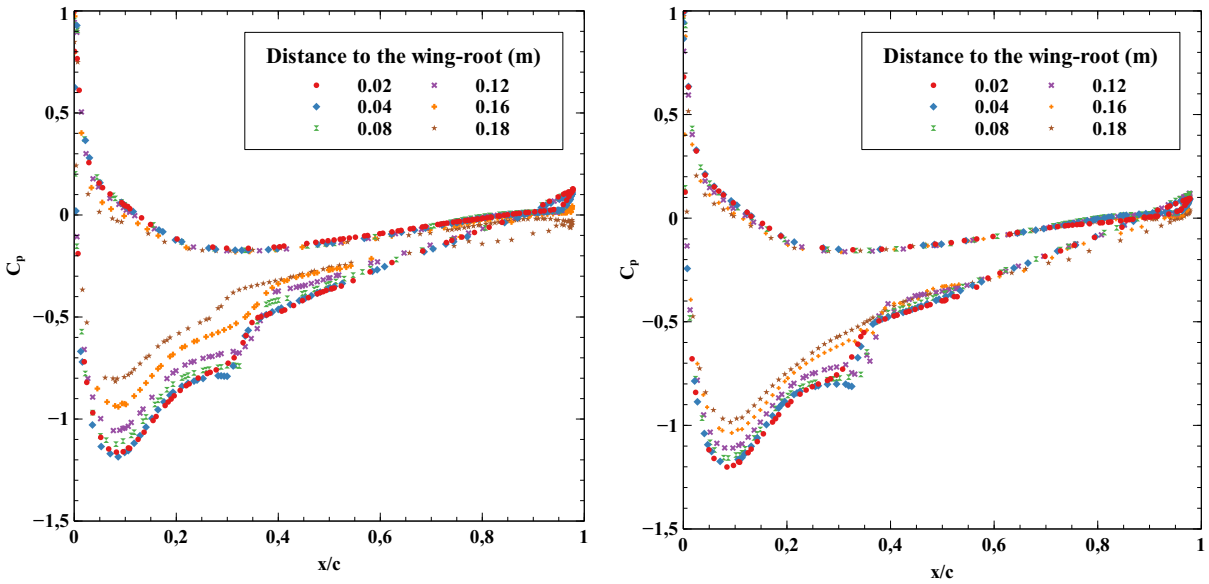

(a) C_P distribution in different sections along the span in the crosswise direction for the finite-wing without an end-plate and with a no-slip condition on the wing root at $Re = 3.6 \cdot 10^5$ and 6°AoA

(b) C_P distribution in different sections along the span in the crosswise direction for the wing with an end-plate and a no-slip condition on the wing root at $Re = 3.6 \cdot 10^5$ and 6°AoA

Figure 5.20: C_P distribution in different sections along the span in the crosswise direction for the finite-wing with and without an end-plate at $Re = 3.6 \cdot 10^5$ and 6°AoA.

To determine the side effects of the previous perturbation on the wing aerodynamic characteristics, the pressure coefficient for several sections on the crosswise direction either for the wing with and without end-plate was plotted in figure 5.20.

Regarding the wing-wall junction from the pressure coefficient plots, as expected from the observed

skin friction lines, the secondary flow impact on the wing properties is negligible in contrast to the results of a wing with symmetry conditions in figure 5.12. As a consequence, the properties of the wing with or without a wall on the wing-root are identical, as illustrated in the histogram of figure 5.27.

On the other hand, the end-plate attachment at the wing-tip increased the global wing pressure distribution. From the pressure coefficient plot in figure 5.20(b) and the skin friction lines in figure 5.17, the pressure increase derives from a lower interference of the crosswise velocity on the pressure side. As a result, the wing lift properties substantially increased when compared to wings without end-plate, as illustrated in the histogram of figure 5.27.

Finally, since the pressure coefficient distribution of the wing with end-plate remained identical to that illustrated in figure 5.14(a), the induced angle of attack kept unchanged.

5.5 MotoGP Case Study

From the lifting line theory, the most efficient way to produce downforce is by increasing the wing AR. However, from regulation, the MotoGP wings are limited in span-length. As a consequence, from the results depicted in section 2.2.3, to produce the demanded downforce are required more wings. From the 2017/2018 MotoGP season, the prototypes were forced by regulation to close the side-wings for safety reasons. As a result, a lot of different box-wings designs were developed throughout the years.

Throughout this chapter was discussed that the low AR wings enhance the pressure communication between the suction and pressure side, changing the effective wing angle of attack. As a result, the lift force decreases and the upwash velocity induce additional drag forces to the wing. The box-wings design aims to reduce this pressure communication between the wing surfaces reducing the upwash effect. Although, from [31], this upwash decrease is achievable for a certain distance between the upper and lower wing. Otherwise, the interference between each other could cause worse aerodynamic characteristics.

In this section, one of the box-wings set-ups racing in MotoGP will be studied for three different distances between the lower and upper wing. The upper and lower wings have as cross-section a NACA23015 and the connecting wing is a NACA0006. The angles of attack of both wings are identical and the distance between the upper and lower wings changed between a half wing-span, one wing-span and three and a half wing-span.

5.5.1 Box-Wings

Following the same analysis of previous sections, on figures 5.21, 5.22 and 5.23 are plotted the skin friction lines on the wing surfaces for the three wings with different gaps. For the three numerical results, the flow pattern on the outer side of the wing, which includes the upper wing pressure side and lower wing suction side, is similar to the finite-wing without end-plate in figure 5.15. The cause of this similarity is illustrated on the secondary flow after the trailing-edge for the wing with the shorter gap in figure 5.25, where the pressure communication between the upper and lower wing through the outer side

is observed. The observed secondary flow emerges two tip-vortex illustrated on the secondary flow isolines in figure 5.24.

Concerning the inner side of the box-wing, due to the high proximity of the upper and lower wing, the flow patter changed utterly. For the three configurations, the interference is high enough to change the separation bubble position. For the wing with the lower gap on the upper wing, the laminar separation that took place at 10% of the wing-chord due to the wings proximity is located at more than 50% of the wing-chord. Similarly, at the lower wing, the separation bubble changed its position in the opposite direction with an early laminar separation. As long as the gap increases, the interference decreases and the separation bubbles move towards its initial position.

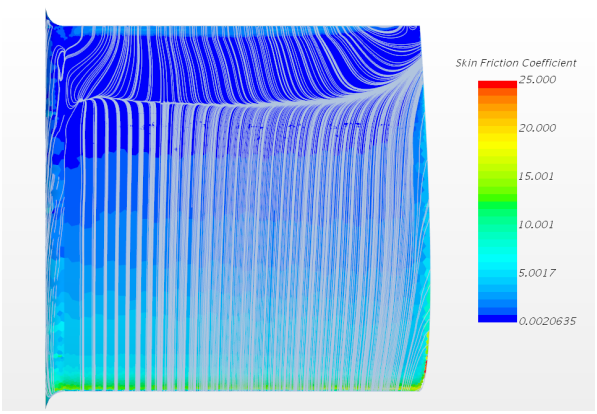

(a) Skin friction lines of the pressure side of the upper-wing

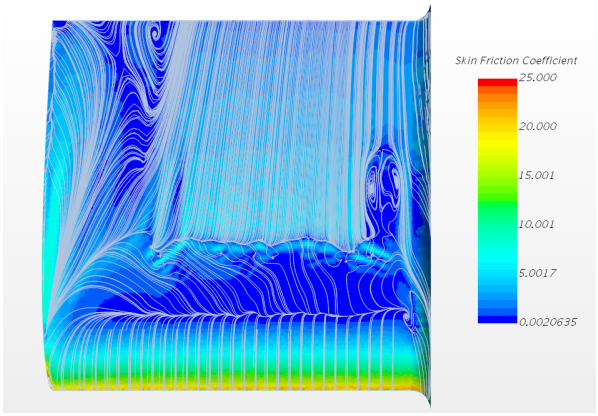

(b) Skin friction lines of the suction side of the bottom-wing

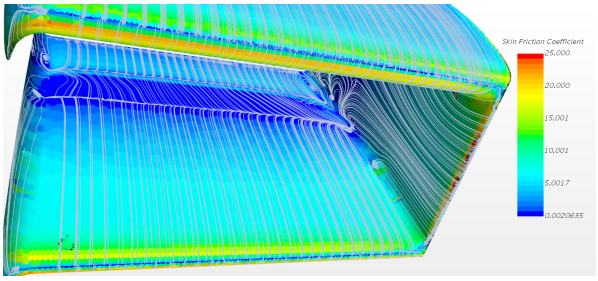

(c) Skin friction lines of the pressure side of the bottom-wing

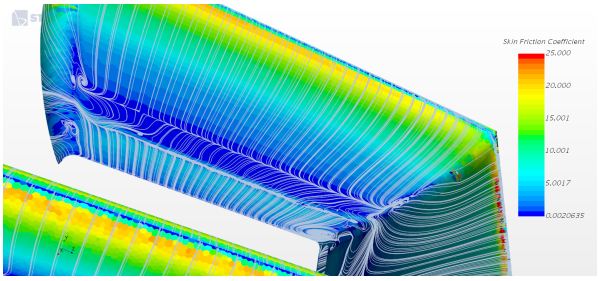

(d) Skin friction lines of the suction side of the upper-wing

Figure 5.21: Skin friction lines of the close-wing with half span length distance at $Re = 3.6 \cdot 10^5$ and 6º AoA

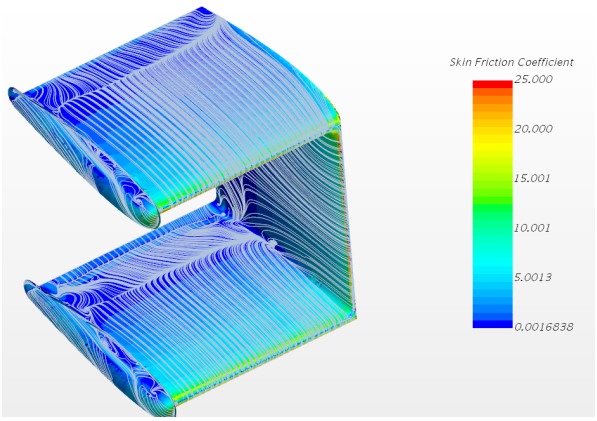

(a) Isometric view over the wall skin friction lines of the pressure side of the closed wings

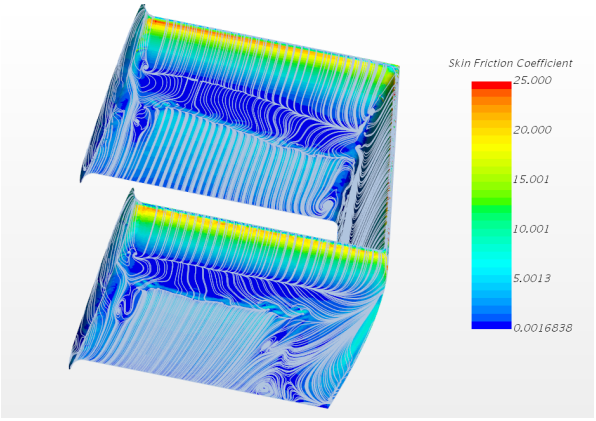

(b) Isometric view over the skin friction lines of the suction side of the closed wings

Figure 5.22: Isometric view over the skin friction lines of closed wings with a span length distance at $Re = 3.6 \cdot 10^5$ and 6º AoA

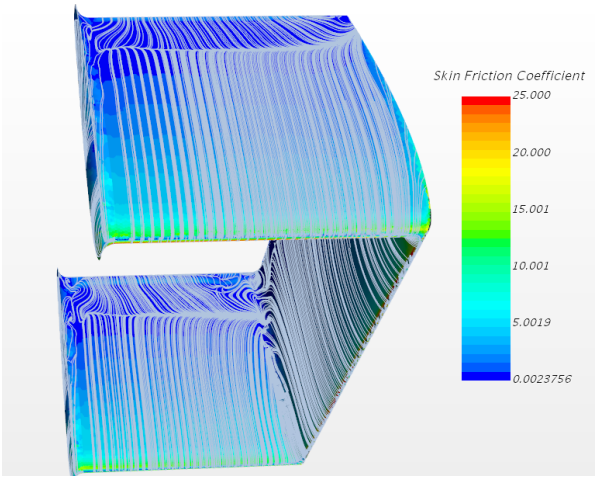

(a) Isometric view over the skin friction lines of the pressure side of the closed wings

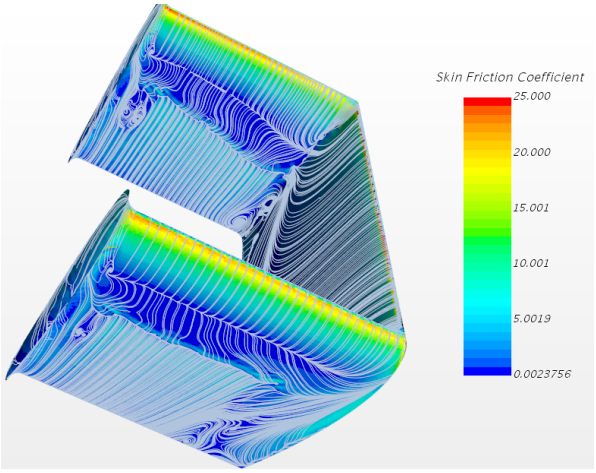

(b) Isometric view over the skin friction lines of the suction side of the closed wings

Figure 5.23: Isometric view over the skin friction lines of closed wings with three half of a span length distance at $Re = 3.6 \cdot 10^5$ and 6º AoA

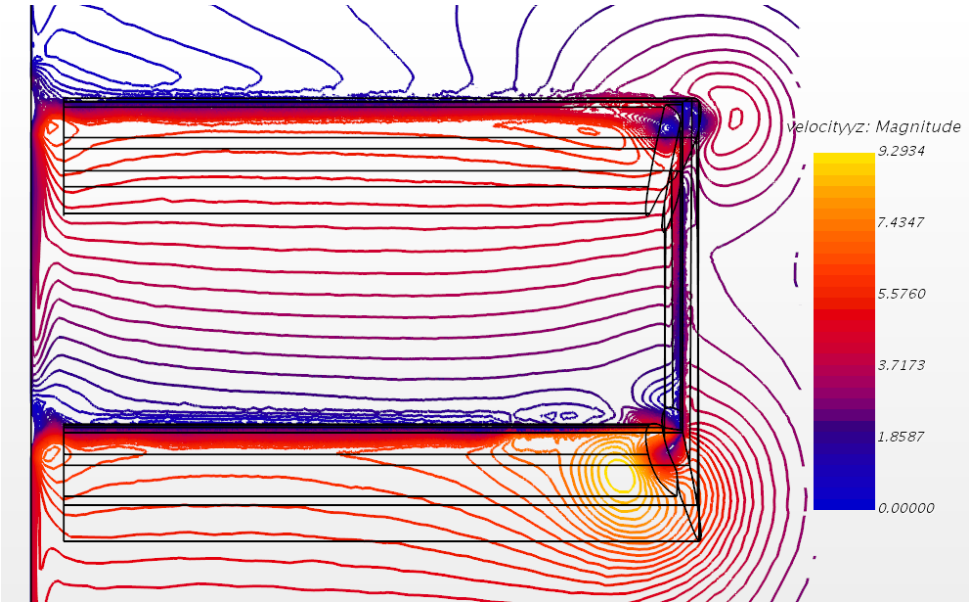

Figure 5.24: Velocity isolines after the trailing-edge for the lower gap box-wing with no-slip condition on the wing root at $Re = 3.6 \cdot 10^5$ and 6ºAoA

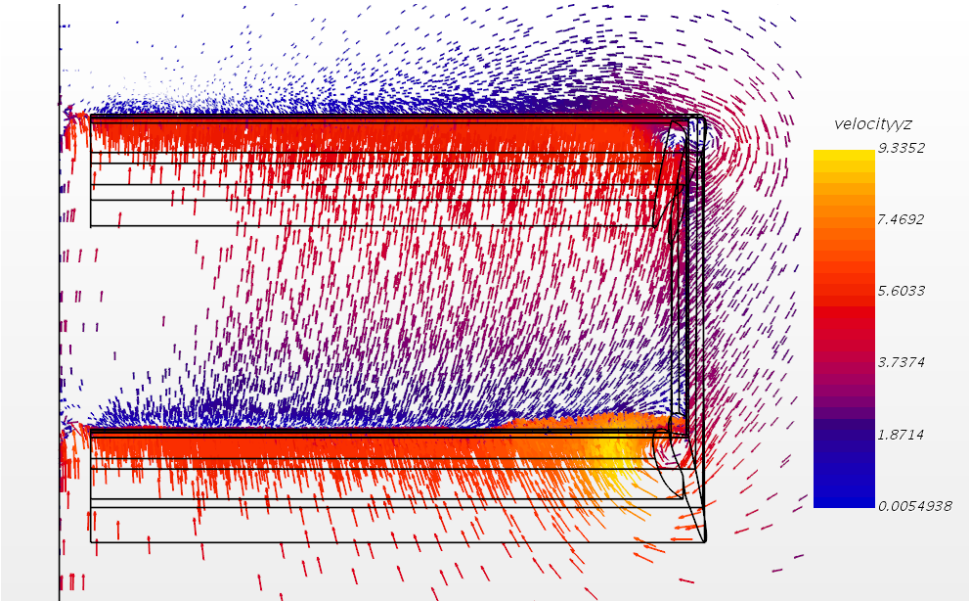

Figure 5.25: Velocity vectors after the trailing-edge for the lower gap box-wing with a no-slip condition on the wing root at $Re = 3.6 \cdot 10^5$ and 6ºAoA

The flow interference illustrated on the limiting flow lines is a consequence of the flow acceleration at the inner side of the box-wing. The wings proximity works as a nozzle increasing the kinetic energy of the flowing medium at the expense of its pressure. As a result, the upper wing end-up more loaded than the lower one, as illustrated on the pressure coefficient distribution for the three configurations. The most interesting case study regards the smaller gap set-up where the upper wing got extremely loaded and the lower one becomes neutral.

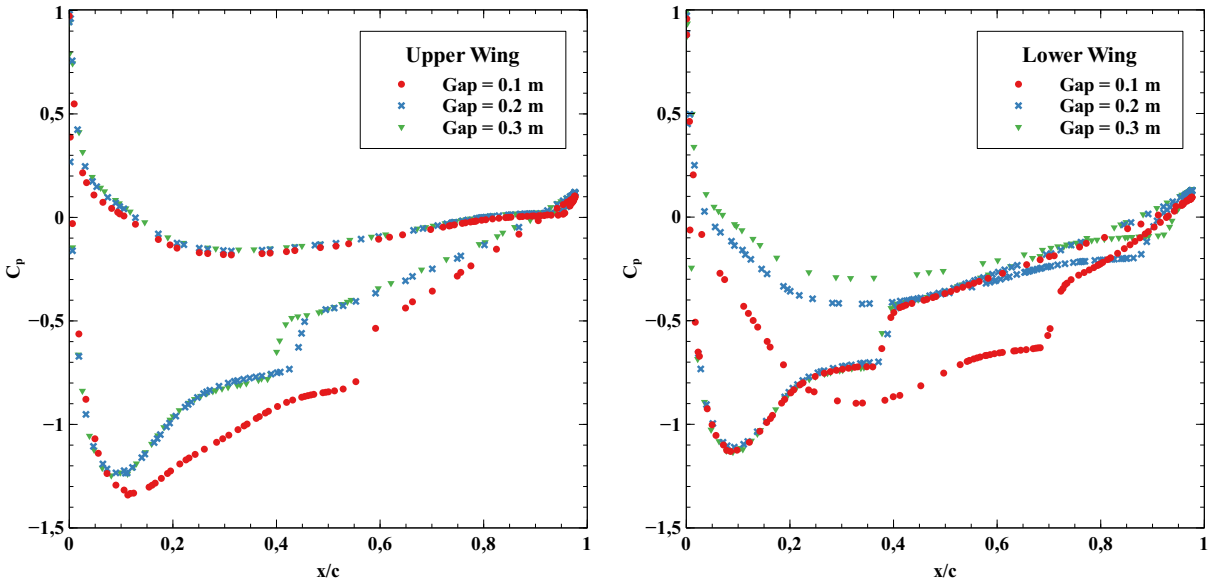

(a) C_P distribution in different sections of the upper wing along the span in the crosswise direction at $Re = 3.6 \cdot 10^5$ and 6ºAoA

(b) C_P distribution in different sections of the upper wing along the span in the crosswise direction at $Re = 3.6 \cdot 10^5$ and 6ºAoA

Figure 5.26: C_P distribution in different sections of the upper and lower wing from the box-wing set-up along the span in the crosswise direction at $Re = 3.6 \cdot 10^5$ and 6ºAoA

In conclusion, for the three different gaps studied in this section, the high interference levels between wings decrease the global wing efficiency, illustrated in histogram 5.27. Overall, if the space available through the motorcycle fairing constrains the total number of wings, then overlapping two wings may not be the most efficient way to produce downforce, but at least it is a way to produce more downforce with a low drag cost.

5.6 Final Considerations

5.6.1 Wings Performance Overview

Concerning the low $\mathcal{AR}$ wings, it is now possible to state that regardless of the set-up, the downforce loss caused by the upwash velocity is considerably high. It is also possible to state that, for the five different set-ups, the separation bubble is highly sensitive to the three-dimensional effects leading to changes in the flow characteristics and the global wing properties as well.

As can be observed in the histogram present in figure 5.27, the end-plate attachment to a finite wing substantially increases the lift coefficient, proving to be the most efficient way to produce downforce.

Lastly, closed-wings results enable us to infer that the flow interference between wings decreased the downforce efficiency, even so, for greater gap distances, it shows advantages comparing to the wing without end-plate.

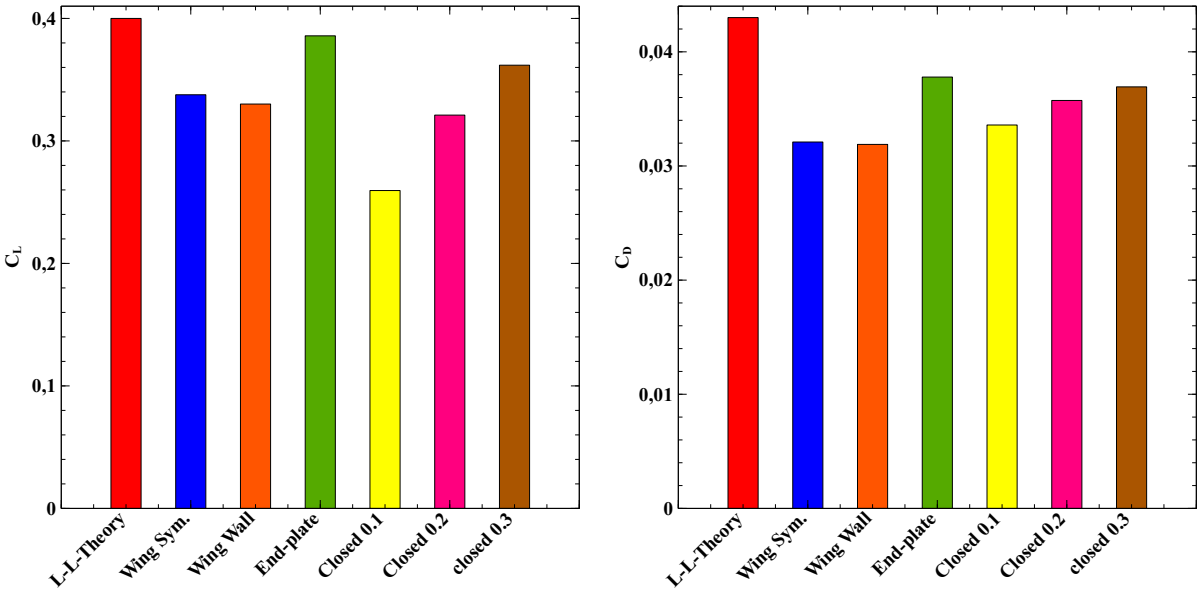

(a) Lift coefficient for the different set-ups and for the lifting line theory as well

(b) Drag coefficient for the different set-ups and for the lifting line theory as well

Figure 5.27: Histogram with the properties for the different set-ups as well the theoretical prediction from the lifting line theory. The lift and drag coefficient of the closed wings is calculated with twice the reference area of the other wings configurations.

5.6.2 Transition Model

Along the dissertation became clear that, for this Reynolds regime, the transition may occur anywhere over the wing surface. Thereby, an appropriate modelling for the transition between flow regimes is crucial to determine the flow properties and the separation bubble location. In chapter 3 was enlightened that turbulence models as $SST\ \kappa - \omega$ by themselves were not developed to determine transition. For these models, the transition is dependent on the model turbulence production. Nowadays, for several applications, the $SST\ \kappa{-}\omega$ acts very accurately and with a lower computational effort than the demanded by transition models. Although, concerning the studied Reynolds regime, the coupling of a transition model can be particularly important.

2D Results

To determine the transition model dependency under these Reynolds regimes, a two-dimensional analysis will be performed to the NACA23015 at $Re = 3.6 \cdot 10^5$ and $6\ ^\circ$ angle of attack only by coupling the $SST\ \kappa - \omega$ turbulence model to the RANS.

As expected for the two-dimensional analysis, the flow characteristics and transition location changed completely. From pressure and friction coefficient results for the NACA23015 in figure 5.28, the turbu-

lence model predicts the transition closer to the leading-edge on both sides and can not determine the boundary layer separation.

Concerning the wing lift properties, from the pressure coefficient plot illustrated in figure 5.28(b), the separation bubble predicted by the transition model increases the airfoil pressure distribution.

Regarding the drag forces, once the transition takes place sooner for either side from the skin friction coefficient plot in figure 5.28(a), the turbulent boundary layer will cover a greater part of the airfoil, and consequently, the friction drag increases.

As a conclusion, the $SST\ \kappa - \omega$ by itself can not predict the separation bubble phenomenon that in this Reynolds regime play a major role. From the numerical results, for two-dimensional analyses the lack of a transition model coupled with the turbulence model for this Reynolds regimes is not advisable.

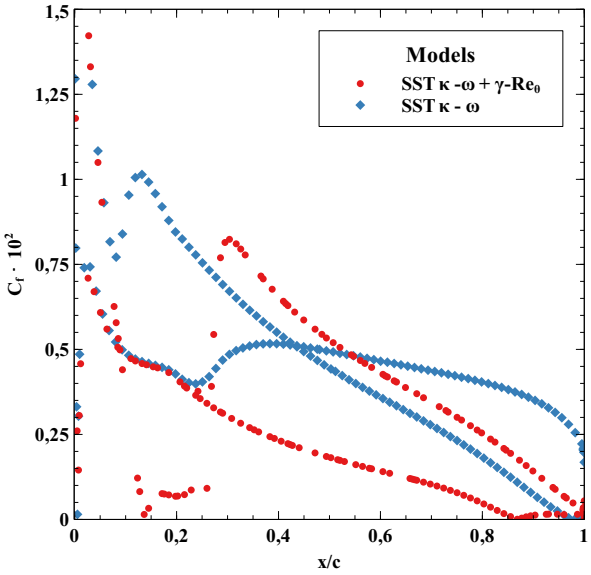

(a) C_f distribution for the NACA23015 with and without transition model for $Re = 3.6 \cdot 10^5$ and 6ºAoA

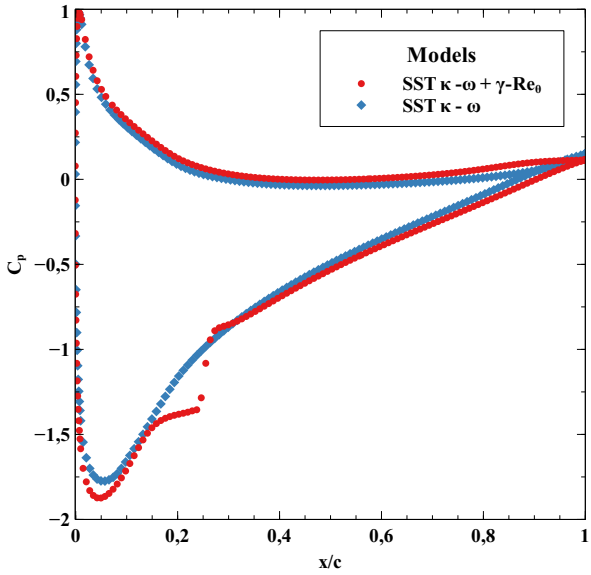

(b) C_p distribution for the NACA23015 with and without transition model for $Re = 3.6 \cdot 10^5$ and 6ºAoA

Figure 5.28: C_f and C_p distribution for the NACA23015 with and without transition model for $Re = 3.6 \cdot 10^5$ and 6ºAoA

3D Results

To determine the consequences of not coupling a transition model in the three-dimensional analysis was tested the closed-wing with half a chord gap. From the skin friction lines, in figure 5.29 and 5.30, plotted on the wing surfaces, the flow behaves according to the two-dimensional results in figure 5.28. The separation bubble as a transition mechanism vanished and was replaced by a natural transition near the leading-edge. As a consequence, the boundary layer developed in the streamwise direction behaves much differently when compared to the boundary layer development illustrated in figure 5.21 with the transition model.

Concerning the box-wing outer side, the limiting flow lines deflection near the wing tip is less steep than that predicted by the transition model, illustrated in figure 5.21(a).

Although the turbulence model can not predict the flow field accurately, from table 5.3, the lift coef-

ficient is similar to the one predicted by coupling the transition model. This result is expected since the lift properties of a low AR wing rely on the upwash effects that can be predicted either with or without the transition model. On the other hand, the separation bubble as a key role in the wing drag properties. Since the turbulence model $SST\ \kappa - \omega$ predicts the boundary layer transition closer to the leading-edge either for the pressure and suction side, the wing drag coefficient is overestimated, as depicted in table 5.3.

In conclusion, the boundary layer transition has an important role in the flow characteristics for these Reynolds regimes and the lack of a transition model would result in a poor prediction of the wing aerodynamic characteristics.

(a) Skin friction lines of the pressure side of the upper-wing without transition model for $Re = 3.6 \cdot 10^5$ and 6°AoA

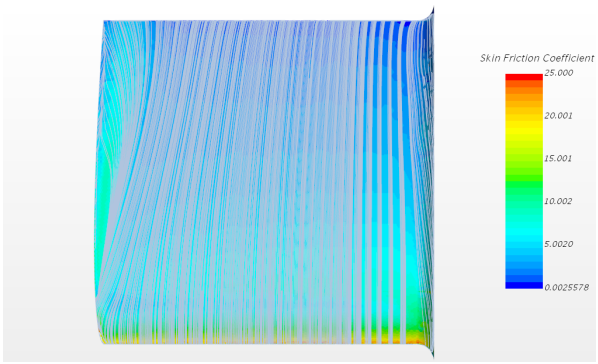

(b) Skin friction lines of the suction side of the bottom-wing without transition model for $Re = 3.6 \cdot 10^5$ and 6°AoA

Figure 5.29: Skin friction lines of the outside surface of the close-wing with half span length distance without transition model for $Re = 3.6 \cdot 10^5$ and 6°AoA

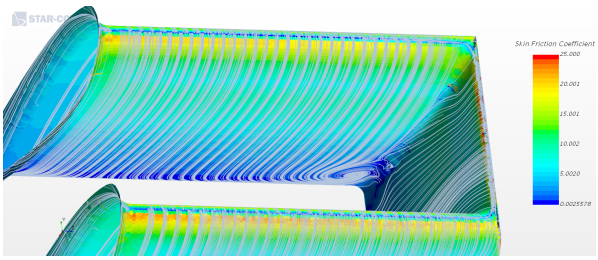

(a) Skin friction lines of the suction side of the upper-wing without transition model for $Re = 3.6 \cdot 10^5$ and 6°AoA

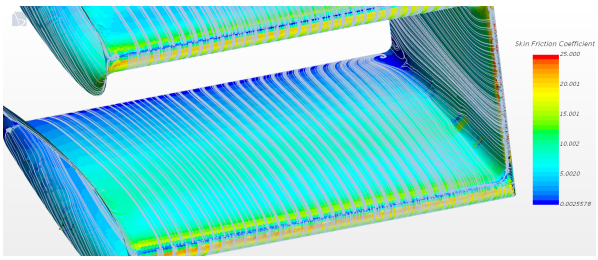

(b) Skin friction lines of the pressure side of the bottom-wing without transition model for $Re = 3.6 \cdot 10^5$ and 6°AoA

Figure 5.30: Skin friction lines of the inner side surface of the close-wing with half span length distance without transition model for $Re = 3.6 \cdot 10^5$ and 6°AoA

	C_L	$C_{DP} \cdot 10^3$	$C_{Df} \cdot 10^3$
$[\kappa - \omega]_{2D}$	0.712	7.03	9.88
$[(\kappa - \omega) + (\gamma - Re_\theta)]_{2D}$	0.811	8.93	6.38
$[\kappa - \omega]_{3D}$	0.249	23.74	13.07
$[(\kappa - \omega) + (\gamma - \ Re_\theta)]_{3D}$	0.260	26.56	7.03

Table 5.3: Solution of the properties for the two-dimensional and three-dimensional analysis with and without transition model

Chapter 6

Conclusions

The main target of this dissertation was the influence of the transient and three-dimensional effects on the side-wings performance. This objective encompassed three main stages: A steady-state analysis to the wing airfoil section regarding the MotoGP velocity ranges; A transient analysis for the same airfoil, considering the unsteady process flow associated to a circuit motorcycle racing; And finally, an analysis to three different finite wings like that used by MotoGP.

The main conclusions are:

- Firstly, throughout the dissertation, to reliably determine the flow characteristics and the wing aerodynamic characteristics under moderate Reynolds numbers was crucial to couple the transition model $\gamma - Re_\theta$ to solve the RANS equations. The turbulence model, by itself, was not able to predict the exact transition location, neither the separation bubble phenomenon.

- The flow characteristics showed a high sensibility to the income flow turbulence conditions. Consequently, to determine the wings aerodynamic characteristics accurately, the information regarding turbulence should be provided.

- The separation bubble proved to have a key role in the flow features. Under the two-dimensional analysis were determined that near the stall region, this bubble can induce different stall mechanisms that depend on the free-stream flow conditions. As a result, for safety reasons, when the motorcycle undergoes a deceleration, the wing angle of attack should be controlled to avoid the unstable effects due to the wing stall.

- Concerning the motorcycle behaviour during a lap in a circuit, neither the acceleration nor the deceleration affected the airfoil aerodynamic characteristics. Likewise, the wing performance is not sensitive to the pitching motion regarding the motorcycle suspension frequencies. As a result, a quasi-steady approach is sufficient to determine the wing aerodynamic characteristics.

- Regarding the finite-wing results, due to the span-length restriction from MotoGP regulation, the prototypes side-wings end-up highly prone to three-dimensional effects. As a result, the downforce of these wings decreases in more than 50% in contrast to higher aspect ratio wings.

- For the three set-ups depicted in this dissertation, the attachment of an end-plate proved to be the more efficient way to produce downforce. However, since the MotoGP regulation forbids these wings as a safety feature, the manufactures are restricted to design box-wings. For the studied configuration of two overlapped wings, besides the interferences between them have decreased the set-up efficiency, the global downforce increased 30% about the wing with end-plate.

6.1 Future work

Concerning the three-dimensional results, different subjects would be interesting to explore in the future. In the present dissertation, the motorcycle fairing was approximated to a flat plate. However, these wings are attached to a region where the fairing shape induces a favourable pressure gradient to the flow. It would be worthwhile to determine how different fairing shapes can affect the wing aerodynamic characteristics due to the flow acceleration near the motorcycle fairing.

In addition, the three-dimensional analysis of different wing configurations opened doors to different ideas to increase the MotoGP box-wings performance. Since MotoGP wings are constrained to the available space on the motorcycle, it is required to study a way to decrease the flow interference between the upper and lower wing. As a future work, to optimize the box-wings in different configurations is suggested to change different parameters to decrease the flow interference. To increase the global downforce is required to decrease the influence of the flow acceleration on the lower wing. That can be handled by managing the angles of attack of the upper and lower wing, the gap, or the position between them.

Bibliography

[1] J. Winslow, H. Otsuka, B. Govindarajan, and I. Chopra. Basic Understanding of Airfoil Characteristics at Low Reynolds Numbers (104–105). *Journal of Aircraft*, 55(3):1050–1061, 2017. ISSN 0021-8669. doi: 10.2514/1.c034415.

[2] A. Marta. Hydrodynamic analysis of a slalom fin of windsurf board. (December), 2018.

[3] R. Miguel and A. Lopes. Calculation of the flow around hydrofoils at moderate Reynolds numbers. (December), 2015.

[4] B. H. a. Smith and R. F. Schaefer. for Aeronautics Technical Note 2074. (April):0–10, 1950.

[5] R. E. Sheldahl and P. C. Klimas. Sandia_Lab_Data. 1981. doi: 10.2172/6548367.

[6] H. Roohani. *Aerodynamic effects of accelerating objects in air*. Number September. 2010. ISBN 9780620431668.

[7] Z. J. Wang. Vortex shedding and frequency selection in flapping flight. *Journal of Fluid Mechanics*, 410:323–341, 2000. ISSN 00221120. doi: 10.1017/S0022112099008071.

[8] M. E. Rosti, M. Omidyeganeh, and A. Pinelli. Video: Dynamic stall of an aerofoil in ramp-up motion. In *69th Annual Meeting of the APS Division of Fluid Dynamics - Gallery of Fluid Motion*. American Physical Society, nov 2016. doi: 10.1103/APS.DFD.2016.GFM.V0044. URL `https://gfm.aps.org/meetings/dfd-2016/57d02d43b8ac3117910004d8`.

[9] J. Guerrero. Aerodynamics of Flapping Flight. *Numerical Simulation of the unsteady Aerodynamics of flapping flight*, pages 7–33, 2009. URL `http://www.dicat.unige.it/guerrero/thesis.html`.

[10] V. de Brederode. *Aerodinâmica Incompressível Fundamentos*. 1997.

[11] O. F. Low-aspect ratio, T. O. The, N. F. Copy, P. Retli, N. T. O. Coo, and N. Aeronautics. Technical note. (July 1961), 2019.

[12] V. Sedlak. Motorcycle cornering improvement : An aerodynamical approach based on flow interference (MSc thesis). page 54, 2012.

[13] V. Cossalter. *Motorcycle Dynamics 2nd Edition*. 2006. ISBN 9781447532767.

[14] FIM. Fim World Championship. 2016.

[15] K. Gemba. Measurement of Boundary Layer on a Flat Plate. *California State University*, (1):1–12, 2007. URL http://web.iitd.ac.in/{~}pmvs/mel705/boundarylayer.pdf.

[16] E. Hussein and M. El. Boundary-Layer Theory of Fluid Flow past a Flat-Plate: Numerical Solution using MATLAB. *International Journal of Computer Applications*, 180(18):6–8, 2018. doi: 10.5120/ijca2018916374.

[17] A. H. Techet. 2.016 Hydrodynamics. Technical report.

[18] J. Y. Andro and L. Jacquin. Frequency effects on the aerodynamic mechanisms of a heaving airfoil in a forward flight configuration. *Aerospace Science and Technology*, 13(1):71–80, 2009. ISSN 12709638. doi: 10.1016/j.ast.2008.05.001.

[19] M. Saif, U. Khalid, I. Akhtar, and N. I. Durrani. Aerodynamic Characteristics of Pitching and Plunging Airfoils at Low Reynolds Number. pages 1–28, 2014.

[20] H. Versteeg and W. Malalasekera. *An Introduction to Computational Fluid Dynamics*, volume M. 2007. ISBN 9780131274983. doi: 10.2514/1.22547. URL http://www.ncbi.nlm.nih.gov/pubmed/6686412.

[21] F. R. Menter. Zonal Two Equation k-cl, Turbulence Models for AIAA 93-2906 Aerodynamic Flows. 1993.

[22] C. L. Rumsey and P. R. Spalart. Turbulence model behavior in low reynolds number regions of aerodynamic flowfields. *AIAA Journal*, 47(4):982–993, 2009. ISSN 00011452. doi: 10.2514/1.39947.

[23] F. Joel and L. Gamboa. Numerical Analysis of an Wing Sail Aerodynamic Characteristics Using. 2010.

[24] Robin Blair Langtry. A Correlation-Based Transition Model using Local Variables for Unstructured Parallelized CFD codes. 2006. URL https://elib.uni-stuttgart.de/bitstream/11682/1722/1/Kap01{_}05{_}1.pdf.

[25] C. Hirsch. *Numerical Computation of Internal & External Flows By C. Hirseh (Vol.-2)*. 1990. ISBN 0471923516.

[26] E. Committee. Solution of Flows Around Airfoils Using RANS with Wall-Functions. (October), 2014.

[27] M. Hoekstra. DRAFT-OMAE2010-20338. pages 1–9, 2016.

[28] S. Burmester and G. Vaz. DRAFT : Towards credible CFD simulations for floating offshore wind turbines.

[29] L. E. Schwer. Is your mesh refined enough? Estimating Discretization Error using GCI. *7th LS-DYNA Anwenderforum*, 1(1):45–54, 2008.

[30] F. Gand, S. Deck, V. Brunet, P. Sagaut, F. Gand, S. Deck, V. Brunet, and P. Sagaut. Flow dynamics past a simplified wing body junction Flow dynamics past a simplified wing body junction. 115111, 2010. doi: 10.1063/1.3500697.

[31] F. Khan, P. Krammer, and D. Scholz. Preliminary Aerodynamic Investigation of Box-Wing Configurations Using Low Fidelity Codes. *Deutscher Luft- und Raumfahrtkongress, DocumentID: 161308*, pages 313–327, 2010.

[32] Motorcycle Specifications, . URL https://motorcyclespecs.co.za/index.htm.

[33] Specs of 2015 - 2016 Yamaha R1, . URL https://motoperf.com/motorcycles/Yamaha-R1-2015-284011.

[34] Ducati Team MotoGP: Bike. URL https://www.ducati.com/ww/en/racing/motogp/ducati-team-bike-desmosedici-gp.

[35] Foale. Motorcycle Handling And Chassis Design Foale. 2011. doi: 10.1360/zd-2013-43-6-1064.

[36] Brembo 340 mm discs are obligatory for the heavy deceleration at Motegi — Brembo - Official Website. URL https://www.brembo.com/en/company/news/motogp-motegi-brembo-brake.

Appendix A

Motorcycle Dynamics

Single-track vehicles are known for their unique attributes. The lack of lateral stability introduces a significant complexity when it comes to dynamics behaviour. Moreover, track motorcycles are the categories where the synergies between the rider-bike become crucial to push both to the limits. Nowadays, the sensor systems are fundamental for setting up a motorcycle to a specific rider, thus making the evolution faster. On the other hand, the dynamic know-how of these vehicles is fundamental before any set-up. The following chapter will outline the basic motorcycle principles, section A.1, which are the fundamentals to set up any motorcycle.

A.1 Motorcycle Principles

To deeply get into the motorcycle dynamics, this section will be split into two main topics. The section A.1.1, establish the basic motorcycle geometry parameters followed by a simplified approximation of the rectilinear motion equations and steady turning, taken from [13]. The section A.1.2 covers the in-plane dynamics topic, also discussed in [13], passing through the geometric motorcycle variation up to the dynamic motorcycle response after being perturbed by forces.

A.1.1 Rectilinear motion and steady turning

The suspension work and material deformation are reasons why motorcycle does not show rigid body behaviour. By neglecting this motion, it is plausible to get an appropriate approximation of the system's instantaneous force reaction to a perturbation.

Figure A.1 and A.2, from [13], represents the acting forces in rectilinear motion and steady turning, respectively. As it is clear from figure A.1, there are a few prominent geometric parameters that characterize a motorcycle. The center of gravity position (X_{CG}) determines the motorcycle weight distribution and behaves like a lever of the gravity force (F_g) and lift force (F_L). The Wheelbase (WB), apart from establishing the X_{CG} value, it also contributes to the motorcycle maneuverability, cornering speed and even directional stability [13], which makes its value dependent on the motorcycle category.

Moreover, the center of gravity height (Y_{CG}) bounds the 2D plane and transverse plane motion, figure

A.1 and A.2, respectively. During acceleration or deceleration, figure A.1, the Y_{CG} acts as the inertial forces (ma) and drag forces (F_D) lever and depending on the track slope (α) it is also one of the gravity force components levers. In addition, considerable heights of the gravity center may lead to premature loss of wheel contact to the ground.

Over a lap on a circuit motorcycles may experience three different dynamic scenarios: acceleration,

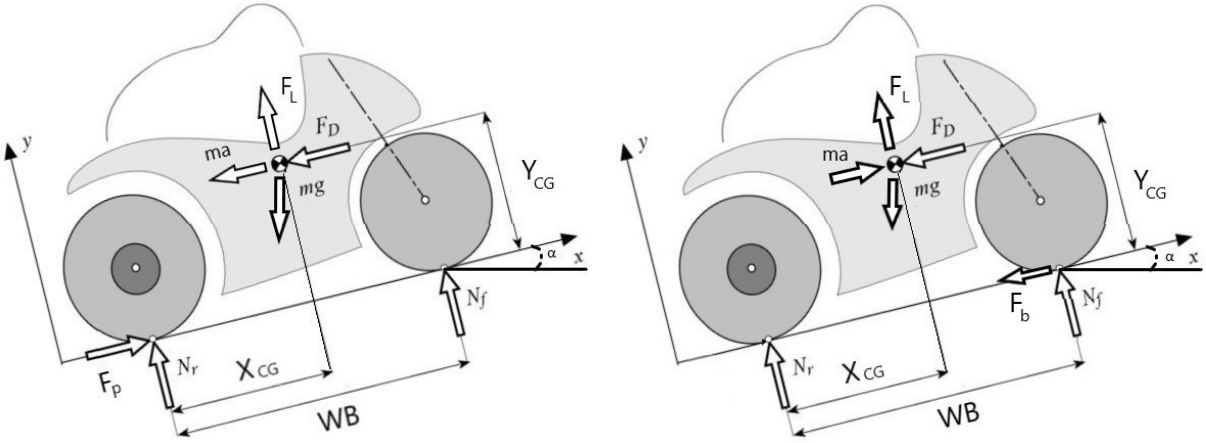

(a) Vector representation of acceleration motion

(b) Vector representation of deceleration motion

Figure A.1: Vector representation of rectilinear motion forces

deceleration, and cornering. The acceleration values differ a lot depending on the category, typically it is related to the engine power (or driving force (F_p)).

During acceleration, not only the engine needs the power to overcome the motorcycle and rider mass, but also to overcome the inertial forces exerted by the moving parts. Wheels, gear-box, engine pistons are examples of mechanical elements that contribute to this inertial forces, and sometimes it could correspond to move an extra mass of $20kg$,[13]. Due to the extra mass high value, for the further calculus, it will be considered an equivalent mass (m_a) given by the sum of the motorcycle-rider mass and the extra mass.

On the whole, the equation A.1 defines the equilibrium of forces and momentum set on the contact point between the rear wheel and the ground, figure A.1(a), [13].

$$\begin{cases} N_r + N_f + F_l - F_g cos(\alpha) = 0 \\ F_p - F_d - F_g sen(\alpha) - (m_a)a = 0 \\ N_f WB + m_a a Y_{CG} + F_d Y_{CG} + F_l X_{CG} + F_g sen(\alpha) Y_{CG} - F_g cos(\alpha) X_{CG} = 0 \end{cases} \tag{A.1}$$

Similarly to acceleration, the deceleration ability of a motorcycle is mainly limited by its geometry and tires condition. Figure A.1(b) represents the deceleration scenario, only considering the front brake force (F_b). Settled the forces and momentum equilibrium on the contact point between the front wheel and the ground, system A.2 defines deceleration motion, [13].

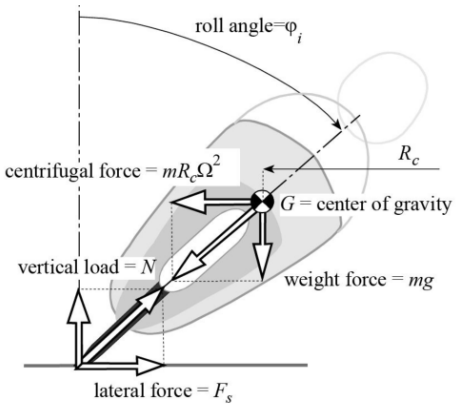

Figure A.2: Steady turning assuming that motorcycle has zero thickness tires

$$\begin{cases} N_r + N_f + F_l - F_g cos(\alpha) = 0 \\ -F_{bfront} - F_{brear} - F_d - F_g sen(\alpha) + m_a a = 0 \\ -N_r WB - m_a a Y_{CG} + F_d Y_{CG} - F_l(\Delta x) + F_g sen(\alpha) Y_{CG} + F_g cos(\alpha)(\Delta x) = 0 \\ \Delta x = WB - X_{CG} \end{cases} \tag{A.2}$$

Cornering dynamics constitute a world of their own within motorcycle dynamics analysis. The material deformation, gyroscopic effects of the rotating bodies, and tire behavior turn out this topic challenging to predict with a linear system of equations.

For instance, it will be studied steady cornering considering three hypotheses: rigid body, gyroscopic effects negligible, and zero tire thickness, chapter 4.1.1 of [13]. This hypothesis simplifies our forces diagram to the one in figure A.2. Therefore, equation A.3 characterize the forces and momentum balance during steady cornering.

$$\begin{cases} m \times a_c = \mu_{cornering}(N_r + N_f) \\ N_f + N_r = m \times g \\ -F_g sin(\psi) Y_{CG} + m a_c cos(\psi) Y_{CG} = 0 \end{cases} \tag{A.3}$$

A.1.2 In-Plane Dynamics

Besides the assumption of a rigid body, the high suspension travel implies the existence of a sprung rigid body, represented in figure A.3. The sprung mass or the mass over the suspensions, when undergone an acceleration or deceleration should react to it in two stages:

1. During the velocity change, suspensions should compress or expand depending on the wheels' reaction (N_r, N_f). From chapter 5.3.1 of [13], the front and rear suspension travel (x_{travel}), equations A.4 and A.5 respectively, is a consequence of the spring stiffness and spring pre-load.

   The suspension system is not vertically aligned with the wheel travel, and thus it is mandatory to align the normal force by projecting it to the suspension direction. The front suspension reaction relies upon the angle between the vertical axis and the steering head axis, commonly known as the rake angle. The rear suspension is not commonly attached to the wheel axis, and consequently, it depends on a quantity called leverage ratio (LR), which determines the ratio between the rear

wheel travel and suspension travel.

$$x_{travel} = \frac{N_f \times cos(rake)}{k_{springf}} - x_{preload} \tag{A.4}$$

$$x_{travel} = \frac{N_r \times Leverageratio}{k_{springr}} - x_{preload} \tag{A.5}$$

2. Therefore, every sprung body, after being subjected to a force should oscillate at a natural frequency that may lead to the motorcycle pitch and bounce, figure A.3. To overcome these problems, suspensions integrate shock absorbers that are crucial to dissipate those frequencies. Chapters 5.9 and 5.10 of [13], explains how to get optimum damping coefficients, but to keep the linearity of equations A.4 and A.5 it will not be considered dumping factor either the presence of natural frequencies.

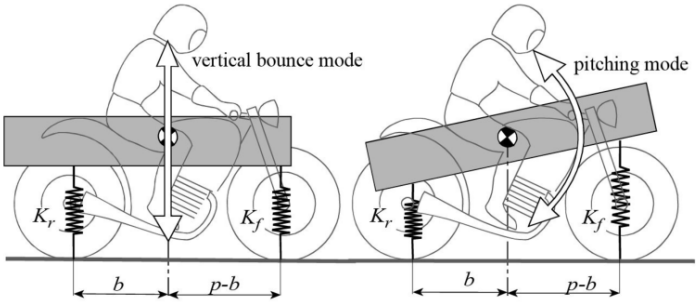

Figure A.3: Pitch and Bounce representation suffered by the unsprung mass

Appendix B

Front-End-Lift Case Study

The present case study aims to estimate the ratio between the driving force and the global weight of a motorcycle where the front-end-lift is of high concern. The objective is to determine a range of motorcycle whether the wings studied in this dissertation becomes useful.

B.1 Motorcycle Limits

In Appendix A was already determined the equations that govern the motorcycle dynamics behaviour through different dynamic situations along the track. In this section it will be outlined the fundamental equations that constrain the motorcycle power delivery during acceleration.
During acceleration, two different limits constrain engine power. The first constraint is the tire limit that occurs when the driving force exceeds the tire friction force limit:

$$F_p > \mu_{tire} N_r \tag{B.1}$$

Where μ_{tire} is the friction coefficient and N_r is the normal force at the rear tire.
The second one is the limit when the wheel starts losing contact with the ground ($N = 0$). In particular, front-end-lift or wheelie is the definition for the front tire contact loss during acceleration($N_f = 0$).
To simplify the present analysis will be neglected the track elevation, the wind effect and the inertia of moving parts. Applying the previous constraints on the system of equations A.1, the maximum acceleration that the motorcycle can perform to avoid the contact loss of the wheels with the ground and the loss of traction is given by equations B.2 and B.3, respectively.

$$a_{maxlift} < g \frac{X_{CG}}{Y_{CG}} \tag{B.2}$$

$$a_{maxtire} < \frac{\mu_{tire} \left(-\frac{X_{CG}}{WB} \right)}{1 - \mu_{tire} \frac{Y_{CG}}{WB}} \tag{B.3}$$

Where X_{CG} is the center of gravity position in the x-direction, Y_{CG} is the center of gravity position in the y-direction and WB the motorcycle wheelbase.
In addition, the acceleration that the motorcycle can deliver from the engine from the system of equations A.1 is given above:

$$a = \frac{F_p}{m} \tag{B.4}$$

Where F_p is the driving force and m the global mass, which includes the motorcycle and the rider.
From equations B.2, B.3 and B.4, it can now be established the maximum driving force that a motorcycle could deliver to avoid either the front-end-lift or the loss of traction from equation B.5 and B.6 respectively.

$$\frac{F_p}{m} < g\frac{X_{CG}}{Y_{CG}} \tag{B.5}$$

$$\frac{F_p}{m} < \frac{\mu_{tire}\left(-\frac{X_{CG}}{WB}\right)}{1-\mu_{tire}\frac{Y_{CG}}{WB}} \tag{B.6}$$

Usually, manufacturers instead of providing the driving force, provide the engine's characteristics such as the maximum engine power and torque. To determine the driving force is required to know all the gear reductions inherent to the drive-train system. For a typical drive-train system the driving force can be written as:

$$F_p = \frac{T_{engine} \times [Tpr] \times [Gbr] \times [Tsr] \times [Rst]}{Radius_{reartire}} \tag{B.7}$$

Where Tpr is the primary gear ratio, Gbr the gearbox ratio, Tsr the secondary gear ratio, Rst the ratio between the rear sprocket and the tire dimensions, T_{engine} is the engine torque and $Radius_{reartire}$ is the radius of the rear tire.

B.1.1 MotoGrandPrix Categories Assessment

In the previous section, it was established the maximum ratio between engine torque and motorcycle weight to avoid either the front-end-lift or the loss of traction. In this section, will be analysed four different motorcycle categories from the MotoGrandPrix and WSBK to estimate for which one the engine power delivery is being constrained by the two scenarios previously presented.
The main differences between the categories racing in MotoGrandPrix and WSBK are the power to weight ratios. The chosen motorcycles, representative of these categories, are depicted in table B.1. In that same table are depicted the drive-train characteristics for the different motorcycles as well as the maximum engine torque.

To accurately determine the motorcycle driving force, it would be required to map the engine torque under the engine rotation, as illustrated in figure B.1. If it is assumed that the rider uses the engine speed range where the maximum engine torque is available, illustrated in the red lines in figure B.1, then assuming the maximum engine torque for the following calculus is a good approximation. Apart from the drive-train, it is essential to establish the remaining variables that fully close equations B.2 and B.3,

-	Drive-Train									-
Motorcycles	Gbr						Tpr	Tsr	$R_{reartire}$ (m)	Max.engine torque(N/m)
	1	2	3	4	5	6				
Honda NSF250R ”Moto3”	1.88	1.52	1.30	1.17	1.08	1.00	2.95	2.33	0.301	28.00
Yamaha R6 2009 Stock	2.58	2.00	1.67	1.44	1.29	1.15	2.07	2.81	0.326	67.80
Ducati V4R 2018 ”WSBK”	2.71	2.12	1.74	1.52	1.36	1.25	1.80	2.56	0.326	112.00
Ducati V4R 2018 ”MotoGP”	2.71	2.12	1.74	1.52	1.36	1.25	1.80	2.56	0.326	120.00

Table B.1: Drivetrain table description of 4 different racing motorcycles. The drive-train values were taken from [32] and [33] except for the Ducati V4R MotoGP which is an approximation based on the MotoGP prototypes power extra power, from [34] and technical regulation.

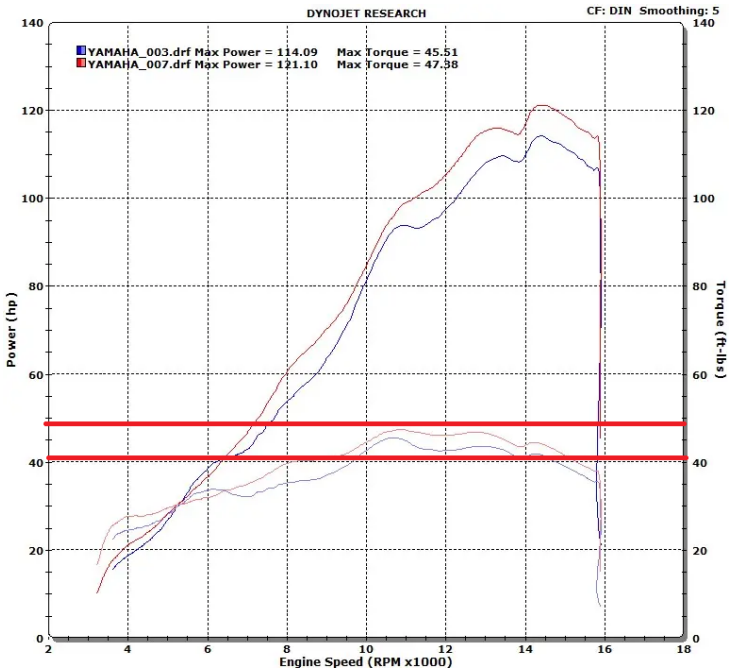

Figure B.1: Yamaha R6 2009 Stock, engine power curve.

which includes the center of gravity position, X_{CG} and Y_{CG}, the motorcycle and rider total weight and the tire friction coefficients.

For the motorcycles depicted in table B.2, it was considered an equal balanced weight distribution with rider($X_{CG} = 0.5WB$). From [35] a typical center of gravity height for a sport-bike without a rider is around $Y_{CG} = 550mm$. For instance, to take into account the rider it was used the data of the electric prototype TLMoto02e from IST university, which has the center of gravity height approximate to a typical sport-bike around $Y_{CG} = 560mm$. Including the rider weight, the center of gravity increased for approximately $Y_{CG} = 684mm$.

The weights depicted in table B.2 for the motorcycles categories included in the MotoGrandprix competition were taken from the FIM technical regulation in [14]. The Stock Yamaha was assumed its real weight and a rider with approximately $65kg$.

Finally, the tire friction coefficient was taken from [36] with the maximum deceleration that MotoGP prototypes can perform, approximately 1.5g's. From equation B.3 it is estimated a friction coefficient of approximately 1.3.

Established the remaining variables in table B.2 are depicted for each motorcycle gear the motorcycle driving force to the total weight ratios that exceed the previous dynamic constraints.

	Mass (kg)	X_{CG} (m)	$a_{maxlift}$ (m/s^2)	$a_{maxslip}$ (m/s^2)	Driving force/mass (m/s^2)					
					1	2	3	4	5	6
NSF250R "Moto3"	152	0.61	**8.92**	**22.34**	**7.91**	**6.43**	**5.50**	**4.92**	**4.54**	**4.22**
R6 Stock	265	0.70	**10.29**	**16.78**	**11.82**	**9.16**	**7.63**	**6.61**	**5.89**	**5.26**
V4R "WSBK"	233	0.74	**10.77**	**15.63**	**18.47**	**14.41**	**11.82**	**10.37**	**9.28**	**8.50**
V4R "MotoGP"	222	0.74	**10.77**	**15.63**	**20.77**	**16.20**	**13.29**	**11.66**	**10.43**	**9.56**

Table B.2: In this table are depicted the motorcycle driving force to the total motorcycle and rider weight ratios that exceeds the motorcycle dynamic constraints. The red values are the gears where the available acceleration from the engines exceeds either the front-end-lift limit and the tire slip limit. The yellow values are the gears where the available acceleration from the engines exceeds only the front-end-lift limit. The green values are the gears where the motorcycle where the available acceleration is not enough to exceed the motorcycle dynamic limits.

From the results depicted in table B.2 the main conclusions are:

- The tire acceleration limit exceeds the front-end-lift limit. As a result, the loss contact loss of the front wheel with the ground is the main concern regarding acceleration in motorcycles.
- For the Moto3 category, motorcycles engines are not powerful enough to exceed the front-end-lift limit in any gear.
- Looking to a mid-range power motorcycle as Yamaha R6 the front-end-lift is not expected to be of high concern. The result is expected since we are looking to a stock motorcycle that, besides having a considerable amount of torque, the total weight is way higher than the Moto Grand Prix prototypes or WSBK motorcycles. However, considering other aspects in dynamic equations as the motorcycle drag and track elevation, this mid-range power motorcycle might start to be constraint by the front-end-lift.
- Looking to the last two motorcycles is clear that almost for any gear the motorcycle is prone to the front-end-lift effect. Both categories include motorcycles with a higher engine power delivery and a lower global weigh. As a result not only the motorcycle end up losing the contact of the front wheel with the ground, but also for lower gears the motorcycle can lose the rear wheel traction.
- Finally, it can be established an approximation to the ratio between the engine maximum torque and the motorcycle and rider weight from where the front-end-lift should be a concern. Based on the depicted values in table B.1 and B.2, for ratios larger than $0.48Nm/kg$ the front-end-lift highly

affects the motorcycle performance. As an aside, this ratio is based on different hypothesis that neglects the track elevation and air friction forces and is based on a specific gearbox set-up. As a result, this ratio must be evaluated qualitatively

In conclusion, the achieved results proved that the motorcycle acceleration in MotoGP prototypes and WSBK motorcycles no longer relies on the engine. Consequently, aerodynamic appendices that delay the wheelie effect represent an increase in motorcycle performance.

B.1.2 Aerodynamic Forces influence on the Front-End-Lift

As already mentioned in the previous section, the driving force to weight ratios depicted in table B.2 was determined by neglecting the aerodynamic forces acting on the motorcycle. However, depending on the motorcycle velocity the front-end-lift maximum acceleration can even take lower values than the ones itemized in table B.2.

Considering the aerodynamic forces, the equation B.2 can now be written as:

$$a_{maxlift} < \frac{gX_{CG}}{Y_{CG}} - \frac{C_d A 0.5 \rho v^2}{m} - \frac{C_l A 0.5 \rho v^2 X_{CG}}{m Y_{CG}} \tag{B.8}$$

Where C_d is the motorcycle drag coefficient, C_l is the motorcycle lift coefficient, v is the motorcycle velocity and ρ the air density.

Assuming that the $C_d.A = 0.31$ from a sport motorcycle [35] and a $C_l.A = 0.07$ from the electric prototype TLMoto02e from IST university, the maximum acceleration of a Ducati MotoGP in a middle range velocity between $[40-60](m/s)$, may decrease up to $8m/s^2$, as illustrated in figure B.2. As a result, to accurately determine the maximum allowable acceleration to avoid the front-end-lift it must be considered the aerodynamic forces throughout the track.

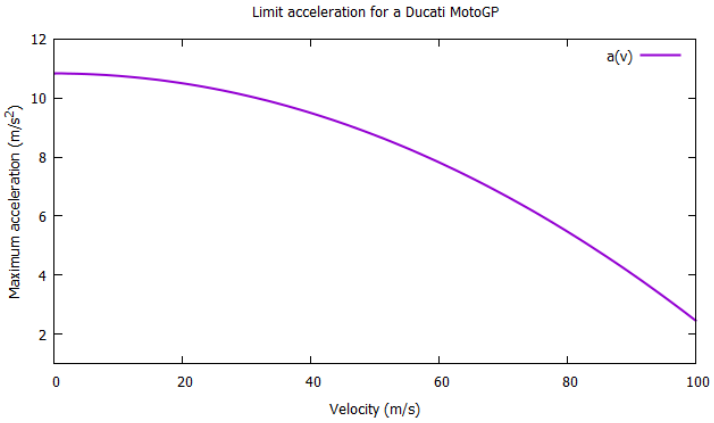

Figure B.2: Function of the maximum acceleration allowable to avoid wheelie against velocity for the Ducati MotoGP prototype presented in table B.2

Appendix C

MotoGP fairing regulation

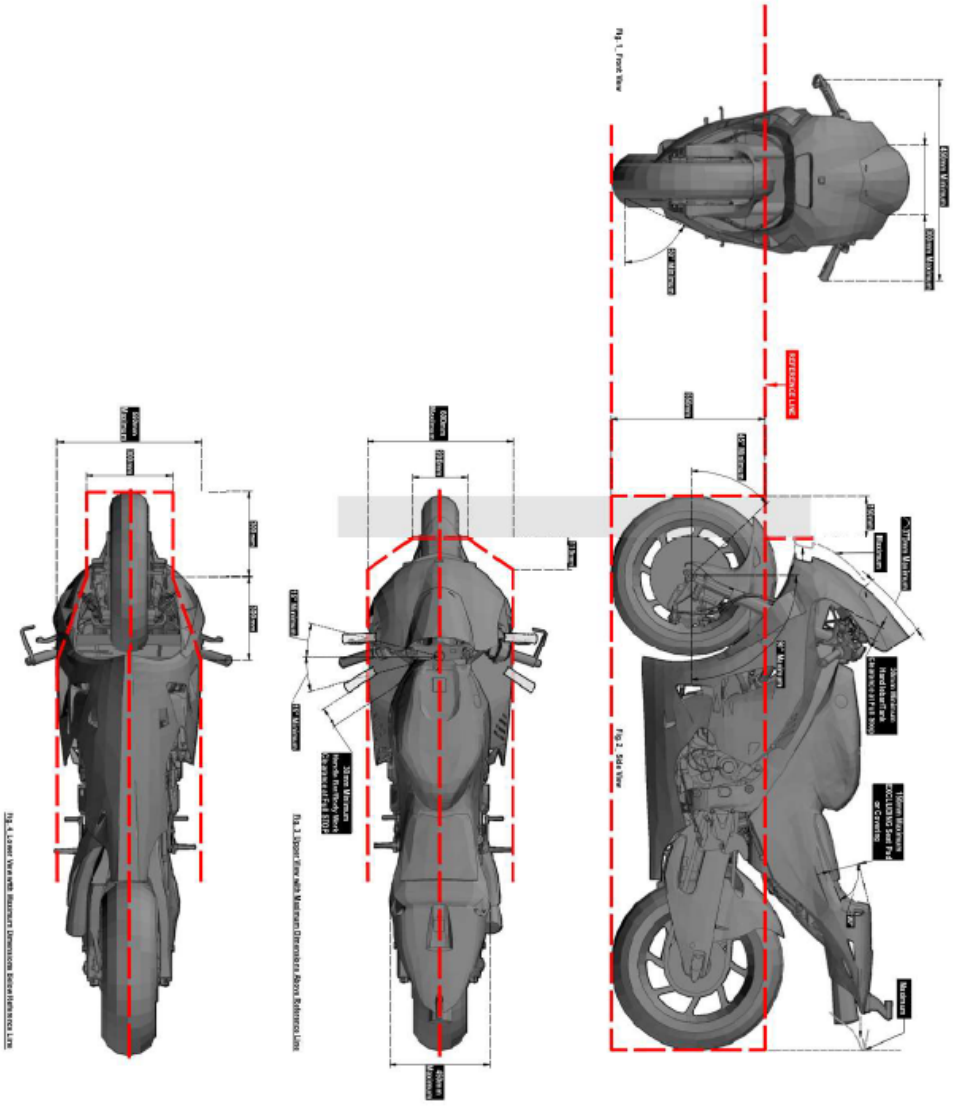

Figure C.1: MotoGP Aerofairing regulation limits,[14]. The red lines illustrate the aerodynamic components limits

Appendix D

Suspension Work Results

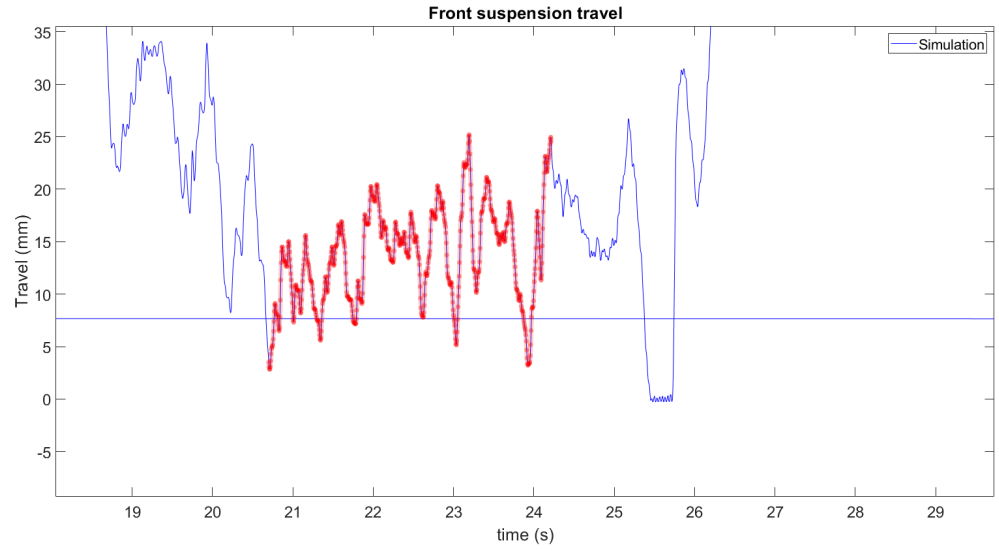

(a)

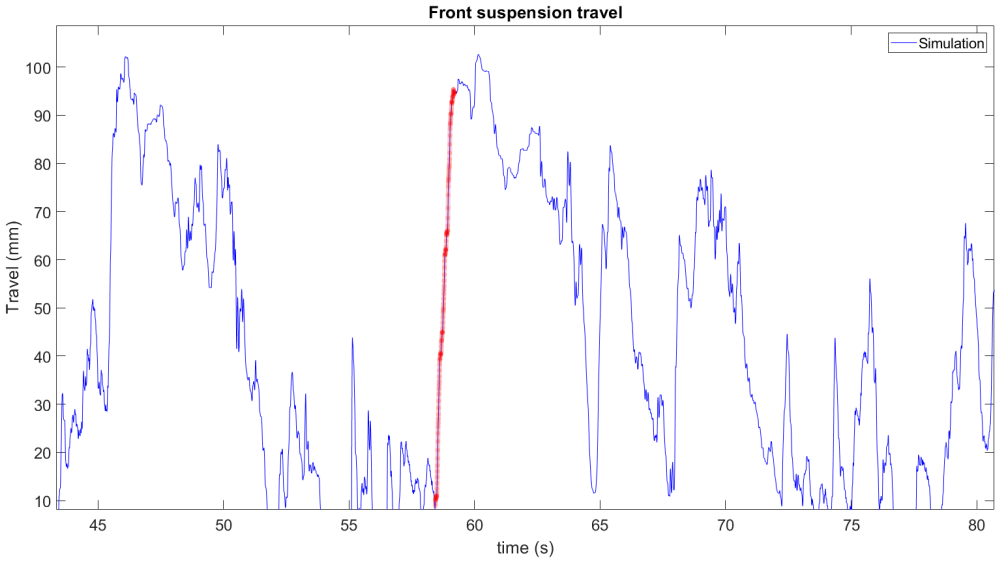

(b)

Figure D.1: Real data of suspension work for a Yamaha R6 2009 through a lap at Oulton Park circuit